# Investigating the efficacy of inverse-charging of lead-acid battery electrodes for cycle life and specific energy improvement

Constantine Spanos

Submitted in partial fulfillment of the
Requirements for the degree of
Doctor of Philosophy
In the Graduate School of Arts and Science

COLUMBIA UNIVERSITY

2017

# ABSTRACT

## *Investigating the efficacy of inverse-charging of lead-acid battery electrodes for cycle life and specific energy improvement*

Constantine Spanos

Although competitive today, traditional PbA (<1500 cycles) and advanced lead-acid batteries (ALAB) (>4000 cycles) will not be able to compete with lithium and flow batteries by 2020. To compete with novel zinc, lithium and flow batteries, the PbA chemistry needs to achieve significant performance improvements, primarily through sustainable increases to specific energy (Wh/kg), while not negatively impacting cycle life.

Inverse charging has been examined for its potential in improving PbA cycle life as a battery maintenance procedure, and as a potential technique for improving electrode specific capacity (mAh/kg) during battery manufacturing and formation. A thorough levelized cost of energy (LCOE) shows that for traditional PbA batteries with cycle lives <2000, inverse charging as a maintenance strategy (to increase cycle life) improves battery economics. Inverse charging to increase cycle life for ALAB systems (>4000 cycle life) was proven to worsen battery economics, as additional costs of capital and maintenance fail to outweigh savings achieved through reductions in replacement cost. On the other hand, inverse charging employed as a manufacturing practice to increase specific energy dramatically reduces the cost of the PbA and ALAB systems, ensuring future cost competitiveness. Inverse charging as a maintenance strategy should be restricted to devices with <2000 cycles and to projects with long project lives (20 years) that require frequent replacement. Inverse charging as a manufacturing strategy (to increase specific energy) is highly preferable in all instances.

When successful, inverse charging increases the specific capacity and active material utilization of studied battery electrodes significantly. Successful inverse charging of battery electrodes and pure lead rods show improvements in discharge capacities over a range of discharge rates with negligible impact to coulombic and energy efficiency values. The extent of success, however, depends on several important variables. Thorough examination of inverse charging on Pb rods and porous battery electrodes illustrates the importance of the degree of prior electrode sulfation and obstruction of transport of $H_2SO_4$. Other important factors include the composition of electrode grid alloys, the peak oxidation voltage applied to the negative electrode during inverse charging, initial particle sizes, and electrolyte additives.

Significant challenges to inverse charging exist. For heavily sulfated batteries and lead metals, impeded electrolyte transport results in excessive internal pore pH increases, creating semipermeable membranes through an electrode hydration mechanism, resulting in dramatic inverse charging failure. Additionally, impedance, voltage, x-ray and BET data hint that post-inverse charging, agglomeration of finely divided Pb and $PbSO_4$ particles occurs, coupled with negative electrode conductive pathway destruction. As such, the influence of expander materials and nucleation additives should be investigated to better prevent sulfation failure, and to better control the nucleation and growth of lead and lead sulfate structures during inverse charging.

Cycle life studies on flooded lead antimony batteries subjected to periodic inverse charging illustrate that inverse charging is highly successful on all batteries independent of states-of-health. Batteries with poor states-of-health (discharge capacities <15% of initial values) experienced almost perfect discharge capacity restoration post-inverse charging. Traditional methods of extending cycle life (i.e. prolonged overcharging techniques) were demonstrated to be inadequate at appreciably regenerating battery capacities, providing only marginal increases.

The benefits of inverse charging, however, are met with significant challenges to battery redesign. Temporary antimony poisoning effects lead to declines in round-trip-efficiency for batteries with antimony-based positive plates. Tin dissolution results in diminished grid to active material conductivity and reduced capacity for batteries with tin-based positives. For the negative electrode, Brunauer–Emmett–Teller (BET) surface area and x-ray measurements indicate that although large $PbSO_4$ crystals are oxidized during inverse charging, creating extensive micropore networks during conversion from Pb to $PbO_2$, surface area and capacity gains are lost during reconversion back to sponge lead due to uncontrolled nucleation and particle fusion. Additionally, active material shedding of the positive and negative electrodes is observed to spike during and after inverse charging. Negative electrode active material suffers excessive degradation and loss of cohesion, particularly for electrodes with small initial particle feature sizes, resulting in a loss of structure upon completion of the technique. Positive electrode composition changes to weakly interconnected β-$PbO_2$, dramatically increasing electrode capacity while simultaneously accelerating electrode failure through shedding. Loss of particle cohesion in both electrodes promotes excessive shedding and sludging, creating intra-cellular short-circuits. In addition, inverse charging aggravates grid growth, promoting inter-cellular short-circuiting by creating pathways for cell-to-cell electrolyte contact upon seal destruction in current monoblock designs.

# Table of Contents

# List of Figures

# List of Tables

# Acknowledgements

I would first and foremost like to thank my Ph.D. Advisors, professor Alan C. West and professor Paul F. Duby for all their guidance, motivation, and support throughout the process.

Professor West has enabled me to pursue new research directions, and trusted me to supervise fellow researchers Sarah Berlinger for her bachelors and Aditya Jayan for his masters; individuals with whom I have created lasting friendships and whose future careers I am excited to see unfold. Alan provided me a world-class research forum through weekly meetings and regular group presentations. Alan's ability to distill challenging concepts while simultaneously expounding on the complexities of research setups – from chemical interferences to contradictory datasets – lent me tremendous insight into electrochemical fundamentals. I am also thankful for Alan's patience, as well as his ability to exercise realism on timelines for research projects when presented with someone who initially thought answering the questions surrounding this work would take only a few months, (remarking instead, "that sounds like a dissertation"). I didn't quite understand until now. Thank you for giving me the opportunity to make many mistakes, for the continued trust in my capability despite the foibles, and for only laughing when I decided it was a good idea to destroy my electrodes in 96% sulfuric acid. I would also like to thank the members of the Electrochemical Engineering Laboratory at Columbia University for their invaluable insights during the early stages of the work.

Professor Duby was truly my first entry point into laboratory research, and would spend hours after class instructing me on the fundamentals of electrochemistry and experimentation, with the ever-encouraging remark "nothing interesting is a waste of time." In between countless hours discussing the history of battery and fuel cell research, I would be surprised and overjoyed to hear Paul exclaim "we have that here somewhere," before proceeding to reveal to me vital pieces of equipment and hidden relics of the School of Engineering and Applied Science, such as the local gravitational constant immediately outside the fume hood in laboratory 945, to 5 decimals, reading

9.80245 $m/s^2$. Paul piqued my imagination by loaning me any shape and size of glassware, platinum, sensors, adhesive and other knickknacks. I am grateful to Paul for placing me in charge of laboratory and classroom instruction for the undergraduates, and for taking a sincere interest in my education.

I am also indebted to professor Patricia Culligan, director of the Integrative Graduate Education and Research Traineeship fellowship, for supporting my research through the M.S. degree, and for always being available and able to find a simple solution to seemingly insurmountable challenges. Likewise, to my M.S. advisor professor Vasilis M. Fthenakis for providing a welcoming environment at Columbia and for continued support throughout the Ph.D. In addition, thanks are due to my dissertation committee members, Drs. Daniel Esposito, Daniel Steingart, Alyssa Park, and Ngai Yin Yip for taking the time and energy to lend further insight on the work.

I owe a great portion of my enthusiasm for research to friends and fellow researchers, specifically to my good friend Dr. Timothy Sharobem, who was always available for laboratory help and discussion despite his own engagements. In addition, I would like to thank former friends and research collaborators Drs. Melis Duyar, Angela Zheng, Emi Leung, Kevin Knehr, Lev Sviridov, Joshua Gallaway, and Damon Turney.

To my brother John, sister Zoe, parents Konstantinos and Carmen, and girlfriend Caroline, thank you for the love, encouragement and healthy mockery, and for supporting me without ever fully understanding what I was researching.

In addition, much of this research was conducted with government support under and awarded by the Department of Defense, Air Force Office of Scientific Research, National Defense Science and Engineering Graduate (NDSEG) Fellowship, 32 CFR 168a.

# 1. Introduction

Lead-acid (PbA) batteries are the most mature secondary battery technology, and the most commonplace for over 150 years. Of the 54B battery market in 2013, PbA batteries accounted for 60%, with the automotive sector growing fastest [1]. Increasing deployments of inherently variable wind and solar energy exceeding 10%-15% of grid supply is impractical without large quantities of energy storage [2]. In parallel, government mandates are stimulating growth in electric vehicle (EV) markets. PbA, although used in both grid and automotive applications, faces stiff competition from other chemistries, particularly lithium-ion (Li-ion).

In Europe and America, 99% of PbA batteries are collected and recycled, the highest rate of recycling for a consumer product [3]. Primary lead (Pb) is among the easiest metals to extract due to low melting points, and approximately 60-80% of battery Pb comes from older batteries, giving PbA one of the lowest environmental footprints [3,4]. PbA batteries have a track record of safety, low capital cost, and are used in applications that range from starting-lighting-ignition (SLI) in vehicles, traction, backup batteries for uninterrupted power supply, renewables integration, and bulk power storage in combination with solar-home systems [1].

Although cheap to produce, PbA batteries have lower active material utilization than most battery chemistries (*Section 1.3*), relying on bulky Pb current collector designs and thicker electrodes that impede electrolyte transport and form undesirable concentration gradients [3]. Low cycle life, and energy densities ≤ 40 Wh/kg (Table 1-1) prevent PbA demand from growing at the rates of chemistries offering portability advantages and flexibility of use in both automotive and grid applications. Policymakers and venture capitalists largely ignore PbA chemistries, placing an emphasis on Li-ion technologies. As such, the market share for alternative battery technologies has been growing rapidly, from 5% in the 1990s, to an expected

level of 40% in 2020. By 2020, PbA batteries have a forecasted market of $47B, closely followed by Li-ion with $32.5B [3]. Due to the increasing prevalence of Li-ion batteries in consumer products, and more recently grid-level storage installations, there are mounting pressures for PbA research to improve cycle life, as well as renewed interest in anode charging as a means of mitigating sulfation (irreversible sulfate crystal accumulation, *Section 1.4.6*) [5,6].

The European mandate for a 35% $CO_2$ reduction in new car emissions by 2021 (2015 base levels) expanded the market for micro-hybrids and has driven recent innovations in advanced PbA batteries [7,8]. In 1992, the Advanced Lead-Acid Battery Consortium (ALABC) was created to support pre-commercial development of PbA technology. This international consortium of 80 companies and organizations continues to make significant progress through fundamentals research in key challenge areas to ensure strong PbA market growth [3,9]. ALABC investments in next-generation PbA proceeded from examining positive plate deficiencies during deep discharge to addressing premature degradation of the negative for hybrid electric vehicle (HEV) and photovoltaic (PV) system applications. Negative electrodes in valve-regulated lead-acid (VRLA) batteries suffer rapid capacity declines due to progressive sulfation when cycled at partial states-of-charge (PSoC) common to HEV and PV applications. Partnerships screened through 14 formulations of carbon additives (graphite, activated carbon, carbon black, carbon fibers and graphene), and found activated carbons to yield the greatest benefit in small percentages (~0.2%) of negative electrode paste [1,3,9].

New lead-carbon (PbC) batteries now come in the form of enhanced flooded batteries (EFB) [10,11], and VRLA absorptive glass mat designs (e.g. UltraBattery®) [6,12,13]. Retrofitted HEVs with PbC batteries demonstrated improved dynamic charge acceptance (DCA) for better regenerative breaking capability, and showed continuous operation for >150,000 miles

with only 12% reduction of initial capacity [3]. Similarly, independent testing of PbC batteries in photovoltaic (PV) systems by Sandia National Laboratories showed eight times the cycle life of standard AGM batteries currently used in the same application [14]. Other testing on new separators, tubular positive plate gauntlets, negative plate additives (silica, carbon), electrolyte improvements with phosphoric acid, and optimized pulse charging showed lead cells capable of completing >3150 cycles at 50 °C, or 6300 cycles (17.5 years of operation) for PV systems at 20°C [3].

ALABC research has shown that significant improvements are realized through lower electrolyte concentrations (1.25 g/cm$^3$), an elimination of overcharging, tubular positive plate gauntlets, improved separator design, and activated carbon additions to negative electrode paste. Future PbA development will be based on basic research & development (R&D) into the materials science of the capacity-bearing and current-collecting materials through optimized cell design, judicious use of carbon, and alloys that prevent gassing and water loss and minimizing grid corrosion [3].

Pb, due to its toxicity is the subject of evaluation for several recent policies that seek to ban hazardous materials. In 2015, the European Union's Registration, Evaluation, Restriction and Authorization of Chemicals (REACH) regulation added Pb compounds to the list of substances requiring authorization for future use. As such, the future of PbA batteries is uncertain unless superiority of the chemistry can be demonstrated [3].

## 1.1. Electrochemical principles

The electrochemical reactions taking place at the positive and negative electrodes of a PbA battery are outlined in Eqns. 1-1 and 1-2, respectively. During discharge, the positive electrodes

accept electrons from the negative, each forming $PbSO_4$ through a dissolution precipitation reaction mechanism in a sulfuric acid ($H_2SO_4$) electrolyte, Eqn. 1-3. On recharge, fine particles of $PbSO_4$ are electrochemically converted back to Pb at the negative electrode and $PbO_2$ at the positive, as $SO_4^{2-}$ ions are driven back into the electrolyte [1].

- Negative electrode (anode) reaction, discharge (→), recharge (←):

$$Pb + SO_4^{2-} \leftrightarrows PbSO_4 + 2e^- \qquad (1\text{-}1)$$

- Positive electrode (cathode), discharge (→), recharge (←):

$$PbO_2 + SO_4^{2-} + 4H^+ + 2e^- \leftrightarrows PbSO_4 + 2H_2O \qquad (1\text{-}2)$$

Dissolution precipitation intermediate (similar on both negative and positive plates)

$$Pb^{2+}_{(aq)} + {SO_4}^{2-}_{(aq)} \leftrightarrows {PbSO_4}_{(aq)} \qquad (1\text{-}3)$$

The overall reaction is the sum of Eqns. (1-1) and (1-2), discharge (→), recharge (←):

$$Pb + PbO_2 + 2H_2SO_4 \leftrightarrows 2PbSO_4 + 2H_2O \qquad (1\text{-}4)$$

The equilibrium potential of both electrodes can be calculated using the Nernst Eqn. 1-5, 1-6:

$$\mathrm{E_{PbO_2/PbSO_4}} = \mathrm{E^0_{PbO_2/PbSO_4}} + \frac{RT}{nF}\ln\left(\frac{a_{PbO_2} \bullet a_{SO_4^{2-}} \bullet a_{H^+}^4}{a_{PbSO_4} \bullet a_{H_2O}^2}\right) \qquad (1\text{-}5)$$

$$\mathrm{E_{Pb/PbSO_4}} = \mathrm{E^0_{Pb/PbSO_4}} + \frac{RT}{nF}\ln\left(\frac{a_{PbSO_4}}{a_{Pb} \bullet a_{SO_4^{2-}}}\right) \qquad (1\text{-}6)$$

Where, $E^0 = \frac{-\Delta G^0}{nF}$, $F$= 96,485 coulombs per mole electrons (C/mol $e^-$). At 25 °C, $T$ = 298 °K; gas constant $R$ = 8.314 J/mol•°K, activity of the solid phases $a_{PbO_2}$, $a_{PbSO_4}$, $a_{Pb}$= 1, and two electrons participate in the reactions at each of the electrodes, i.e., $n$ = 2. Substituting into the equations for the $Pb/PbSO_4$ (Eqn. 1-7) and $PbO_2/PbSO_4$ (Eqn. 1-8) electrodes yields:

$$E_{Pb/PbSO_4} = -0.358 - 0.029 \log a_{SO_4^{2-}} \qquad (1\text{-}7)$$

$$E_{PbO_2/PbSO_4} = 1.683 - 0.118pH - 0.059 \log a_{H_2O} - 0.029 \log a_{SO_4^{2-}} \qquad (1\text{-}8)$$

$$\Delta E = E_{PbO_2/PbSO_4} - E_{Pb/PbSO_4} \quad (1\text{-}9)$$

$$\Delta E = 2.041 - 0.118pH - 0.059 \log a_{SO_4^{2-}} - 0.059 \log a_{H_2O} \quad (1\text{-}10)$$

$$\Delta E = 2.041 + 0059 \log \left(\frac{a_{H_2SO_4}}{a_{H_2O}}\right) \ [V] \quad (1\text{-}11)$$

$E^0_{PbO_2/PbSO_4}$ depends on the crystal configuration of $PbO_2$ (tetragonal $\beta$ $-PbO_2$ < orthogonal $\alpha$ $-PbO_2$) [3]. From Eqns. 1-9 to 1-11 we can calculate the electromotive force (EMF), $\Delta E$, as a function of $H_2SO_4$ concentration, and the activities of $H_2O$ and $H_2SO_4$ for different concentrations are tabulated and readily available [15]. The EMF, or cell potential of the battery is measurable at open circuit, giving an open circuit voltage (OCV). The OCV will vary as a function of acid concentration, battery depth-of-discharge (DOD), and temperature, with $\partial \Delta E / \partial T$ = 1.31 mV/°K [15]. A certain period is needed to equalize the $H_2SO_4$ concentration between the two plates before measuring the EMF of the cell. True steady state values are often reached after 8 hours or even longer [16]. During normal battery discharge, insulating $PbSO_4$ crystals progressively nucleate and coalesce on the anode, obstructing transport of sulfate ions into the interior of the electrode, coinciding with a decline in cell voltage [17,18].

Each electrode potential is measured with respect to a reference electrode. The $Hg/Hg_2SO_4$ reference electrode is the predominant electrode used in PbA research, due to its stability and precision in this system. Calculated potentials for fully charged negative and positive electrodes with respect to various reference electrodes are presented in Figure 1-1, whereby the concentration of sulfuric acid in the reference electrode and battery cell electrolyte are the same. When concentration gradients manifest, additional non-equilibrium junction potentials are added. Diffusion potentials also develop between upper and lower parts of the battery cell due to electrolyte stratification, and because of concentration gradients between current collector and the electrolyte surface during charge and discharge.

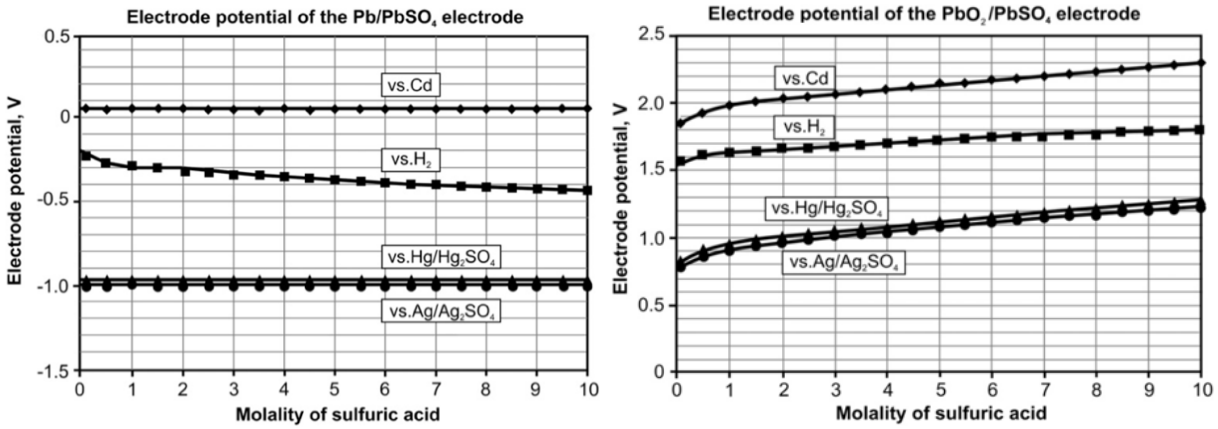


**Figure 1-1:** Calculated electrode potentials of the a) Pb|$PbSO_4$ electrode as a function of concentration with respect to different reference electrodes, b) $PbO_2$|$PbSO_4$ electrode. Source: Ref. [16].

## 1.2. Lead-acid battery formats

PbA batteries are classifiable into two types, depending on the state of the electrolyte. Both can be constructed with electrodes in prismatic format, and with tubular positive electrodes in compression gauntlets. Only VRLA cells are available in spirally wound configurations. Both are constructed with calcium alloyed negative grids (Pb-Ca) [15]:

- Flooded, vented lead-acid (VLA): batteries with an excess flooded electrolyte, such as starting-lighting-ignition (SLI) batteries. During charging, hydrogen gas evolved on the negative electrode and oxygen evolved on the positive are vented through a one-way valve, resulting in gradual decline of water in the electrolyte. Water is easily replaced periodically. Positive grids are commonly alloyed with antimony (Pb-Sb) [19].

- Gas recombinant, valve-regulated lead-acid (VRLA): "acid starved" or "maintenance free", VRLA batteries immobilize the electrolyte as a gel, or in an absorptive glass mat (AGM) separator with a small quantity of highly concentrated sulfuric acid. Oxygen evolved from the positive migrates through air channels in the mat separator or

microfissures in the silica gel, and recombine to $PbSO_4$, creating the internal oxygen cycle of Eqn. 1-12:

$$Pb + \frac{1}{2}O_2 + H_2SO_4 \leftrightarrows PbSO_4 + H_2O + Heat \qquad (1\text{-}12)$$

Evolved hydrogen on the negative electrode in recombinant cells is not recoverable, and is instead released through a pressure valve, resulting in water loss [20]. Positive grid alloys are of calcium and tin (Pb-Ca-Sn) [19].

## 1.3. Electrode formation and active material utilization

Both the active material of the positive electrode (PAM), and of the negative (NAM) are formed from leady oxide (LO), a powder made of thermally oxidized lead particles to 70-80 wt. % $\alpha$ or $\beta$ −PbO content, prepared in a Barton pot or ball mill [21]. ). Active material paste is prepared via introduction of diluted $H_2SO_4$, which initiates the heterogeneous reactions of Eqns. 1-13 – 1-15, transforming $\alpha$ −PbO to $\beta$ −PbO, forming monobasic sulfate, $PbO{\cdot}PbSO_4$ (1BS), and tribasic sulfates, $3PbO{\cdot}PbSO_4{\cdot}H_2O$ (3BS). Basic sulfate reactions proceed through a lead hydroxide intermediate, $Pb(OH)_2$ [22].

$$\alpha - PbO \rightarrow \beta - PbO \qquad (1\text{-}13)$$

$$2PbO + H_2SO_4 \rightarrow PbO{\cdot}PbSO_4 + H_2O \qquad (1\text{-}14)$$

$$4PbO + H_2SO_4 \rightarrow 3PbO{\cdot}PbSO_4{\cdot}H_2O \qquad (1\text{-}15)$$

After lead electrode grids (current collectors and tabs) are cast, the slurry is pasted on the grids and left to cure and recrystallize while controlling relative humidity, reaction time, temperature, and particle size. Curing above 80 °C and steam treating transforms 3BS to tetrabasic sulfates, $4PbO{\cdot}PbSO_4$ (4BS), Eqn. (1-16), yielding large crystals better suited for deep-cycling stationary batteries and traction batteries [23].

$$2(3PbO{\cdot}PbSO_4{\cdot}H_2O) + \alpha - PbO + \beta - PbO \rightarrow 2(4PbO{\cdot}PbSO_4) + 2H_2O \qquad (1\text{-}16)$$

The size of 4BS crystals range from 30-40 μm. Pastes containing mostly 3BS crystals have higher initial capacity. Their life, however, is shorter than that of plates prepared with 4BS pastes [24,25].

Cured pastes comprise a mixture of $PbSO_4$, 1BS, 3BS, 4BS, PbO and Pb. The formation of positive and negative electrodes involves electrochemically converting cured pastes into electrochemically active porous materials: $PbO_2$ in the positive electrodes and Pb in the negative electrodes [1]. This is accomplished through charging within the assembled battery (jar formation), or charging electrodes in tanks of sulfuric acid (tank formation) [26].

PbA batteries only utilize a small fraction of the active material. The active material of the electrode is comprised of two parts 1) the energetic mass, $G_e$, the active material portion electrochemically responsible for storing and discharging energy, 2) the skeletal mass, $G_s$, the mass of the active material providing mechanical support and electron conductivity, transmitting current throughout the plate. The total weight of the negative or positive active material (NAM or PAM, respectively), $G$, is the contribution of the both portions (Eqn. 1-17).

$$G = G_e + G_s \qquad (1\text{-}17)$$

The active mass utilization coefficient ($\eta_{util}$) is the share of weight for the energetic structure of the active mass, Eqn. 1-18. PAM and NAM utilization ranges from 35% to 55%, depending on the design features of the battery and the design discharge current. PAM utilization is typically greater than for NAM due to smaller active material crystallites.

$$\eta_{util} = \frac{G_e}{G} < 1 \qquad (1\text{-}18)$$

For a specific battery capacity, *C,* in Amp-hours, the weight of active mass per Ah of charge, ($\beta$) and the specific capacity per kg of active mass, ($\sigma$) are equal to:

$$\beta = \frac{G}{C} \quad [g{\cdot}Ah^{-1}] \qquad (1\text{-}19)$$

$$\sigma = \frac{C}{G} \quad [Ah{\cdot}g^{-1}] \qquad (1\text{-}20)$$

The coefficients describe the relationship of PAM or NAM weight to electrode capacity on discharge. The correlation between $\eta_{util}$, $\beta$ and $\sigma$ for a standard PbA battery is presented in Figure 1-2. All values are determined experimentally for each technology of PAM or NAM active mass produced, and depend on the battery type and application as illustrated in Table 1-1 [16].

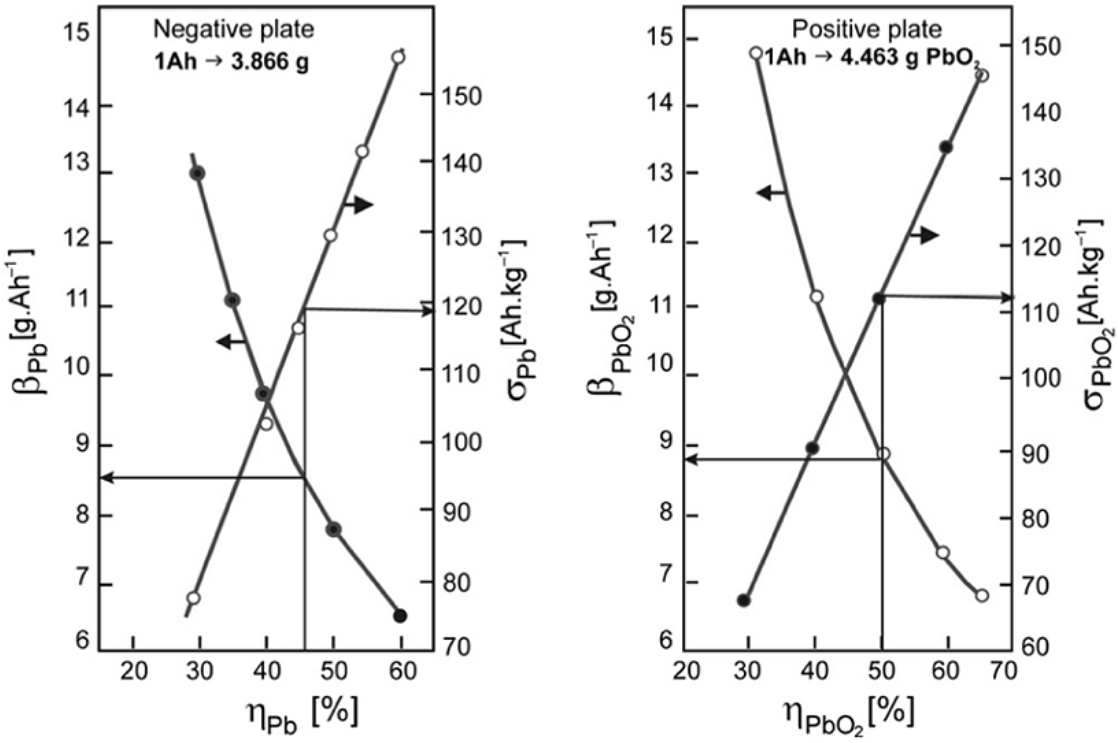


**Figure 1-2:** Correlation between active material utilization and specific capacity using established manufacturing techniques. Source: Ref. [16].

**Table 1-1:** Range of specific energy and active material capacity for PbA battery formats. Source: Ref. [16].

| | Specific Energy | | $\beta$ and $\sigma$ Coefficients | | | |
|---|---|---|---|---|---|---|
| | | | $PbO_2$ | | Pb | |
| Battery Type | Wh $kg^{-1}$ | Wh $L^{-1}$ | $\beta_{PbO_2}$ g $Ah^{-1}$ | $\sigma_{PbO_2}$ Ah $kg^{-1}$ | $\beta_{Pb}$ g $Ah^{-1}$ | $\sigma_{Pb}$ Ah $kg^{-1}$ |
| SLI (20h rate) | 30–40 | 75–100 | 10–7.7 | 100–130 | 8.7–6.5 | 115–154 |
| Traction cell (5h rate) | 25–32 | 60–100 | 16.7–11.1 | 60–90 | 12.5–10.0 | 80–100 |
| Stationary battery: Flooded | 20–28 | 35–60 | 16.7–10.0 | 60–100 | 12.5–10.0 | 80–100 |
| VRLAB (60Ah) | 21–31 | 45–85 | 15.2–11.4 | 66–90 | 12.5–7.2 | 80–140 |

## 1.4. Failure modes of the PbA battery

The quick failure of PbA batteries is the key barrier to its future deployment. PbA failure modes are interdependent with several mechanisms contributing simultaneously to performance declines, necessitating a general overview [27].

### 1.4.1. Anodic corrosion of grids, plate-lugs and posts

Anodic grid corrosion is a predominant failure mechanism; positive electrode grids are gradually consumed during float and overcharging, and during standby operation. During charging, Eqns. 1-21 – 1-22, Pb grid bars anodically react with surface adsorbed water, precipitating new $PbO_2$ at the Pb/$PbO_2$ interface, which in the absence of sulfuric acid takes the $\alpha$-modification [27–29].

$$Pb + 2H_2O \rightarrow \alpha - PbO_2 + 4H^+ + 4e^- \qquad (1\text{-}21)$$

$$2H_2O \rightarrow O_2 + 4H^+ + 4e^- \qquad (1\text{-}22)$$

During standby, the Pb grid forms an unstable thermodynamic couple with PAM, Eqn. 1-23. Oxidation of the lead grid at the Pb/$PbO_2$ interface occurs simultaneously with cathodic reduction of $PbO_2$ at the $PbO_2$/electrolyte interface [30]. Formed $PbO_2$ corrosion layers are impervious to $SO_4^{2-}$ and $HSO_4^-$ ions, and corrosion during standby is slow.

$$2\beta - PbO_2 + Pb + 2H_2SO_4 \rightarrow \alpha - PbO_2 + 2PbSO_4 + 2H_2O \qquad (1\text{-}23)$$

Figure 1-3 illustrates the steady-state corrosion currents observed on pure Pb metal as a function of electrode potential. Three important regions are observed [27]:

1. Zero corrosion is experienced at potentials < -0.971 V vs. $Hg/Hg_2SO_4$, potentials on the negative electrode during charging, because of cathodic protection.
2. Corrosion rates increase in regions where $PbSO_4$ is formed (-0.971 to +1.12 V), volumetrically large sulfates are less protective than $PbO_2$, accelerating corrosion due to crack and crevice formation.
3. >1.12V, anodic corrosion currents are seen to decrease to a minimum at +1.18 V vs. $Hg/Hg_2SO_4$ (5 molal $H_2SO_4$), representing the ideal float charging potential of the positive electrode at this acid concentration.

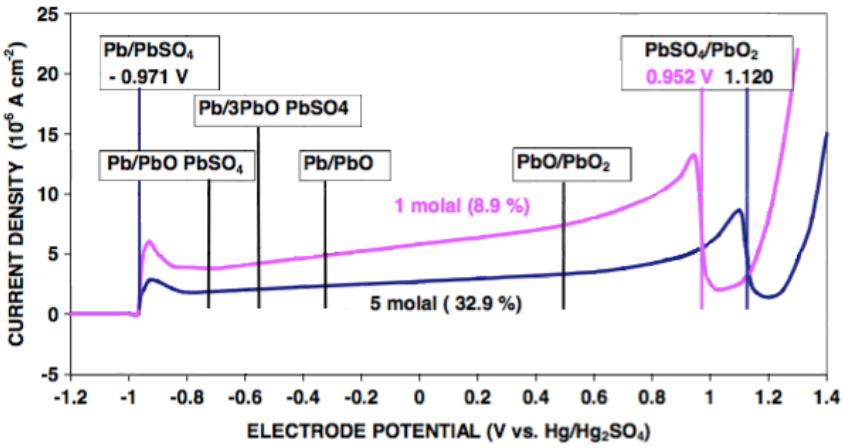


**Figure 1-3:** Schematic representation of long-term, steady-state anodic corrosion currents held at constant potential, T = 25°C. Source: Ref. [27].

Minimum corrosion currents at +1.18 V corresponds to 2 $\mu A/cm^2$ or a transformation of metallic Pb to $\alpha$-$PbO_2$ at 0.03 mm/yr, implying a 20 yr life for a PbA battery with 3 mm thick grids [27]. Corrosion rates increase during overcharging, and are higher for grids with antimony in the positive grid alloys (>1.18% Sb). Corrosion is inhibited through finer grain structures, achievable

through additions of selenium or arsenic (0.15%) to Pb-Sb grids, and aluminum to Pb-Ca-Sn grids. At lower acid concentrations, Pb and $PbSO_4$ solubility increases, implying corrosion increases in discharged batteries. Additionally, at higher temperatures, corrosion currents are exacerbated.

Positive electrodes in VRLA batteries experience higher overpotentials than in flooded batteries (>50 mV), and corrosion rates are as much as two times higher. Plate lugs and posts in VRLA systems on the negative electrode also experience corrosion due to dilute electrolyte films and insufficient cathodic protection throwing power [27].

### 1.4.2. Loss of water, electrolyte contamination

Flooded cells held at constant float voltages of +2.45 volts per cell (vpc) exhibit differing proportions of side reactions compared to VRLA cells. Oxygen cycle depolarization, Eqn. 1-12, in VRLA cells shifts each electrode's voltage in the positive direction by ΔV, Figure 1-4. This results in higher currents for grid corrosion ($I_C$) and oxygen evolution ($I_{O_2}$) at the positive, while increased oxygen reduction currents ($I_{O_2\text{-}red}$) suppresses the rate of hydrogen evolution ($I_{H_2}$) on the negative. Suppressing hydrogen evolution in VRLA cells is desirable to prevent electrolyte dryout, but poses a challenge to fully recharging the negative electrode. Current may be continually consumed by the internal oxygen cycle such that the negative plate never reaches a full state-of-charge, and may lead to thermal runaway, a prevalent failure mode in recombinant batteries [31].

During charging of the positive electrode, oxygen evolution is accompanied by corrosion reactions. At high anodic potentials, the oxygen evolution current is typically about 100 times larger than the corrosion current [27].

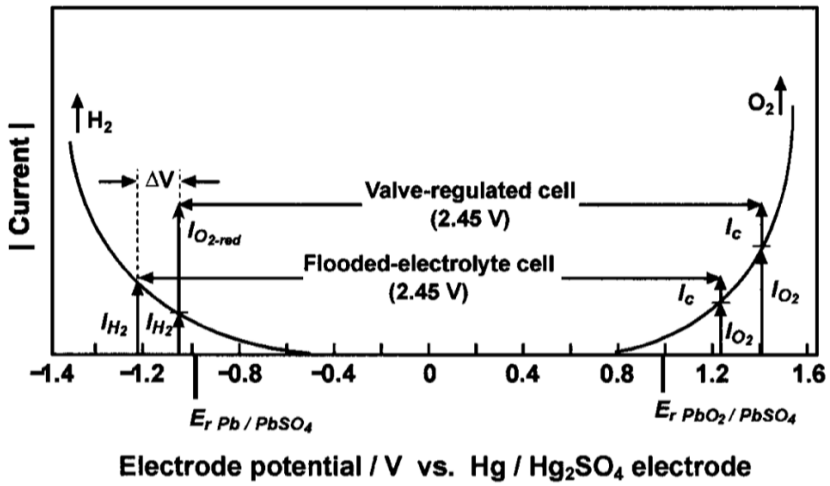


**Figure 1-4**: Side reaction currents in flooded and VRLA cells during CV charging at +2.45V. Currents presented in absolute value for convenience. Source: Ref. [31].

For flooded cells, water loss is easily replaced, while for VRLA cells it is irreversible [20]. As positive grids undergo corrosion in flooded PbA cells of Pb-Sb grid alloy, leached antimony deposits on the negative plates. Hydrogen evolution on antimony proceeds at low charging overpotentials, accelerating the decomposition of water. Transition to VRLA designs required the removal of antimony to prevent water loss, replacing it with tin, a metal with poor hydrogen evolution kinetics [19]. In flooded batteries, the hydrogen evolution rate can be strongly influenced by impurities in refilled water that may deposit on the negative electrode [27].

### 1.4.3. Positive active mass degradation and sludging

Batteries subjected to regular cycling fail largely through the disintegration of the positive active mass (PAM) energetic structure ($G_e$). Conversion of $PbO_2$ to $PbSO_4$ during discharge at the positive plate results in significant volumetric change and stress. The molar volume of $PbSO_4$, $V_{m,PbSO_4}$ is 92% greater than $V_{m,PbO_2}$, figure 1-5 [15]. Recharging does not fully restore $PbO_2$ to the original volume, and with increasing depth-of-discharge per cycle, PAM degradation is accelerated. During cycling service, an increasing fraction of the active material becomes

electrically disconnected from the current-collector [31,32]. PAM has been modeled as an interconnection of spheres. During cycling, interconnections slowly thin and shedding occurs during a loss of coherence [33].

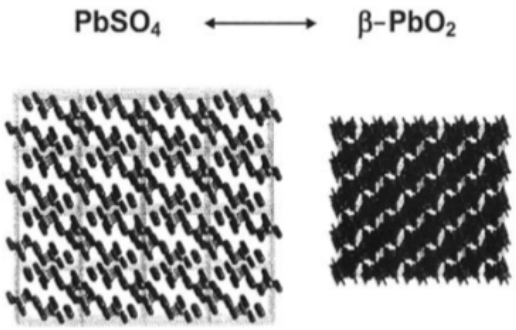


**Figure 1-5:** Volumetric differences between PAM phases for same number of lead atoms. Source: Ref. [31].

At the negative, $V_{m,PbSO_4}$ is 164% greater than $V_{m,Pb}$. Shedding is not observed due to lead's malleability (compared to the brittleness of $PbO_2$) incorporating more voluminous $PbSO_4$ [15].

Differing discharge and charge rate significantly affect PAM shedding. High current discharge utilizes active material adjacent to the grid, while slow recharges redeposits $PbO_2$ throughout the entire plate, causing a gradual displacement of active mass toward the plate surface [27]. With continued cycling, PAM shedding will result in sludging, or the accumulation of material at the base of the battery. Sludging results in internal short circuiting of the battery. PAM shedding can be mitigated through appropriate electrode compression, (i.e. through the use of tubular-plate positive electrodes), while sludging can be reduced through the use of pocket-type separators [34–36].

### 1.4.4. Premature capacity loss

The removal of antimony from the positive electrode for VRLA batteries results in premature capacity loss (PCL), where positive electrodes suffer accelerated disintegration of the mechanical and electronic contact between grid and PAM. Passivating lead oxide inhibits conductivity at the

current collector, resulting in difficulties recharging and recovering from deep discharge [1]. Anodic dissolution of alloyed antimony in Pb-Sb electrodes prevented PCL by incorporating into the PAM in the form of hydrated antimony oxides, cementing $PbO_2$ particles and ensuring conductivity at the grid/PAM interface. The addition of tin in Pb-Ca-Sn electrodes in quantities >0.7% was found to aid in formation of mixed lead-tin oxides and restored conductivity in VRLA batteries [37–39].

### 1.4.5. Short circuits due to hydration

In dilute electrolytes, $PbSO_4$ precipitates in a dendritic, voluminous form that can result in short circuits. This is attributable to a tenfold increase in solubility of $1.6x10^{-5}$ in 0.1 M $H_2SO_4$ to $1.5x10^{-4}$ mol/L in water (25 °C). High solubility of $PbSO_4$ at low acid concentrations can be reduced by addition of 0.1M $Na_2SO_4$ to the electrolyte [20,27].

### 1.4.6. Sulfation

Sulfation is one of three predominant failure modes in PbA batteries, the others being positive electrode grid corrosion and active material shedding [20,40]. Sulfation is the recrystallization of $PbSO_4$ into a form that is no longer electroactive. A certain portion of irreversible $PbSO_4$ is accumulated on every discharge as a result of recrystallization of finely divided particles according to the Ostwald-Fruendlich equation, Eqn. 1-24 [6,20,41].

$$\ln\left(\frac{C_{Pb^{2+}}}{C^{\infty}_{Pb^{2+}}}\right) = \frac{K}{T \cdot r} \qquad (1\text{-}24)$$

Where $C_{Pb^{2+}}$ is the $Pb^{2+}$ ion concentration over the small crystals, $C^{\infty}_{Pb^{2+}}$ is the ion concentration over big $PbSO_4$ crystals, $K$ is an empirical constant, $T$ is temperature. and $r$ is the radius of the crystals. Big $PbSO_4$ crystals grow at the expense of dissolution of the small ones (figure 1-6).

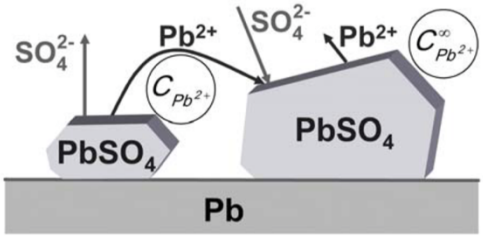


**Figure 1-6:** Illustration of recrystallization phenomena in PbA batteries. Source: Ref. [6].

In VRLA batteries, sulfation is aggravated in the negative electrode as a result of inadequate charging, due to internal oxygen cycle anode depolarization, requiring higher float voltages than flooded batteries [5,27,31]. In conventional flooded battery formats, sulfation is observed during regular deep discharges and battery idling during prolonged storage. Flooded batteries with lead-antimony grids suffer higher self-discharge rates than their VRLA counterparts, and spend a larger fraction of storage time in a discharged state, conditions favorable for $PbSO_4$ crystal growth [40]. If PbA anodes spend a significant time in storage (over 6 months) at partial states-of-charge (PSoC), sulfate crystals on the anode coarsen and recrystallize, becoming increasingly difficult to reduce, leading to a loss of discharge capacity, declines in OCV, decreasing acid concentration, and increases in internal resistance [6,42]. Accumulation of large fractions of 1BS and 3BS has been observed in stored flooded batteries, indicating that electrolyte alkalization in interior pores results from poor permeability through enlarged exterior surface crystals [42,43].

Sulfation has not been described as a failure mode for the positive electrode, due to the relative ease of $PbO_2$ growth on $PbSO_4$ via endotaxial metasomatic substitution upon battery charging [44]. Smaller active material crystallites in positive active masses allow for higher utilization and reaction reversibility [41]. Sulfation of the positive plates is reversible as long as conductive pathways in the electrode remain intact [45,46].

In tall flooded cells with a height >25 cm, sulfation results from acid stratification, (figure

1-7). This is a conditions of high acid concentration at the bottom of the cell, and low concentration at the top, which results in accelerated self-discharge of the bottom of the plate due to created diffusion potentials [27]. An effective means to avoid stratification is the installation of an electrolyte circulation pump.

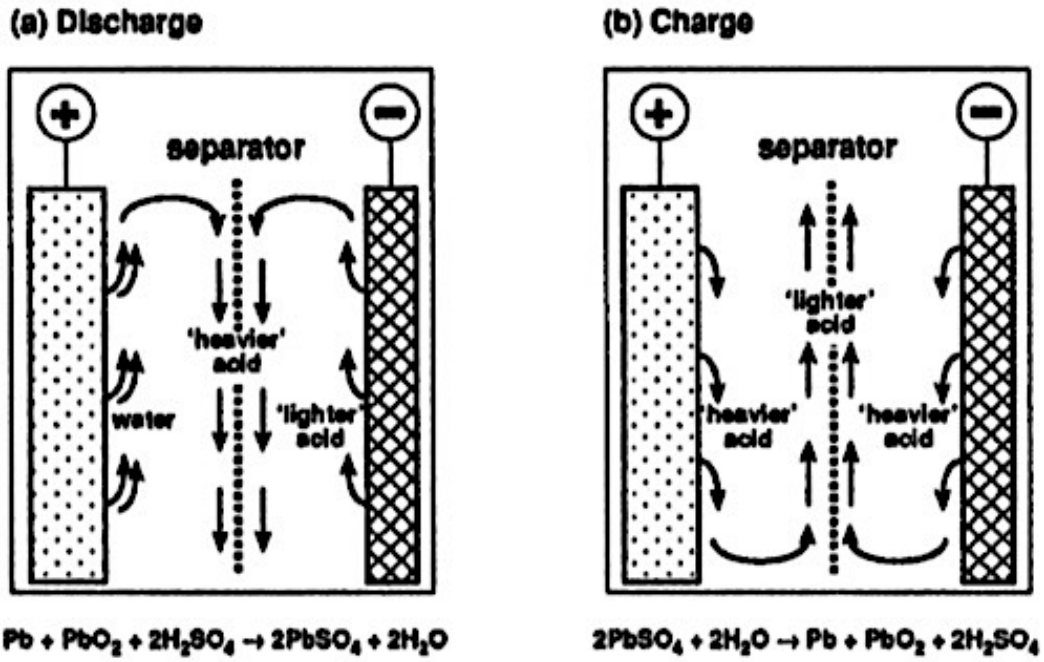


**Figure 1-7:** Sulfuric acid stratification in flooded batteries during charging and discharging. Source: Ref. [31].

## 1.5. Motivation for this thesis

Despite significant progress in understanding the mechanisms of failure for the PbA battery and improving battery design, critical improvements to specific energy and cycle life are necessary to compete with alternative chemistries such as Li-ion. A specific energy ≤ 40 Wh/kg is ≤ 23% of the theoretical value of 172.32 Wh/kg (Assuming $\Delta E$=2.04 V, 100% sulfuric acid) [15]. The specific energy actually achieved decreases further with increase in the discharge rate to ~16% of theoretical at the 2 h rate [4]. ALABC improvements to the chemistry and desired targets are

illustrated in Figure 1-8. A doubling of specific energy is heavily desirable for the industry, and has significant implications for the environment.

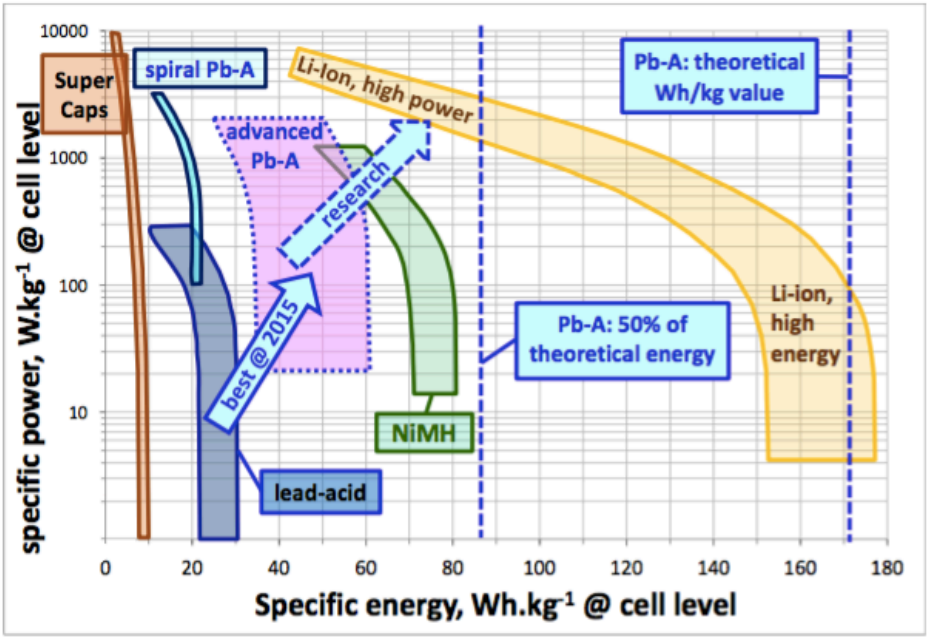


**Figure 1-8:** Ragone plot illustrating recent advances in PbA development as compared to other chemistries. Source: Ref. [3]

PAM degradation during cycling and grid corrosion are the two major failure modes for positive electrode, while irreversible sulfation is the most common failure mode for the negative electrode. Introduction of carbon materials to the negative electrodes of PbA batteries could suppress the sulfation problem and increase the reversibility of charge-discharge when added to NAM pastes, and restraining the growth of $PbSO_4$. However, additions of carbon result in lower capacities and greater hydrogen evolution, due to a reduction in overpotential, as illustrated in Figure 1-9.

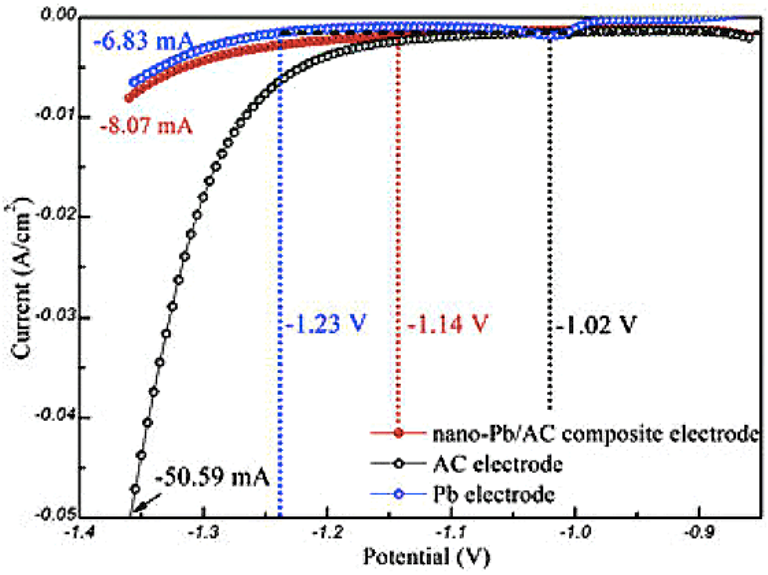


**Figure 1-9:** Overpotential changes with carbon additions to NAM. Source: Ref. [1].

Doubling specific energy implies significantly increasing active material utilization ($\eta_{util}$) and the specific capacity per kg of active mass ($\sigma$).

On the other hand, cycle life remains predominantly limited by PAM shedding and negative plate sulfation. PAM shedding is best mitigated using antimony alloy, compression gauntlets in tubular electrodes, and managing charge and discharge rates. Recrystallization of $PbSO_4$ always exists, and is exacerbated in applications where full charging is infrequent (PV systems, HEVs) [3]. Sulfation of the anode structures of PbA batteries has traditionally been mitigated through the use of additives and expander materials in negative electrode active mass formulations (~0.3% $BaSO_4$, ~0.2% lignosulfonates, ~0.1% of carbon black), and more recently through the introduction of electroactive carbons [5,12,13,27,47]. While this has increased cycle life substantially, non-reacting additives in the active material provide structure and conductivity to the plates, but do not significantly increase utilization, creating roadblocks to specific energy doubling. Pulse chargers have also been investigated for sulfation treatment of VRLA batteries

operating under high-rate partial state-of-charge (HRPSoC) duty, with relative success [48,49]. Chemical techniques for PbA battery rejuvenation have been investigated with limited applicability, using sulfate salts to improve electrolyte conductivity or persulfate oxidizers to forcibly oxidize unreactive sulfates. Karami [46] makes use of a combination of 40% ammonium persulfate oxidant in a 50 °C sulfuric acid electrolyte, with necessary controls on temperature and reaction time.

### 1.5.1. Inverse charging to reverse sulfation and increase specific energy

Due to differences in $PbSO_4$ crystallite size and activity between the positive and negative electrodes, inverse charging has been proposed as an electrochemical technique to eliminate accumulated sulfate fractions on the negative electrode [48]. Electrochemical inverse charging techniques run along a similar vein to chemical oxidizers, but have the added benefit of avoiding electrolyte replacements, electrode washing, and the possibility of introducing metallic contaminants or other impurities into the battery electrolyte. We utilize the same notation as Zhang [48], where $PbSO_4$(O) refers to lead sulfate formed from oxidation of Pb on the anode, and $PbSO_4$(R) refers to that formed from reduction of $PbO_2$ on the cathode. The inverse charging sequence involves conversion of anodic $PbSO_4$(O) into $PbO_2$, prior to recharging the anode back to lead metal, thereby consuming and reactivating $PbSO_4$(O) as $PbSO_4$(R). If the reactions are coupled with the positive electrode as a two-electrode battery arrangement, this involves temporarily switching both electrode's polarities as described in Eqns. 1-25–1-26.

- Inverse charging of the negative electrode (anode):

$$Pb \rightarrow PbSO_4(O) \rightarrow PbO_2 \rightarrow PbSO_4(R) \rightarrow Pb \qquad (1\text{-}25)$$

- Inverse charging of the positive electrode (cathode):

$$PbO_2 \rightarrow PbSO_4(R) \rightarrow Pb \rightarrow PbSO_4(O) \rightarrow PbO_2 \qquad (1\text{-}26)$$

Inverse charging has only been described in three distinct peer reviewed studies [45,46,48,50]. Zhang [48] and Yamamoto [50] conducted cyclic voltammetry studies on Pb metals in three-electrode arrangements. Zhang [48] found $PbSO_4$(O) to have a nearly six-fold increase in charge transfer resistance over $PbSO_4$(R). Impedance studies hinted at greater degrees of reversibility of $PbSO_4$(R) obtained from $PbO_2$ reduction, providing preliminary evidence to suggest that transformation of $PbSO_4$(O) to $PbSO_4$(R) could constitute a battery recovery procedure. Karami [45], proposes that inverse charging is beneficial to both the positive and negative electrodes as a desulfation practice, allowing for the reintroduction of greater surface area and discharge capacity. NAM contains less surface area (0.5-1 $m^2/g$) than PAM (4–5 $m^2/g$), and surface area increases can provide higher NAM utilization than is achievable through carbon additions alone. The extent to which discharge capacity improvements in positive and negative electrodes are attributable to desulfation or to surface area increases remains unclear.

Zhang [48] and Karami [46] undertook inverse charging on sulfated, flooded PbA batteries. At present, Karami's study offers the most complete investigation into inverse charging as a desulfation practice. Karami constructed cells of new and sulfated electrodes from discarded PbA batteries and found inverse charging recovers sulfated batteries' capacities. However, little is provided regarding these batteries' prior histories and on sulfate crystal characterization, most critically for the anode. Karami's sulfated anodes contain crystallite sizes on the order of 5 μm, whereas heavily sulfated negative electrodes could be expected to have crystals on the order of 20–70 μm or more [51]. We therefore expanded on the research of Zhang [48] and Karami [46] and present improved protocols.

With safety as the underlying concern, patents for chargers for PbA units with "reverse polarity protection" abound [52]. With the first evidence of a patent on the technique found in

1997 [53], several advances in utilizing inverse charge techniques were made in 2009 [45,46]. Boivie [53] filed a patent on the method of eliminating sulfation on the negative electrodes and battery separators through “reverse polarity recharging” or “reverse pulse charging”. The first technique employs incremental potentiostatic voltages to temporarily reverse electrode polarity after a 20% capacity fade is reached. Another brief study proposed that inverse charging could serve as a possible workaround to positive electrode grid corrosion by allowing for battery use in a reversed polarity state after a defined period of time [54]. None of these studies examine the longevity and effectiveness of inverse charging for battery systems outside of proposed claims.

Inverse charging (or reverse polarity charging) suffers from a lack of comprehensive scientific investigations on sulfate crystal removal, safety issues, and negative consequences introduced by the technique. Inverse charging of PbA batteries presents a promising electrochemical desulfation and electrode formation practice. Of the studies that have considered it, an experimental focus has been restricted to cyclic voltammetry [48,50] and on batteries that have undergone uncertain degrees of sulfation [45,46].

### 1.5.2. Multilayer oxidation during inverse charging

As a means of understanding anodic oxidation of Pb electrodes, we adopted the simplified model of Codaro and Vilche [55], given as Eqns. 1-27 – 1-31, with the detailed anodic oxidation sequence illustrated in Figure 1-10 that was adapted from Stewart and Bennion [17], based on works of Pavlov, Valerioté, and Ruetschi [56–59]. At overvoltages from -0.97 to -0.40 V versus $Hg/Hg_2SO_4/H_2SO_4$, the Pb electrode surface is progressively discharged and covered in $PbSO_4$ through a dissolution-precipitation mechanism (Eq. 1-27). $PbSO_4$ crystals coalesce and passivate the electrode after reaching a critical thickness (Figure 1-10a), creating a structure impermeable to $SO_4^{2-}$ and $HSO_4^-$ ions, while remaining permeable to $Pb^{2+}$, $H^+$, $OH^-$, and $H_2O$. Subsequently,

$OH^-$ ions migrate inward to maintain electroneutrality, and basic lead sulfates form in the alkaline interior pore structure. α-PbO (tet-PbO) forms in an alkaline pH at -0.4 – +0.9 V, (Figure 1-10b). Hydrolysis of these α-PbO layers occurs above +0.9 V (Eq. 1-28) and α-PbO layers are converted to α-$PbO_2$ through a $PbOH^+$ intermediate near the lead surface [17]. Pavlov speculates that $Pb^{2+}$ from the lead surface and $O^{2-}$ diffusion participate in tet-PbO and α-$PbO_2$ growth [59], while Valerioté [58] includes $Pb^{2+}$ diffusion from the base of the lead sulfate layer as contributing sources for growth of α-$PbO_2$ filaments (Fig. 1-10c). α-$PbO_2$ filaments grow to consume α-PbO and basic sulfates at +1.0 V, subsequently dropping electrode pH. When this process is complete, sulfates near the α-$PbO_2$/$PbSO_4$ interface react with water to produce β-$PbO_2$ (+1.1 V) that deposit on underlying α-$PbO_2$ (Fig. 10d). When this has occurred, $PbSO_4$ is continuously oxidized until fully converted to β-$PbO_2$, while oxygen evolution occurs simultaneously at the electrolyte interface (Eqn. 1-31).

$$Pb + HSO^- \leftrightarrows PbSO\ (O) + H^+ + 2e^- \quad (1\text{-}27)$$

$$PbO + H_2O \leftrightarrows \alpha\text{-}PbO_2 + 2H^+ + 2e^- \quad (1\text{-}28)$$

$$2H^+ + 2OH^- \leftrightarrows 2H_2O \quad (1\text{-}29)$$

$$PbSO_4 + 2H_2O \leftrightarrows \beta\text{-}PbO_2 + H_2SO_4 + 2H^+ + 2e^- \quad (1\text{-}30)$$

$$2H_2O \rightarrow O_2 + 4H^+ + 4e^- \quad (1\text{-}31)$$

When this oxidation process is completed, the two zones of $PbO_2$ eventually meet as in Figure 1-10e, and constant oxygen evolution kinetics catalyzed by β-$PbO_2$ provides an indicator that Pb oxidation reactions are, for all practical purposes, finished. A similar sequence occurs in reverse, where $PbO_2$ structures are first reduced to $PbSO_4$ and α-PbO. Temporarily alkaline environments create diffusion potential gradients that allow for α-PbO reduction at -0.8 V, prior to $PbSO_4$

reduction at the outer layers to Pb metal at approximately -1.0 V [60].

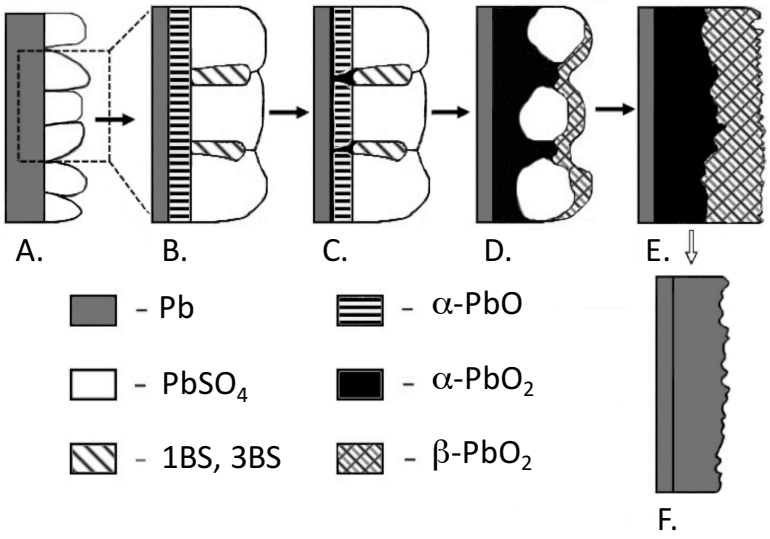


**Figure 1-10:** Anodic oxidation sequence on lead metals. Progressive oxidation is indicated with black arrows. Reduction process from stage "E" back to lead metal depicted with a white arrow. Adapted from Ref. [17].

Pavlov mathematically demonstrates the process of pore alkalization in Figure 1-10b. During discharge, the concentration of sulfate ions depletes ($C_{Pb^{2+}} > C_{SO_4^{2-}}$), and α-PbO formation is observed during in-situ x-ray analysis under potentiostatic oxidation from -0.45 – +0.8 V [56]. Stewart and Bennion model this inhibition of mass transfer caused by $PbSO_4$ growth [17]. The model studies the mass transport and reaction kinetics taking place after $PbSO_4$ passivation. The concentration of relevant species ($H^+$ and $HSO_4^-$ and $OH^-$) is studied as a function of time and position within a $PbSO_4$ pore, under a constant applied potential (+0.28 V), Figure (1-11).

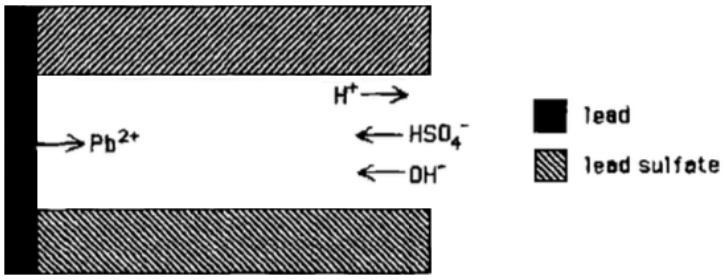


**Figure 1-11:** 1-D pore model for dissolved species flux during oxidation at +0.28V after passivation. Ref. [17]

The model calculates a variation in ionic strength at the lead/solution interface that approaches zero upon discharging. Considering a bulk concentration of 1M $H_2SO_4$, the concentration of $H^+$ near the reaction base as a function of time and position is plotted in Figure 1-12. After only 2099 ms of polarization at +280 mV, the concentration becomes alkaline at $2 \times 10^{-8}$ M $[H^+]$, and an ionic strength dropping to $10^{-5}$ M. $[H^+]$ and $[HSO_4^-]$ decreases further beyond this point, resulting in large electric fields responsible for water splitting.

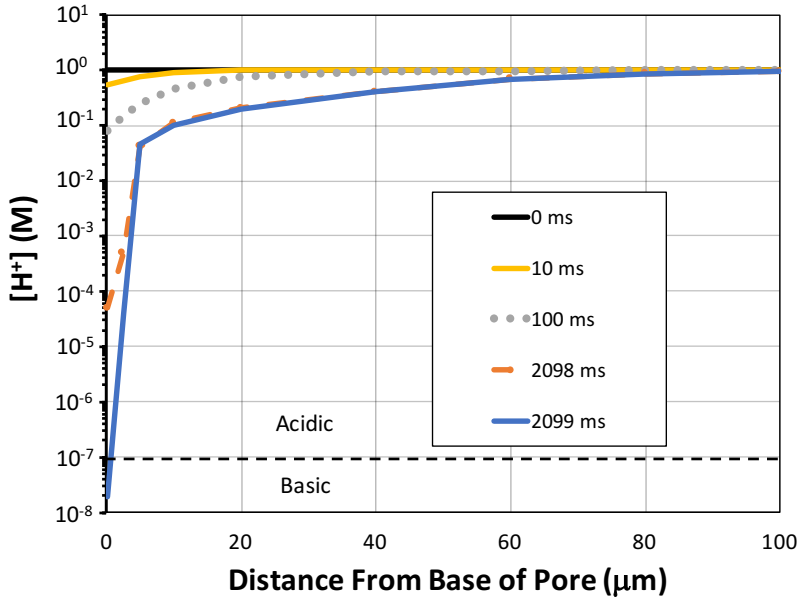


**Figure 1-12:** Concentration of $H^+$ ions at the reaction interface during anodic polarization at +0.28V. Ref. [17]

Alkalization develops rapidly near the lead surface, with the greatest change occurring during short intervals (between 2099 ms and 2098 ms). In pore structures, current densities can reach as high as 5 – 10 A $cm^{-2}$ after sufficient portions of the electrode surface are blocked by $PbSO_4$. Because the precipitation of basic lead sulfates and hydroxides is very slow, the electrode is rapidly polarized to the $PbSO_4/PbO_2$ plateau at +0.9V (figure 1-10 c,d) [56].

# 2. Technoeconomic analysis

While it is uncertain that PbA chemistries will occupy a longstanding position in EV and HEV applications, advanced PbA (ALAB) batteries can deliver performance parameters that approach or exceed competing battery chemistries for grid-based applications (lithium, zinc, sodium, vanadium, etc). To model the status of PbA and ALAB systems and the impact of inverse charging on the application economics, a thorough levelized cost of energy (LCOE) analysis is conducted. LCOE data for PbA and ALAB batteries is compared to that of competing technologies under various energy storage scenarios. Additionally, the impact of industry estimated 5-year cost reductions on battery and plant costs is considered [61]. Subsequently, the impact of inverse charging is modeled through assumed specific energy and cycle life improvements to PbA and ALAB batteries.

Schoenung [62] differentiates energy storage application areas into the four categories of use presented in Table 2-1.

**Table** 2-1**:** Categories of energy storage implementation, according to Schoenung [62].

| Use cases | Discharge time (h) | Cycles/year | Application |
|---|---|---|---|
| 1. Long duration, frequent | 4-8 | 250-350 | Bulk energy management |
| 2. Long-duration, infrequent | 4-8 | ~20 | Capacity credit |
| 3. Short-duration, frequent | 0.25-1 | >1000 | Ancillary services, frequency regulation |
| 4. Short-duration, infrequent | 0.25-1 | ~20 | Ancillary services, power quality |

Consideration is restricted to use cases undergoing frequent cycling (cases 1 and 3), to model the impact of inverse charging on battery economics in cycled applications as opposed to the economics of standby operation. To capture the effect of economies of scale (e.g. utility vs. residential) we consider applications that range in discharge duration and capacity, with details outlined Table 2-2 using data adapted from Lazard [61].

**Table 2-2:** Energy storage system application parameters used for LCOE modeling.
*A battery cycled at 10% DOD 48 times a day is rated at 4.8 100% DOD cycles/d.

| Application | Capacity (MW) | Project life (yrs) | Discharge time (h) | 100% DoD cycles/day* | Days/year |
|---|---|---|---|---|---|
| Transmission System | 100 | 20 | 8h | 1 | 300 |
| Frequency Regulation | 10 | 20 | 0.5 h | 4.8 | 350 |
| PV Integration | 2 | 20 | 2 h | 1.25 | 350 |
| Commercial &Industrial | 1 | 10 | 4h | 1 | 350 |
| Residential | 0.005 | 10 | 2 h | 1 | 300 |

Zakeri [63] finds that battery systems typically have a maximum calendar (standby) lifetime of approximately 15 years, while electromechanical energy storage systems, such as flywheels, compressed air energy storage (CAES) and pumped hydro storage (PHS) have lifetimes that well exceed 20-yr project timelines. To focus analyses on the impact of cycle life on financing, all storage system calendar life is assumed to be equal to the project life.

Applications are further classified into residential (1-10kW), commercial and industrial applications (C&I, 50kW-1MW), and utility (>1MW) in an effort to illustrate the impact of changing balance of system (BOS) costs from sector to sector [64].

## 2.1. Storage technologies considered

The most promising commercial or near-commercial battery technologies are considered in this analysis: Li-ion, traditional lead-acid (PbA), advanced lead-acid (ALAB) available in VRLA and flooded formats, sodium sulfur (NaS), zinc-hybrid (Zn-Hyb), and vanadium redox flow batteries (VRFB or Flow). For the most part, these systems correspond to those analyzed in previous assessments [62,65,66], with the exception of Zn-Hyb that was only considered by Lazard [61]. Commercial and near-commercial non-battery storage technologies considered include CAES and PHS for bulk energy storage (Transmission), and flywheels for frequency regulation applications. The technologies considered for the applications of Table 2-2 are included in Table

2-3 below [62].

**Table 2-3:** Energy storage technologies considered for each application category

| Application | Appropriate storage technology |
|---|---|
| Transmission System | PbA, ALAB, Li-ion, NaS, Flow, Zn-Hyb, PHS, CAES |
| Frequency Regulation | ALAB, Li-ion, Flywheel |
| PV Integration | PbA, ALAB, Li-ion, NaS, Flow, Zn-Hyb |
| Commercial &Industrial | PbA, ALAB, Li-ion, NaS, Flow, Zn-Hyb |
| Residential | PbA, ALAB, Li-ion, Flow, Zn-Hyb |

NaS systems are only designed for 6-8 h discharge times and are therefore not suitable for applications other than C&I and Transmission, but they are included in PV Integration analyses for comparison purposes [64]. Zinc-Air systems were excluded from analyses due low voltage output, low recharge speed and poor roundtrip efficiency; technical challenges that would preclude these systems from cycling applications in reality [67]. Zn-Hyb, NaS and VRFB systems are not suitable for frequency regulation applications due to inadequate response time, and other practical restrictions. Li-ion batteries are available in many different formats, and are studied in general. This technology is compared against PbA and ALABs across all application categories.

## 2.2. Levelized cost of energy methodology

To provide a uniform framework for cost comparison, the revenue requirements in $/kWh of energy delivered is used as a basis. This represents the amount an energy provider (utility or independent power producer) would need to charge to cover all costs associated with operating and owning a system. Revenue requirements, or the LCOE, is calculated for each application over the project lifetime [68]. LCOE calculation requires amortizing all future costs at assumed discount, escalation, and inflation rates [68]. LCOE data are presentable as levelized annual costs (LAC) in $/kW-yr, or as $/kWh using the number of hours operated per year.

Total capital costs (TCC) (Eqn. 2-1) include systems costs of energy storage $C_{storage}$ ($/kWh costs), and power conversion system (PCS) and balance of plant (BOP) costs, $C_{PCS}$ and $C_{BOP}$ ($/kW costs). The battery device is a DC unit that interfaces with the AC electric grid through the PCS that operates when dispatched as source or load. The PCS is rated at the power level (kW, MW) required for the application and the energy storage unit is rated for energy content (kWh, MWh) and is capable of outputting power during the required duration, $h$. BOP costs include costs for project engineering, grid connection and auxiliary components outside of the storage subsystem and power conversion [69].

For short discharge durations, some technologies are incapable of delivering their full energy content, and the storage unit must be oversized [68]. To account for the additional cost of oversizing, a scale-factor is introduced to account for the practical energy extractable, $f_E$, for each chemistry and discharge-duration being considered.

$$TCC = C_{cap} = C_{PCS} + C_{BOP} + \frac{C_{storage} \times h}{f_E} \quad [\$/kW] \qquad (2\text{-}1)$$

$h$ = hours of discharge for the storage system
$f_E$ = Practically extractable energy for discharge time ($h$) considered (%/100).

Scaling of unit energy costs for short discharge times is particularly necessary for PbA, ALAB, Li-ion and Zn systems, as it is not possible to extract rated energies in short timeframes [68]. Oversizing necessarily results in a depth of discharge (DOD) per cycle that is less than the rated 100% (or 80% for battery systems), hence the number of 100% DOD cycles per day (Table 2-2) for these systems must be scaled based on extractable charge, $f_{SOC}$. Extractable energy and charge at various discharge rates for PbA, Li-ion, and Zn systems are determined from performance datasheets in Refs. [67,70–72]. For our purposes, the quantity of extractable energy ($f_E$) and charge ($f_{SOC}$) are assumed to be approximately equal for each device and application.

To account for the time value of money for a loan, all future costs are discounted at the borrowing interest rate, "*i*", over the project life. For corporations that consider both debt (*D*) and equity (*E*) financing, the after-tax weighted average cost of capital (*WACC*) is calculated as the discount rate, using the cost of debt ($K_d$) and cost of equity ($K_e$). *WACC* is calculated by Eqn. 2-2 [61,64]. The after-tax *WACC* is taken to be the interest rate for LCOE modeling [64].

$$WACC = \left(\frac{D \times K_d}{D+E}\right) + \left[\left(\frac{E \times K_e}{D+E}\right) \times (1-t)\right] \qquad (2\text{-}2)$$

$D$ = percentage of debt in financing (%/100),
$E$ = percentage of equity in financing (%/100),
$K_d$ = cost of debt rate (%/100),
$K_e$ = cost of equity rate (%/100),
$t$ = corporate tax rate (%/100).

To conduct an accurate LCOE, all discount rates and escalation rates (annual costs that increase by a percentage each year) must be inflation adjusted. The real (adjusted) and nominal rates are linked by Eqn. 2-3.

$$\bar{i} = \frac{(1+i)}{(1+Inf)} - 1 \qquad \overline{WACC} = \frac{(1+WACC)}{(1+Inf)} - 1 \qquad \bar{e} = \frac{(1+e)}{(1+Inf)} - 1 \qquad (2\text{-}3)$$

$\bar{i}$ = inflation adjusted interest rate (%/100),
$\overline{WACC}$ = inflation adjusted weighted average cost of capital (%/100),
$\bar{e}$ = inflation adjusted escalation rate (%/100),
$i, WACC, e$ = nominal interest rate, *WACC*, and escalation rate (%/100),
$Inf$ = inflation rate (%/100).

Levelized capital costs (LCC) are then obtained by annualizing TCC ($C_{cap}$), represented by $C_{cap,a}$, using the capacity recovery factor (*CRF*) based on the present value of money over the project life (*T*), subject to the inflation adjusted interest rate ($\bar{i}$) according to Eqns. 2-4 – 2-5.

$$LCC = C_{cap,a} = TCC \times CRF \qquad [\$/kW-yr] \qquad (2\text{-}4)$$

$$CRF = \frac{\bar{i}(1+\bar{i})^T}{(1+\bar{i})^T - 1} \qquad (2\text{-}5)$$

Annual operation and maintenance costs ($C_{O\&M,a}$) include fixed annual O&M ($C_{FOM,a}$) and variable O&M ($C_{VOM}$), which depends on the number of cycles per year ($n$) and the discharge time ($h$) for the considered application. Variable O&M can include the cost of fuel and electricity for charging as well as any losses from self-discharge.

$$C_{O\&M,a} = C_{FOM,a} + C_{VOM} \times n \times h \qquad [\$/kW-yr] \qquad (2\text{-}6)$$

Similarly, the cost of replacing energy storage systems with future cost ($C_R$) in \$/kWh can be annualized by knowing the replacement period ($t_R$) and the total number of replacements ($r$) during the project lifetime.

$$C_{R,a} = CRF \times \sum_{k=1}^{r} (1+\bar{i})^{-kt_R} \times \left(\frac{C_R \times h}{f_E}\right) \qquad [\$/kW-yr] \qquad (2\text{-}7)$$

Future disposal and recycling costs ($C_{DR}$) are cost items that are usually neglected in LCOE analysis of energy storage, however, annualized disposal and recycling costs ($C_{DR,a}$) can be calculated with Eqn. 2-8.

$$C_{DR,a} = C_{DR} \times (1+\bar{i})^{-T} \times CRF \qquad [\$/kW-yr] \qquad (2\text{-}8)$$

The present value ($PV$) of any annually recurring costs (fuel, electricity, and O&M), which changes from year to year at a constant rate (or adjusted escalation rate, $\bar{e}$) over the study period, can be obtained from Eqns. 2-9 – 2-10. Escalation rates can be positive or negative [73]. The annualized equivalent of the $PV$ can then be determined by Eqn. 2-11.

$$PV = A_0 \times \left(\frac{1+\bar{e}}{\bar{i}-\bar{e}}\right)\left[1-\left(\frac{1+\bar{e}}{1+\bar{i}}\right)^N\right] (\bar{i} \neq \bar{e}) \qquad [\$/kW] \qquad (2\text{-}9)$$

$$PV = A_0 \times N \quad (\bar{i} = \bar{e}) \qquad [\$/kW] \qquad (2\text{-}10)$$

$$A = CRF \times PV \qquad [\$/kW-yr] \qquad (2\text{-}11)$$

$A_0$ = annually recurring cost at base-date prices,
$A$ =annualized equivalent of present value,
$\bar{i}$ = inflation adjusted discount rate,
$\bar{e}$ = inflation adjusted escalation rate,
$N$ = number of time periods (years) over which A recurs.

Annualized LCC costs ($C_{LCC,a}$) are obtained through adding all previous cost items, according to Eqn. 2-12. This represents the carrying charges for capital equipment, which includes fixed and variable O&M, replacement, and the levelized cost of energy for charging.

$$C_{LCC,a} = C_{Cap,a} + C_{O\&M,a} + C_{R,a} + C_{DR,a} \qquad [\$/kW-yr] \qquad (2\text{-}12)$$

Levelized costs can then be presented as the levelized cost of electricity (LCOE) delivered if the annual operating hours are introduced according to Eqn. 2-13 [63,65,66].

$$LCOE = \frac{C_{LCC,a}}{yearly\ operating\ hours} = \frac{C_{LCC,a}}{n \times h} \qquad [\$/kWh] \qquad (2\text{-}13)$$

The cost of charging incorporates the system efficiency, Eqn. 2-14, or overall AC-to-AC efficiency, defined as the total energy in during charging ($E_{in}$) to the energy extracted from the device during discharge, $E_{out}$. It is the product of inverter-rectifier losses and battery cycle inefficiency [64].

$$\eta_{Sys} = \frac{E_{in}}{E_{in}} = \eta_{PCS} \times \eta_{storage} \qquad [kWh/kWh] \qquad (2\text{-}14)$$

The analysis conducted does not include recycling or disposal costs of spent capital equipment

and ignores the impact of self-discharge [62,63]. Additionally, this study ignores potential value streams, due to their highly market specific nature. As such, a benefit-cost analysis (BCA) framework is avoided, and no sources of revenue are considered [61]. The residual value at the end of the study life is assumed to be zero [69].

## 2.3. Current cost and cycle life data

Zakeri [63] takes energy storage cost data from numerous historical publications and then inflation adjusts them to 2015 dollars. While this may accurately reflect changes in costs of maintenance and electricity, it skews the costs for battery systems which have experienced rapid cost declines in some instances (e.g. Li-ion). Liebrich [74] and Nykvist [75] aggregate updated cost and operational survey data for Li-Ion from original equipment manufacturers and energy storage developers after validation from additional industry participants and users at the EV pack level. Cell level estimates are obtained from Ref. [76]. PCS and BOP for flywheels, PbA, NaS, Li-Ion, VRFB, and Zn batteries fall within the 450-650 $/kW range, values within the middle 50% interquartile range (IQR) of Monte Carlo simulations conducted on literature survey data by Zakeri [63]. Zakeri's data on storage costs for flow batteries, PbA and Li-ion were significantly skewed to higher values. This study therefore selectively reports data for PCS, BOP, storage, O&M and replacement costs by carefully comparing Zakeri [63], Poonpun [65,66], Jülch [77], Rastler [64], Liebrich and Nykvist [74,75], and Schoenung [62,68,69] with recent market analysis reports from Lazard [61] and others. Data from Zakeri, Jülch and Rastler are preferentially used for cycle life, power costs, storage costs and efficiency. Sources for all values are identified in Table 2-4.

**Table 2-4:** 2015 cell-level storage device cost and cycling parameters used in LCOE modeling. Battery cycle lives are rated at 80% DOD.
Sources: [1] Zakeri [63], [2] Liebrich and Nykvist [74,75], [3] Jülch [77], [4] Rastler [64], [5] IRENA [78] , [6] Bullis [79], [7] Spanos [4], [8] Schoenung [68], [9] Lazard [61], [10] Luo [80], [11] Ruetschi [27]

| Storage Device | Power ($/kW) (PCS+BOP) | Storage ($/kWh) | Cycle Life | Efficiency |
|---|---|---|---|---|
| **PbA** | 450[1] - 650[1] | 150[8] - 200[8] | 250[7] - 1500[11] | 75[3] - 80[3] |
| **ALAB** | 450[1] - 650[1] | 200[8] - 330[8] | 2000[8] - 4500[1] | 75[3] - 80[3] |
| **Li-ion** | 450[1] - 650[1] | 300[2] - 500[2] | 1000[5] - 5000[5] | 85 - 90 |
| **NaS** | 450[1] - 650[1] | 350[4] - 450[4] | 4000[4] - 5000[4] | 75[4] - 85[4] |
| **VRFB** | 1100[2] - 1180[2] | 210[3] - 367[3] | 5000[3] - 10000[3] | 65[4] - 75[4] |
| **Zn-Hyb** | 450[1] - 650[1] | 160[6] - 300[6] | 2000[6] - 5000[6] | 60[6] - 75[6] |
| **Flywheel** | 450[1] - 650[1] | 1400[1] - 4000[1,4] | >10000[4] | 93[1] - 95[1] |
| **PHS** | 1500[4] - 3000[4] | ~0[4,9] - ~0[4,9] | 20000[1] - 50000[1] | 70[1] - 82[1] |
| **CAES** | 1000[1,4] - 2000[4] | ~0[4,9] - ~0[4,9] | >10000[4] | 55[3] - 70[10] |

Traditional PbA batteries have been used for energy storage for over a century with estimated energy storage cost on the order of $150/kWh for flooded systems and $200/kWh for VRLA, values that have changed little since the mid-1990s [68]. Although VRLA format batteries are somewhat more expensive than flooded systems, the PCS for a VRLA based energy storage system will be the same as for a conventional flooded system [68]. ALAB batteries are similar in construction to traditional PbA. Schoenung [68] estimates 330$/kWh for the high end, and 200$/kWh for the low end. In 2003, Ruetschi reported PbA cycle lives of 1500 for tubular positive plates, 800 for prismatic VRLA and 100 for SLI electrodes [27]. Hence, a value of 1500 is used as the high end for PbA, and 250 in the low end using test data from Spanos [4]. Presently, the ALABC has increased the lifetime of tubular gauntlet PbA batteries for HEV and PV applications to 6300 cycles [3]. We assume a more modest cycle life of 4500 for tubular positive ALAB designs at the high end, and a 2000 cycle life reported by Schoenung in 2011 as the low end [62]. Efficiency ranges for flooded, VRLA and ALAB systems are assumed to be the same (75% – 80%).

In 2011, Li-ion batteries were reported at $500/kWh in Schoenung [68], with PCS costs slightly higher than those for lead-acid batteries, due to charge equalization challenges [68]. In

2015, costs were reported by Liebrich and Nykvist [74,75] at $300-$500, and we assume the same power system costs as PbA. Similarly, the costs of VRFB have dropped, and for this study, energy-related equipment costs of $210-367/kWh are used from 2016 [77], compared with $600/kWh in older studies [69]. Power related costs (PCS+BOP) costs for VRFB systems remain approximately double compared to other chemistries [64].

Zn technologies are not currently widely commercially deployed, and only one manufacturer for Zn-Air (Fluidic Energy) and Zn-Hyb (Eos Energy) batteries exists. Zinc-based batteries have a limited track record, and are challenged by both cycle life and efficiency [67]. Zn-Hyb technology is reportedly capable of reaching 2000 cycles and targeted to reach 5000 cycles [79].

Power related equipment costs are 70% higher for C&I applications than utility applications, and 125% higher for residential applications based on costs associated with PbA batteries across different application categories in Ref. [64]. For all systems, we express O&M costs as a percentage of capital cost, basing values on those employed by Lazard [61]. O&M data, charging data, and charging cost escalations for each technology and application considered are available in Appendix A.

## 2.4. Modeling inverse charging

The benefits of inverse charging are speculated to be twofold and are modeled as two idealized scenarios, to examine greatest realizable economic benefit. Inverse charging of PbA batteries has the possibility of 1) extending battery life during regular cycling operation through periodic maintenance, and 2) as a manufacturing step to increase the surface area of battery electrodes and improve active material utilization prior to sale.

To model scenario 1, inverse charging is conducted with an additional battery charging device using AC wall outlet power. The cost of this inverse charger is assumed take the form of a one-time capital cost purchase of $25/kWh (i.e. $200/kW for 8h transmission applications). This value is based on a $20 battery charger capable of outputting 4A at 14.4V over a 13.3 hour period (the optimal inverse charging rate), or $20/(4A×13.3h ×14.4V) ≈ $25/kWh. Additionally, we increase maintenance costs by $15/kW-yr, using the values of Schoenung [68] based on a service contract of a single person undergoing continuous monitoring of about $30K per year for a 2 MW plant. It is assumed that inversely charged PbA and ALAB systems result in a doubling of cycle life. We assume that lifetime improvements are realizable for all applications and not only the sulfation-limited applications of frequency regulation and PV integration. The cost of energy for conducting inverse charging, equivalent to a few charge cycles, is ignored.

To model scenario 2, we assume that inverse charging is integrated into regular manufacturing operations of battery electrodes at a negligible cost increase. Based on possible surface area improvements from testing data (Chapters 3, 4), we assume that inverse charging optimally results in a doubling of the specific energy density of manufactured devices. A doubling of specific energy is modeled by halving the energy storage capital costs. It is assumed that improvements in energy density are sustainable, and negligibly impact cycle life.

## 2.5. Industry estimated capital cost outlooks

Future installations of PHS are riskier and costlier as the best sites are now tapped [81]. NaS batteries have one manufacturer, NGK, and storage costs have not changed in over a decade (currently $350 - 450/kWh) [78]. The price of Li-ion battery modules for grid applications has fallen from >$1,000/kWh in 2010 to <$500/kWh today with suppliers expecting prices to fall to

225 $/kWh by 2018 [74]. Li-ion is challenging all other commercial technologies, with cycle life and efficiency superior to lower-cost options [61,74,75]. Flow batteries have better cycle life than Li-ion, but poorer efficiency and slower cost declines. Capital costs for Zn based batteries are lower than other energy storage technologies due to quoted costs' incorporation of possible future capital cost decreases [61]. Industry experts expect that Flow and Zn-based batteries will compete with Li-ion in some applications, while CAES, flywheels, and PbA are falling behind because of cost, development risk, and poorer performance [61].

Lazard [61] examined survey data and puts forth a range of expected capital cost decreases by technology by 2020. Increasing manufacturing scale, lower component prices, and capacity-boosting technologies for Li-ion within the consumer and automotive sectors has resulting in rapid decreases in capital cost and associated levelized costs of energy (e.g. Tesla Gigafactory) [82].

Today, grid-scale energy storage balance-of-system (BOS) costs average 670 $/kW. These costs include hardware like inverters and containers, soft costs like customer acquisition and interconnection, and engineering, procurement and construction (EPC) expenses [83,84]. Ortiz [84] projects a 5-year power cost (BOP+PCS) decline of 41% by 2020 from 2015. Storage BOS costs are projected to reach an average of $398/kW by 2020 through a 48% reduction in hardware cost, 31% reduction in soft cost, and 31% in EPC cost [83].

Projected median capital cost declines for select storage technologies from 2015-2020 were expressed through a compound median annual growth rate (CAGR), Eqn. 2-15. Battery technologies are expected to reach the median cost reductions given in Table 2-5 by 2020.

$$CAGR = \left(\frac{V(t_n)}{V(t_0)}\right)^{\frac{1}{t_n - t_0}} - 1 \qquad (2\text{-}15)$$

**Table 2-5:** 2020 industry estimated energy storage and power system cost reductions.

| Technology | CAGR | 5-year reduction |
|---|---|---|
| Flow Battery | -9% | -38% |
| Flywheel | -2% | -10% |
| Lead-Acid | -5% | -24% |
| Lithium-Ion | -12% | -47% |
| Zinc | -1% | -5% |
| Power (PCS+BOS) | -10% | -41% |

## 2.6. Additional financing parameters

The additional burden of taxation is determined using the debt and equity financing scheme considered in Table 2-6. A 7-year MACRS depreciation schedule is used similar to Lazard [61], a 40% corporate tax rate and property tax of 1% similar to Rastler [64], ignoring the impact of insurance costs. A financing of 20% debt at 8% cost of debt and 80% equity at 12% cost of equity is assumed [61]. This brings the estimated total tax burden to 18.47% of capital costs being financed (capital and replacement costs) for 20 yr projects (18.16% for 10 yr projects). An inflation rate of 2% was used, which is the average annual GDP deflator for the United States from 1990-2015 [85]. We assume the inflation adjusted escalation rate for fuel and O&M is zero, indicating that these costs do not escalate faster than general inflation [68]. The costs of fuel and carbon emissions for CAES systems are obtained from Zakeri [63] and Rastler [64], respectively.

The analysis conducted does not reflect the evolving rules and regulations under the EPA's Clean Power Plan [86]. Additionally, we neglect the influence of various tax subsidies, and ignore environmental consequences and associated costs.

**Table 2-6:** Assumed LCOE financing parameters.

| Model assumptions | |
|---|---|
| Debt | 20% |
| Equity | 80% |
| Debt rate (cost of debt) | 8.00% |
| Equity rate | 12.00% |
| Pre-tax WACC | 11.20% |
| After-tax WACC | 10.56% |
| Total tax | 40% |
| Inflation | 2% |
| Depreciation | 7-year MACRS |
| Property tax | 1% |
| Fuel cost ($/MMBtu) | 10-25 |
| $CO_2$ emissions (Lb/MMBtu) | 117 |
| $CO_2$ price ($/Ton) | 25-30 |

## 2.7. LCOE results

Figures 2-1 – 2-5 illustrate the results of the LCOE analysis for each application considered in Table 2-3. Anticipated capital cost reductions were not reflected in capital and replacement costs for 2015 estimates, but are captured in 2020 estimates. For each application scenario, the LCOE of relevant energy storage systems are presented alongside the LCOE of the same systems using 2020 projections of capital cost declines given in Table 2-5, and a break downs of all modeled data is available in Appendix A. Results are presented as the cost of delivered energy, $/MWh, and levelized annual costs $/kW-yr are presented in Appendix A.

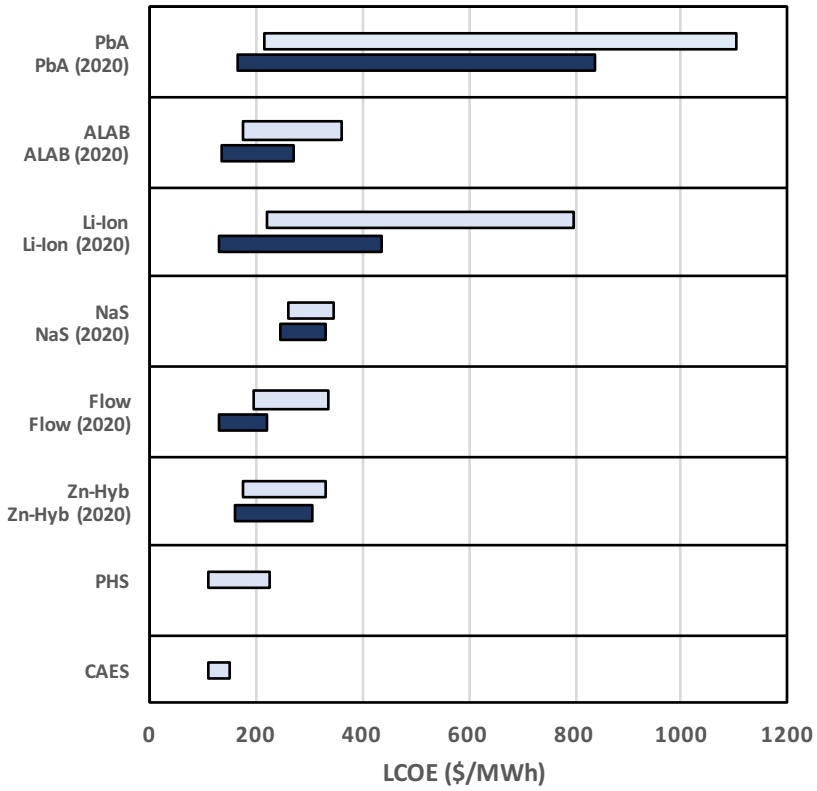


**Figure 2-1:** LCOE results for a transmission system, 20 yr life, 8 h discharge, 1 cycle/day, 300 days/yr. Light colored values represent current 2015 estimates using data in Table 2-4. Dark values use 5-yr (2020) projected cost reductions given in Table 2-6. Low-end LCOE values represent highest cycle life, highest efficiency, lowest capital and replacement cost, and lowest maintenance cost in ranges considered. The opposite applies for high-end values.

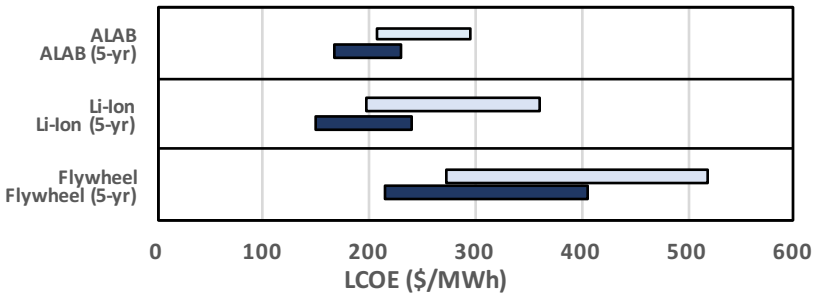


**Figure 2-2:** LCOE results for frequency regulation, 20 yr life, 0.5 h discharge, 4.8 cycles/day, 350 days/year.

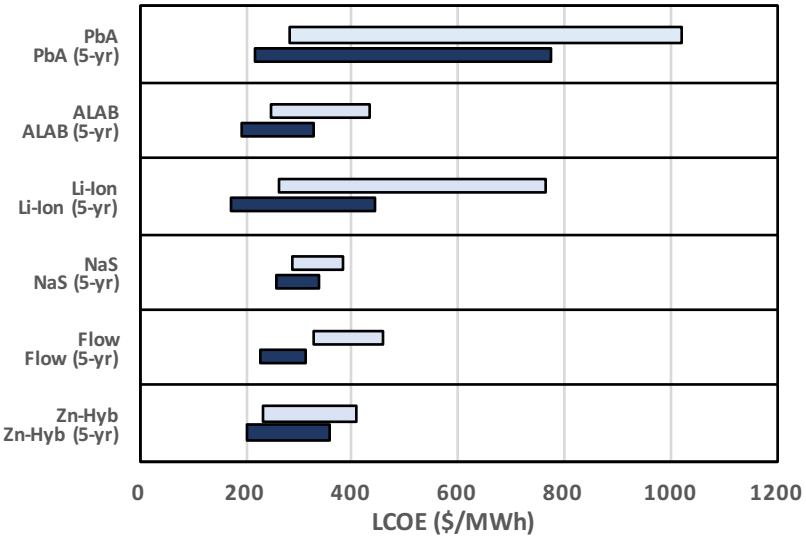


**Figure 2-3:** LCOE results for PV integration, 20 yr life, 2 h discharge, 1.25 cycles/day, 350 days/year.

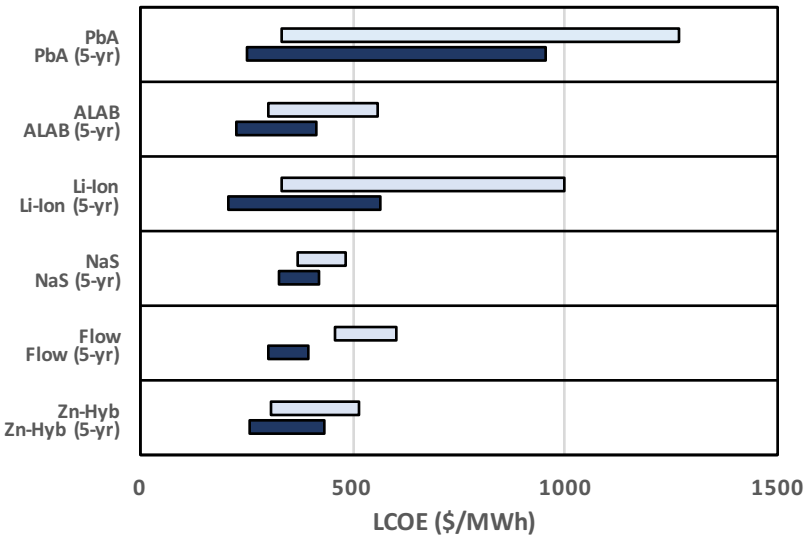


**Figure 2-4:** LCOE results for C&I, 10 yr life, 4 h discharge, 1 cycle/day, 350 days/year.

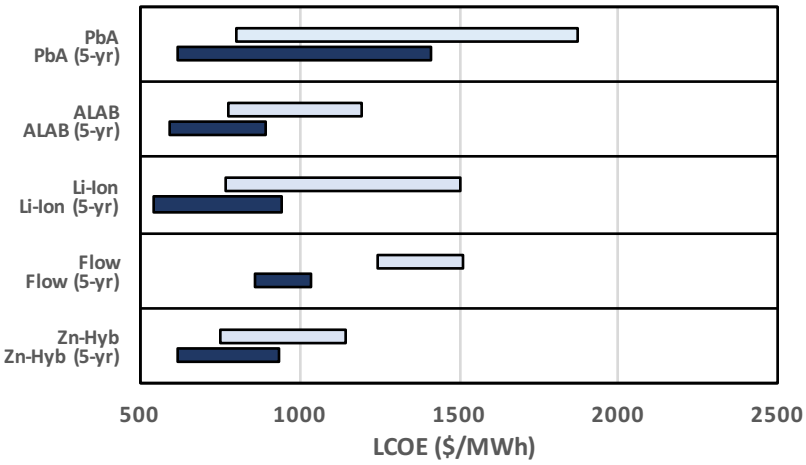


**Figure 2-5:** LCOE results for residential systems, 10 yr life, 2 h discharge, 1 cycle/day, 300 days/year.

Figures 2-6 – 2-7 illustrate the economic impact of inverse charging on PbA and ALAB systems for each application using projected 2020 costs. LCOE data for inversely charged systems are compared to the cheapest competing technology (for transmission applications we compare against both PHS and Flow systems).

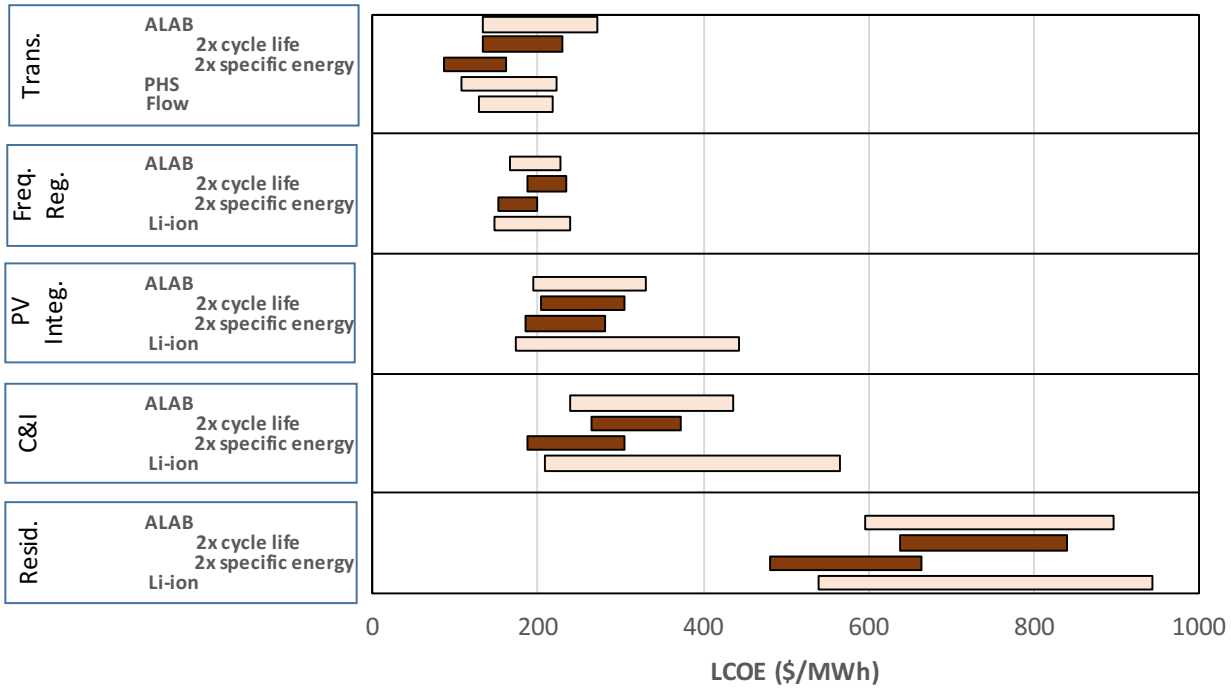


**Figure 2-6:** Future (2020) LCOE results for inverse charging scenarios of ALAB battery devices (dark values) as compared to the cheapest competing technology of each application category (light values). Low-end LCOE values represent highest cycle life, highest efficiency, lowest capital and replacement cost, and lowest maintenance cost in ranges considered. The opposite is the case for high-end estimates.

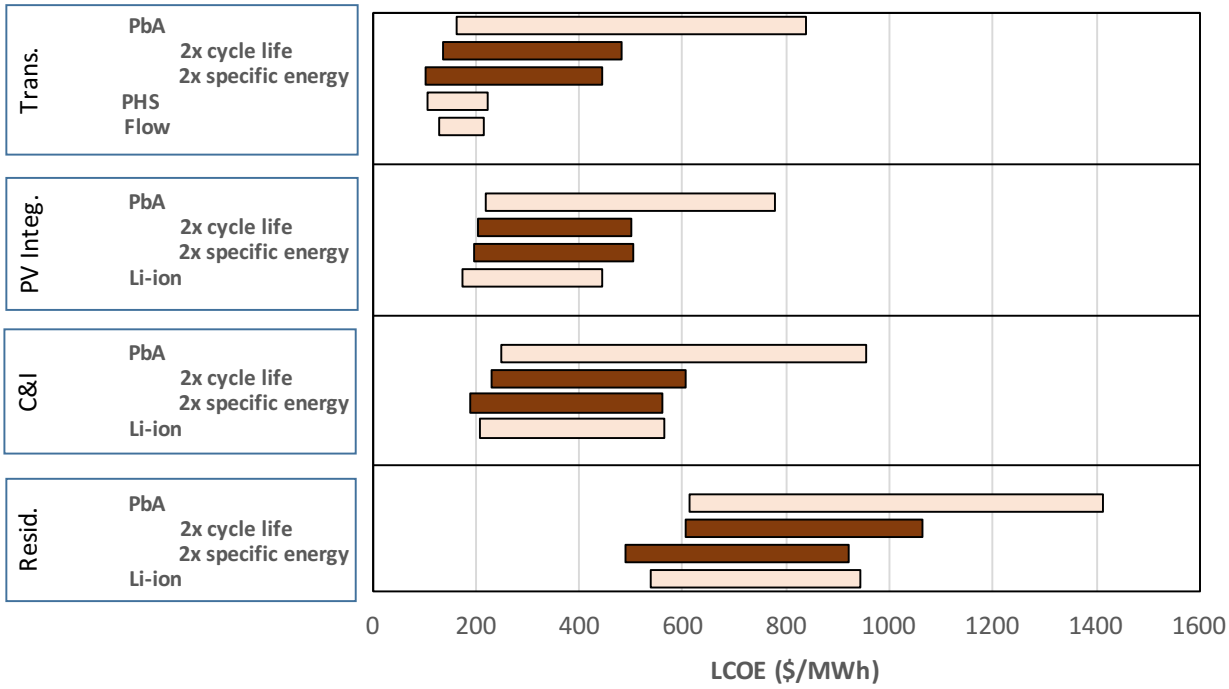


**Figure 2-7:** Future (2020) LCOE results for inverse charging scenarios of PbA battery devices (dark values) as compared to the cheapest competing technology of each application category (light values).

## 2.8. Sensitivity Analysis

To assess the impact of parameter changes in LCOE ($/MWh) calculations, a sensitivity analysis was conducted by varying discount rate (presented as after-tax, pre-inflation adjusted *WACC*) Figure 2-8. For all sensitivity analyses, extant parameters are kept the same (including the 2% inflation rate used in prior analyses) while varying the parameter of study. Figure 2-8 illustrates the impact of discount rate variations on the most relevant energy storage systems (PHS, ALAB, PbA, and Li-Ion) using 2020 cost projections for PCS and storage costs (Table 2-5) for an 8-hr bulk energy discharge transmission system application (Table 2-3). The impact of inverse charging on economics is also considered for PbA systems (presented as 2× specific energy and 2× cycle life, as outlined in *Section 2.4*). Midpoints of LCOE ranges are tracked for each system examined. From the results, variations in *WACC* significantly impact the most capital intensive

systems (PHS and ALAB systems). LCOE for systems with a lower upfront cost (PbA) increase less with increases in WACC. Dramatic reductions in capital cost for Li-Ion by 2020 make initial upfront costs within reasonable comparison to PbA, and high interest rates are seen to benefit this chemistry in a similar fashion. This has important implications for projects installed in the developing world (higher interest rates), making systems with lower upfront capital cost more attractive. By the same token, in regions with very low interest rates, highly capital intensive systems such as PHS, flow batteries and CAES systems are preferable.

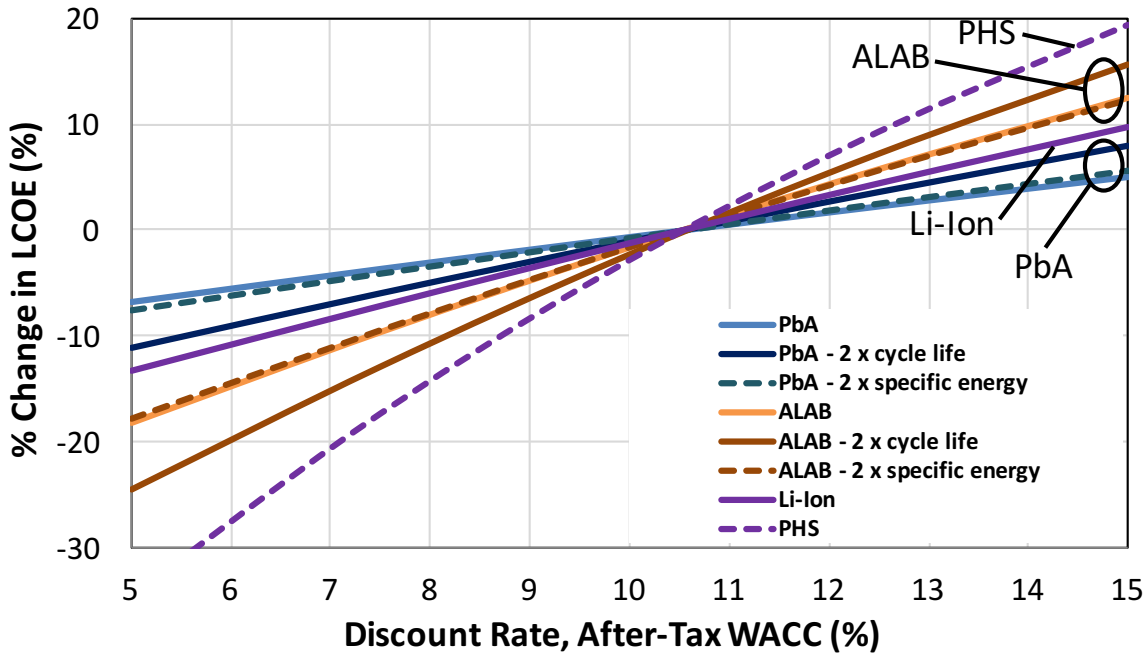


**Figure 2-8:** Average % change in LCOE as a function of discount rate for the 8 h transmission system application. 2020 projected costs of storage and balance of system are used.

Similarly, sensitivities to capital cost variations and charging cost were conducted (Figures 2-9 – 2-10). Variations in capital cost (Figure 2-9) affected all systems to the same extent in a quasi-linear fashion. The systems with lowest cycle life were affected by the greatest amount (PbA, Li-Ion) by increasing replacement costs and taxation costs. Systems with the greatest cycle lives and most infrequent replacement (ALAB, PHS) varied less.

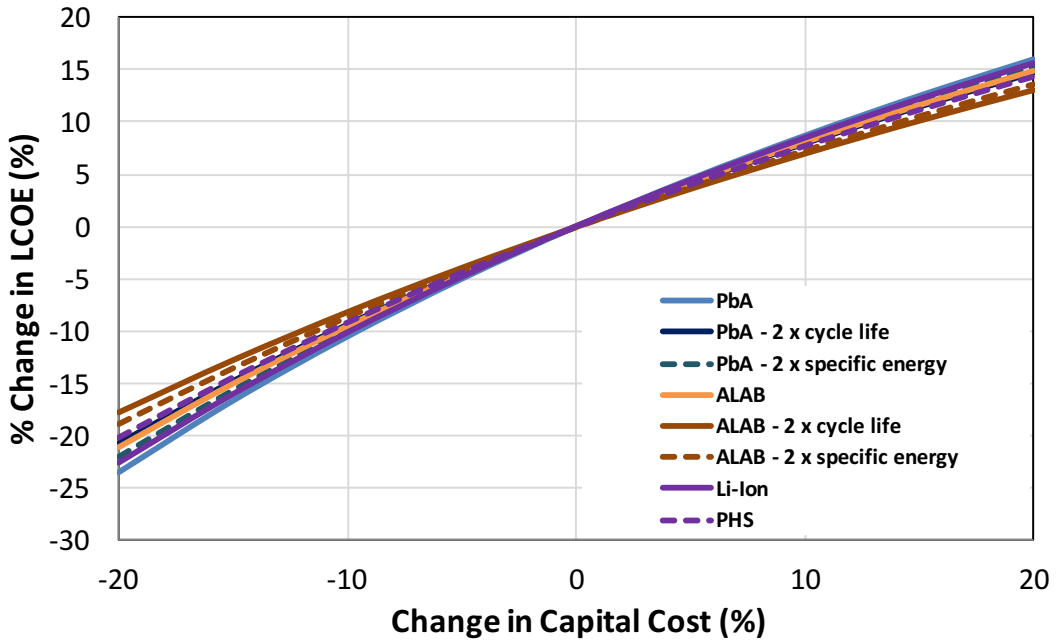


**Figure 2-9:** Average % change in LCOE as a function of % capital cost change for the 8 h transmission system application. 2020 projected costs of storage and balance of system are used.

Changes to electricity cost (Figure 2-10) linearly impact LCOE, more prevalently affecting systems with the lowest overall LCOE (PHS, ALAB, CAES) and lowest efficiencies (CAES, PHS).

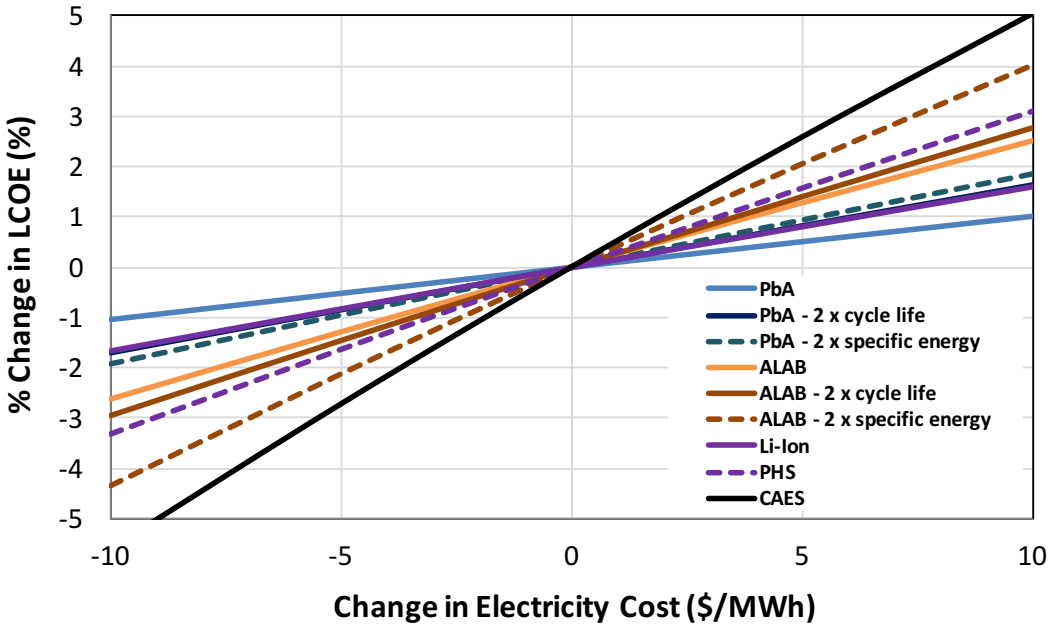


**Figure 2-10:** Average % change in LCOE as a function of incremental change in electricity charging cost for the 8 h transmission system application. 2020 projected costs of storage and balance of system are used.

## 2.9. Conclusions

A life-cycle cost comparison was performed on 9 different technologies in suitable application scenarios. Differences in capital cost and replacement, O&M, efficiency, and charging costs were considered. The LCOE follows a standard economic format, and the results indicate that batteries can address all application areas, while the least expensive option depends on the application. The most important factors influencing total LCOE are foremost upfront capital cost of the equipment and the replacement costs (depending on cycle life), followed by O&M and, finally, the recharging energy and taxation. Replacement costs significantly influence the life-cycle costs of batteries with short cycle lives (<1500 cycles), and this factor results in the greatest spread in LCOE data in Figures 2-1 – 2-5. The high spread in LCOE data for PbA and Li-ion batteries is a result of the low cycle life used on the high-end estimate (250 and 1000 respectively).

If current battery development trends are realized, large-scale bulk energy storage (transmission application) will be best handled by PHS, CAES and flow-based systems due to the low costs per kilowatt-hour (Figure 2-1). Dramatic future cost reductions for Li-ion make Li-ion preferable for all applications by 2020 (except bulk energy). Li-ion is heavily favored for the shorter duration application of frequency regulation (0.5 h) due to the requirement of much less storage capacity, and higher efficiency than lead-based systems. ALAB improvements to cycle life over PbA systems, while significant, must be paired with further improvements to the capital cost of the chemistry to ensure the future viability of the chemistry. If Zn-based chemistries are more widely deployed in the future, they serve as a close competitor to Li-ion and Pb-based batteries for renewables integration and residential systems. Zinc systems compare favorably to the other chemistries at present and in 2020, despite only minor cost declines expected.

Traditional PbA (<1500 cycles), although among the cheapest technologies upfront, have low cycle lives preventing them from being competitive in most grid applications. On the other hand, high cycle life (4500 cycles) ALAB batteries are cost competitive today and in 2020 for a variety of applications. For ALAB systems, using inverse charging to increase cycle life has a negative impact on overall economics for systems with high cycle life (Figure 2-6). The added capital cost of $25/kWh and increase to maintenance cost is not compensated by the avoided replacement costs, which are negligible for systems with cycle lives >4000. Small reductions in cost are observed for ALAB systems with a cycle life of 2000 (high end LCOE data point in Figure 2-6). For traditional PbA batteries with cycle lives <1500, inverse charging to increase cycle life works to decrease LCOE, making 1500 cycle life PbA batteries (low end LCOE point) more competitive with flow and PHS devices for bulk energy storage. On the other hand, inverse charging conducted by the manufacturing facility to increase specific energy dramatically reduces the cost of all PbA and ALAB systems (Figures 2-6 – 2-7). The cost reductions in these scenarios bring LCOE data almost to cost parity or better with PHS, and make PbA and ALAB devices either cost competitive or preferable for almost all applications in 2020.

Thus, inverse charging as a maintenance strategy should be restricted to devices with <2000 cycles and to projects with long project life (20 years) requiring more frequent replacement. Inverse charging as a manufacturing strategy (specific energy) is highly preferable in all instances. These cost-effective solutions merit an understanding of inverse charging and its influence on current battery design and failure mechanisms to inform strategies for future implementation.

# 3. Inverse charging of lead metals and porous battery electrodes

This chapter examines the impacts of inverse charging on pure lead metals and for new battery electrodes from different battery formats.

## 3.1. Experimental setup

Electrochemical investigations and inverse charging experiments were conducted with an Ivium-n-Stat 10 V, 10 A potentiostat. Battery cycling and capacity testing was undertaken on a Neware BTS 4000 10 V, 6 A designated battery cycler. Scanning electron microscopy (SEM) was conducted using a Hitachi S-4700 Field Emission SEM. A GC3000A Inficon Gas Analyzer was used for gas chromatography. Flame atomic absorption spectroscopy (FAAS) and graphite furnace AAS (GFAAS) was conducted with a Buck Scientific 200A FAA and a Buck Scientific 210 VGP GFAA. Brunner-Emmett-Teller (BET) surface area measurements were obtained through single-point BET analysis using a ChemBET Pulsar TPR/TPD (Quantachrome) unit. Powder x-ray diffraction (XRD) studies were conducted with an X'Pert$^3$ PANalytical powder diffractometer (0.035°/sec scan rate from 5 to 125 degrees 2θ). Rietveld refinement for X-ray phase analysis was conducted using X'Pert Highscore Plus, using the crystal structure information in Refs. [87–91]. Two conceptually different sets of experiments were conducted: 1) studies on pure Pb metals, and 2) studies on battery cells using new battery electrodes. All experiments were carried out at room temperature (298 °K), and all voltages are expressed with respect to an $Hg/Hg_2SO_4/4M\ H_2SO_4$ reference electrode that was pre-equilibrated in the same solution for at least 24 h (+0.62 V vs. STP $H^+/H_2$) [16,57]. Measured against the $Hg|Hg_2SO_4$ reference electrode, the reversible potential is determined to be -0.971 V, independent of acid

concentration [27].

$$PbSO_4 + 2Hg \rightarrow Pb + Hg2SO4 \quad (3\text{-}1)$$

$$E_{Pb/PbSO4} = -0.971 + \frac{RT}{nF} ln\left(\frac{a_{PbSO_4} \bullet a_{Hg}^2}{a_{Hg_2SO_4} \bullet a_{Pb}}\right) = -0.971 \ V \quad (3\text{-}2)$$

### 3.1.1. Lead rod tests

Studies on Pb metals were performed using three-electrode experiments in an H-cell (Figure 3-1). 3.25 mm diameter Pb rods of 99.98% purity from Ames Metal Co. served as the working electrodes. Annealed pure platinum wire served as the counter electrode. Electrolyte was prepared by diluting $H_2SO_4$ to 4 M with de-ionized water, pre-sparging with argon gas, and then continuously sparging at the cell bridge to minimize dissolved oxygen. Working electrodes were electrically isolated by melted paraffin under chemically resistant polyvinylchloride (PVC) heat-shrink tubing. Metallic surfaces were cleaned with acetone, microfiber polished to mirror finish, rinsed with de-ionized water, and immediately immersed in the electrolyte. Each electrode had an exposed surface area of ~2 $cm^2$.

Pb rod electrodes were subjected to galvanostatic oxidation and reduction cycling with current density normalizations based on geometric surface area. With progressive cycling, growth in discharge capacities correspond to progressive increases in surface area and hence effective reductions in applied current density. The initial 5 cycles on the flat electrode surface at the +50 μA/$cm^2$ oxidation current corresponds to a 1–3 h discharge rate; a current density in close proximity to ~0.3 $C_{20}$ currents used in PbA industry for formation of newly manufactured porous electrodes [26]. As such, Pb rods were initially formed at the +50 μA/$cm^2$ rate and subsequently at the +200 μA/$cm^2$ oxidation rate to maintain discharge times within in the 1–3 h discharge regime when attempting to form the highest surface area and capacity. Total discharge

capacity was monitored and different degrees of sulfation failure were imposed to mimic different battery states of health.

Inverse charging was conducted at the +50 μA/cm$^2$ rate until the electrode was fully discharged (–0.9 V). When monitoring current transients, electrode potential was then stepped to +1.3 V for an additional 40 hours. For constant-current (CC) inverse charging, discharging at +50 μA/cm$^2$ continued until a +1.3 V cutoff, and held subsequently at +1.3 V until current transients plateaued in ~20 h (Figure 3-2). Pb electrodes were then reduced at the -200 μA/cm$^2$ rate to a –1.1 V cutoff and subsequently held until current transients equilibrated (plateaued) as part of a CCCV charge protocol.

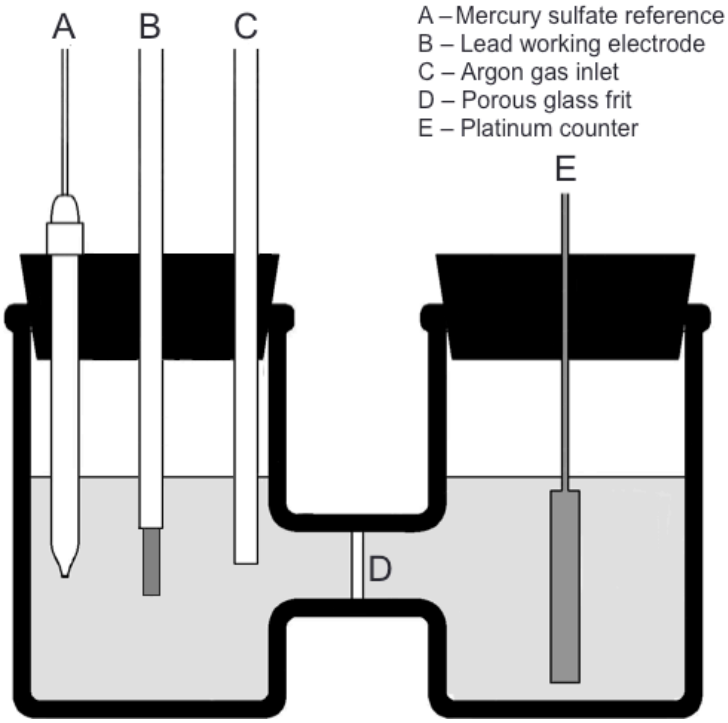


**Figure 3-1:** Three-electrode setup for studies on Pb metals.

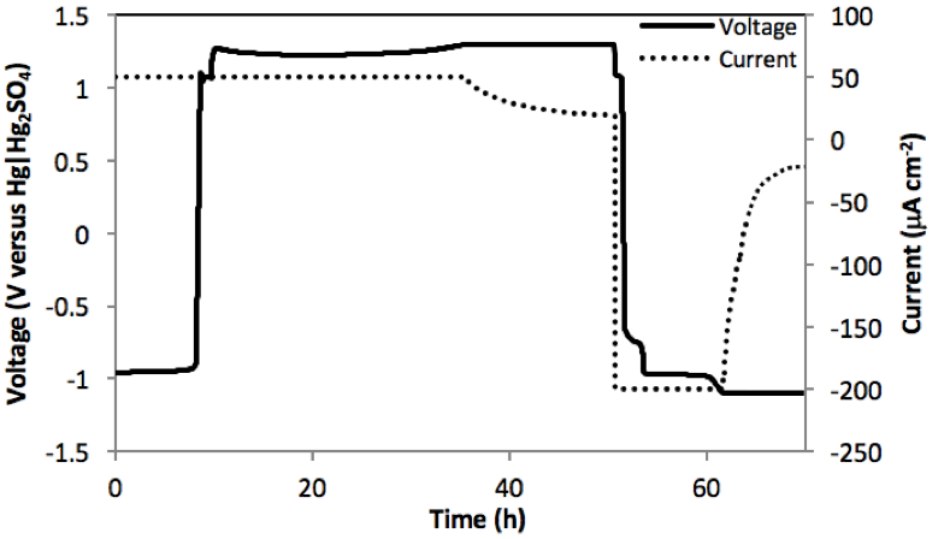


**Figure 3-2:** Inverse charging voltage and current protocol employed for Pb metals in 3-electrode cells. Inverse charging is conducted at the +50 µA/cm$^2$ rate and reduced at the -200 µA/cm$^2$ rate.

### 3.1.2. Studies on battery electrodes

Studies on battery electrodes were conducted on anodes and cathodes sourced from new OEM 12 V, 1.4 amp-hour (Ah) PowerSonic (model no. PS-1212) sealed VRLA batteries and on OEM 6 V, 2 Ah Yuasa (model no. 6N2–2A) flooded batteries. PowerSonic battery electrodes are constructed with three ~0.7 Ah Pb-Ca grid alloy negatives and two ~0.95 Ah Pb-Ca-Sn grid alloy positives. Flooded Yuasa batteries consist of two ~1.6 Ah Pb-Ca negatives and one ~1.3 Ah Pb-Sb positive per cell.

Yuasa Pb-Sb batteries were amenable to inverse charging due to flooded electrolyte construction, allowing full electrode polarity reversal. These batteries were studied as packaged, filled with 4.64 M $H_2SO_4$ and not deconstructed. PowerSonic VRLA battery electrodes were extracted and absorbed glass mat microfiber separators were removed and discarded. Equivalent flooded-cell batteries were reconstructed in beaker format as illustrated in Figure 3-3. Each battery cell was constructed by placing the electrodes in the exact configuration corresponding to its VRLA origin: three negative electrodes, and two positive electrodes. All reported C-rates are

based on nominal battery capacities. Traditional ribbed Daramic microporous polyethylene was used as separator material from Amerace Microporous Products [92,93]. Separator ribs were oriented toward the positive electrode. Electrodes were connected to 99.98% pure Pb foil current collectors from Ames Metal Co., with fluxless Pb welds. Joints were encapsulated in epoxy and acrylonitrile butadiene styrene (ABS) resin to provide structural support and to eliminate possible corrosion conductivity losses. Sandwiching the entire arrangement between two Teflon endplates ensured electrode compression, and the setup was fastened with Tefzel™ chemically inert zip-ties. Additional separators were placed between end electrodes and compression plates to ensure complete electrolyte contact. The completed cells were immersed in beakers of 70 mL pre-sparged 4 M $H_2SO_4$, constituting an excess electrolyte environment.

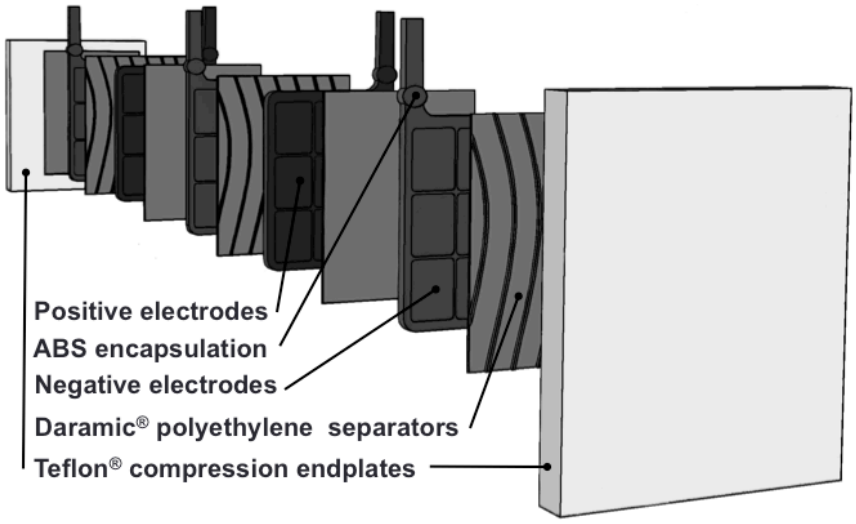


**Figure 3-3:** Exploded model of battery construction.

Karami [45,46] determined that inverse charging at current densities close to the $C_{20}$/13.3 rate (3A for batteries with nominal capacity of 40 Ah rated at 20 h discharge currents) were optimal at capacity improvement post-inverse charging. $C_{20}$/13.3 brought about the greatest relative percentage increase in battery discharge capacity (average increase of 85% over initial $C_{20}$/20 capacity) [46]. Karami employs a time limit on inverse charging of 24 hours prior to recharging.

This hard criterion can prevent reactions from going to completion, especially at the recommended lower current densities. Doing so can limit the amount of anodic oxidation and consequently lessen the degree of $PbSO_4$ conversion (the proposed mechanism), leading to mixed conclusions about optimum current densities and capacity recoveries.

Karami directly recharged inversely charged batteries using a very aggressive constant voltage of +2.66 V. However, imposing high voltages immediately after polarity reversal may result in dangerously high currents that can disrupt electrical equipment and possibly damage the electrodes themselves. This practice was decided against for our purposes, and a less aggressive constant-current to constant-voltage (CCCV) charging algorithm was utilized.

Battery cells were inversely charged per a 4-step protocol: 1) discharged at the $C_{20}$/13.3 rate until polarity was reversed and cell voltage reached –2.45 V, 2) held at –2.45 V for 24 h, 3) recharged at the $C_{20}$/13.3 rate until a +2.45 V cutoff, and 4) held at +2.45 V until a $C_{20}$/35 current limit. A 24 h CV hold proved to be an adequate time for current transients to equilibrate and plateau for all studied batteries, signifying that oxidation of the negative plate group was completed and oxygen evolution was initiated.

In addition, inverse charging on individual battery electrodes was conducted by means of an H-cell analogous to Figure 3-1. For these setups, constant-current (CC) inverse charging was conducted in 4-stages: 1) oxidation at the $C_{20}$/13.3 rate until fully discharged (-0.8 V), 2) continued oxidation at the $C_{20}$/13.3 rate for 20 h, 3) CC reduction at the $C_{20}$/13.3 rate until -1.1V, 4) -1.1V hold until current transients equilibrated.

## 3.2. Results and discussion

### 3.2.1. Lead rod inverse charging experiments

First cycle inverse charging reveals differences from cycled Pb metal electrodes. For a cycled electrode, (Figure 3-4a), capacity is seen to increase with each cycle due to progressive surface roughening and active material formation resulting in electrode surface area increases. For inversely charged rods (Figure 3-4b), capacity is seen to increase by a similar quantity, while average discharge voltages are seen to occur several mV lower, closer to the reversible $Pb/PbSO_4$ potential, indicating lower overvoltages.

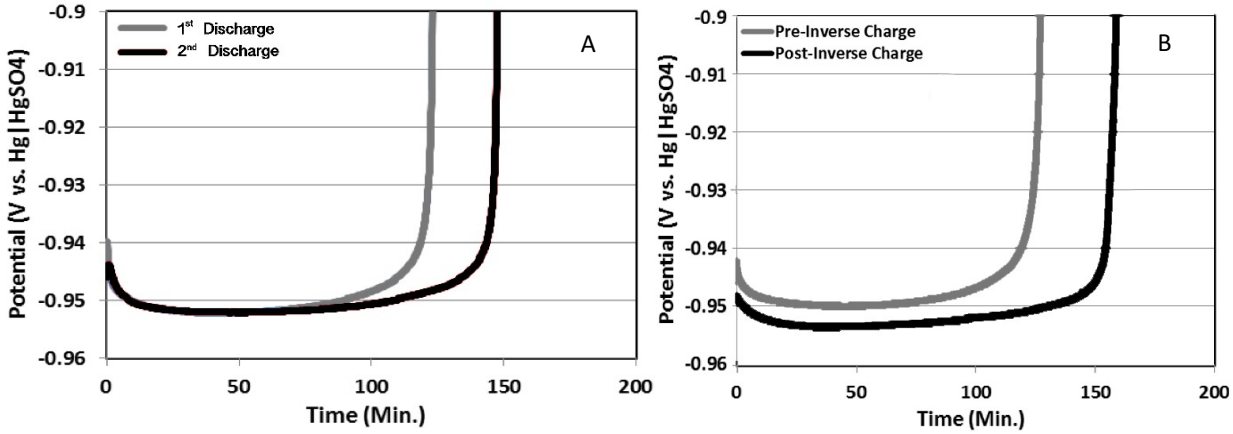


**Figure 3-4:** Pb rod discharge voltage data at the +50 μA/cm$^2$ rate A) during regular cycling, B) pre- and post-inverse charging. Rods are charged before each cycle at the -200 μA/cm$^2$ rate and held at -1.1V for 3600 s.

Identical Pb rods were cycled galvanostatically, and four different battery states of health were analyzed, each representing increasingly pernicious forms of sulfation, with results presented in Figure 3-5. For Test 1, Pb rods were galvanostatically oxidized and reduced at +50 μA/cm$^2$ and –200 μA/cm$^2$ respectively, for the first 15 cycles, and +200/–400 μA/cm$^2$ for subsequent cycles. Test 2 subjected rods to +50/–200 μA/cm$^2$ for the first 5 cycles, +200/–400 μA/cm$^2$ for 15 cycles, allowed rods to rest at open circuit for 2 weeks at a discharged state, and continued cycling at +200/–400 μA/cm$^2$ thereafter. Test 3 subjected rods to continuous +50/–200 μA/cm$^2$

cycling. Rods in Test 4 are cycled at +10/–200 μA/cm$^2$.

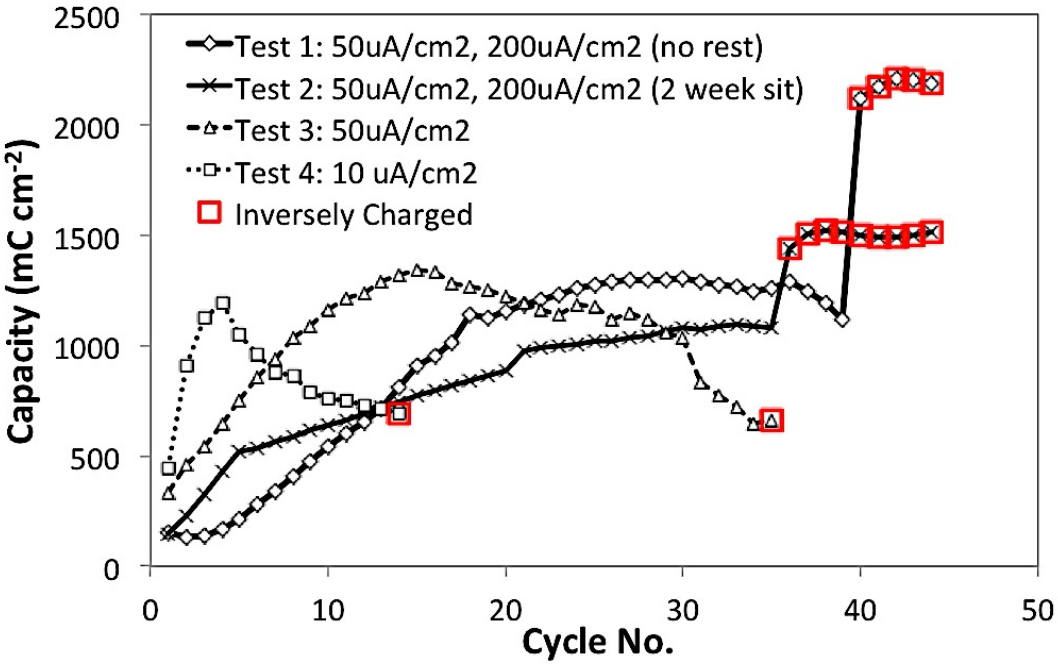


**Figure 3-5:** Discharge capacity studies on pure lead metal. All studies are conducted in 4 M $H_2SO_4$ electrolyte. Charging protocol: CCCV charge at 200-400 μA/cm$^2$ to a -1.1 V cutoff held for 3600 s. Discharge protocol: CC discharge at 10-200 μA/cm$^2$ to a -0.9 V cutoff.

Two competing processes are observed for Pb rod tests: electrode capacity growth and sulfation processes occur simultaneously. Knehr [18] shows that slow discharge rates correlate closely with large $PbSO_4$ crystallites that are difficult to reduce. Slow discharge rates are observed to form flat densely packed crystal arrangements that more effectively impede transport.

By keeping discharges within 1–3 h rates, Pb rod cycle lives can be significantly extended, and capacities can well exceed 2000 mC cm$^{-2}$. As such, Tests 1–2 see longer cycle lives than Tests 3–4 before capacity declines are observed. These Pb rods plateau in capacity growth and exhibit capacity declines after 33–36 cycles. Rods in Tests 3–4 are cycled at much slower rates than the 1–3 h discharge time as cycling progresses. In addition, Pb rods for Tests 3–4 are cycled to ~50% of peak capacity. 80% of peak capacity is a widespread performance criterion in the battery industry signifying the device's end-of-life, and the 50% value used is

aggressive [4].

Inverse charging is conducted per the protocol described in section 3.1.1. Current transients are monitored during the +1.3 V hold (Figure 3-6) and indicate that oxidation peaks at significantly higher values in Test 2 than in Tests 3–4, plateauing much more rapidly as oxidation is completed sooner. As such, these transients provide visual evidence for the decreasing quantities of reactive surface area in consecutive tests.

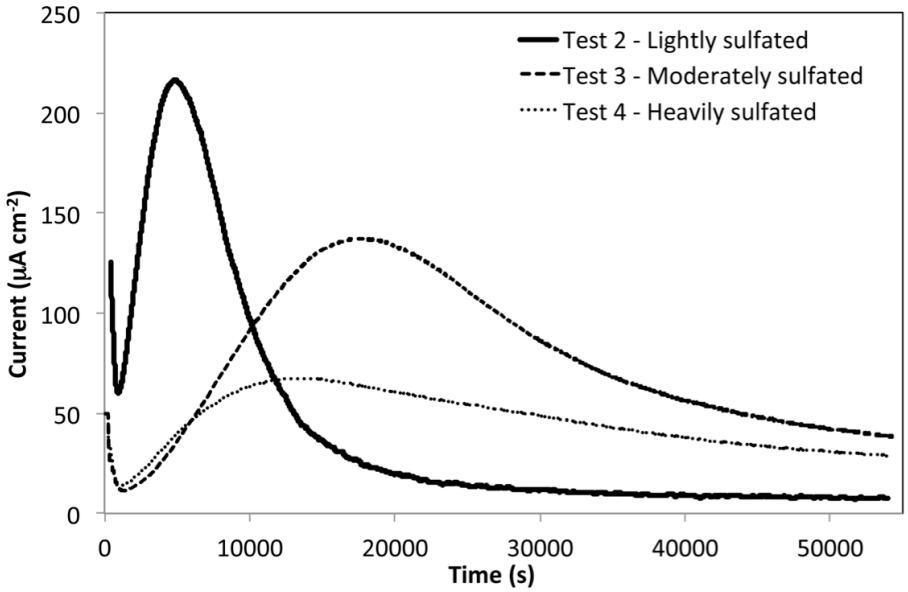


**Figure 3-6:** Current transients for Tests 2-4 during +1.3 V CV hold of inverse charging.

It is observable that inverse charging can reduce sulfate coverage and enhance battery capacity with success directly related to the initial degree of sulfation. For Test 1, capacity after inverse charging increases 90% over base values, while those for Test 2 increase 34%. Tests 3 and 4 are not seen to adequately oxidize $PbSO_4$ crystallites. After inverse charging, capacities for Tests 3–4 are seen to decrease with cycling, or voltages drifted between –0.4 and –0.6 V and electrodes are not able to store charge.

Microscopic images of the Pb rods for the various tests were obtained via SEM (Figure 3-7). The capacity and corresponding cycle number for each image is depicted in the inset. Prior to

taking each image, rods were fully charged to −1.1 V and then held at the −1.1 V reducing potential for 5 h. Rods were subsequently removed from solution, washed in DI water and acetone, and imaged within 20 min. All images are presented at the same magnification of 5,000×.

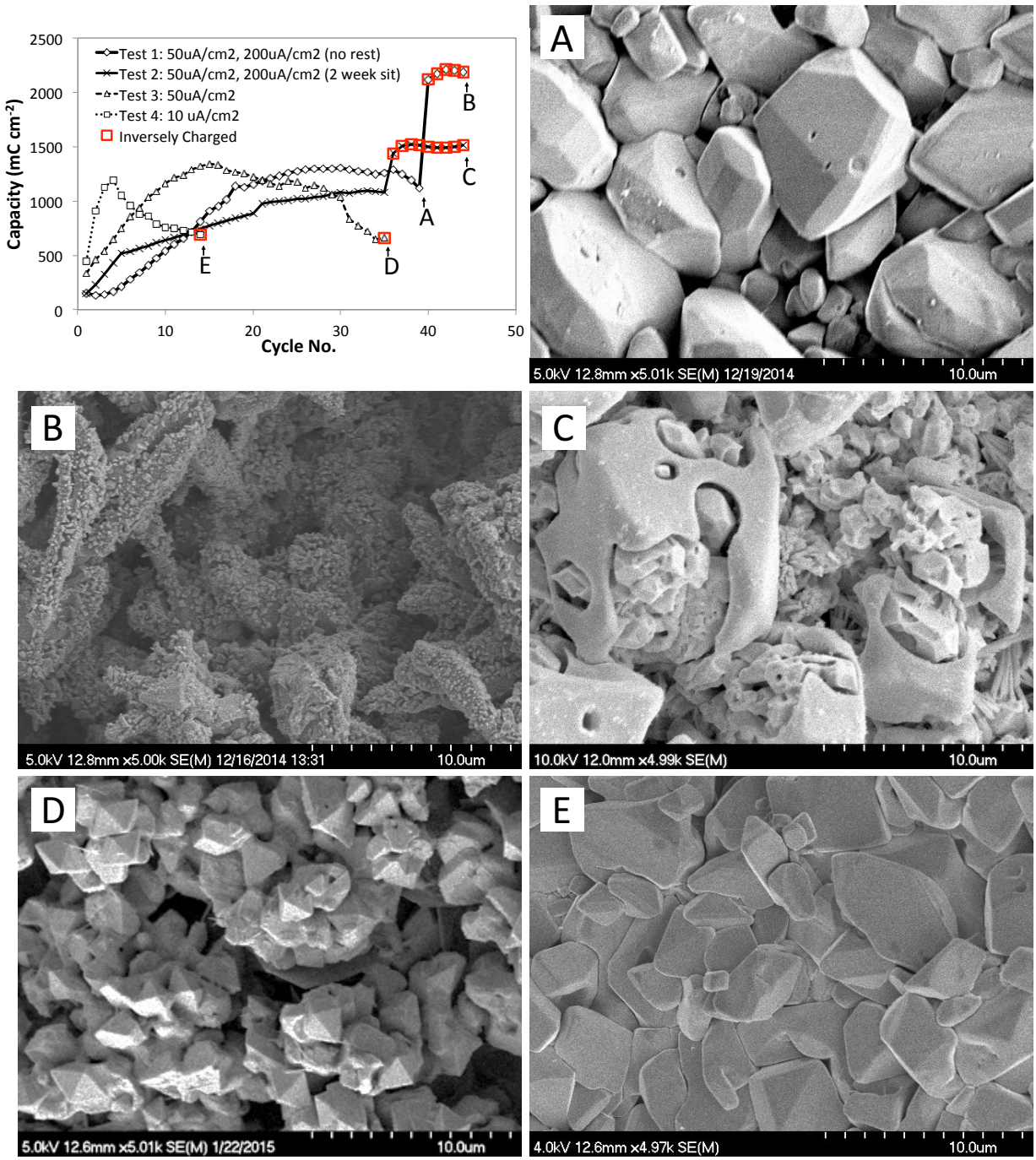


**Figure 3-7:** SEM micrographs of Pb active material. **a)** Test 1: fully sulfated. **b)** Test 1: post-inverse charging. **c)** Test 2: post-inverse charging. **d-e)** Test 3-4: post-inverse charging.

As is evident from Figure 3-7b, clear morphological changes are observable in the Pb crystal structure post inverse charging with well-connected outwardly protruding growths. Sulfate crystals are observed to range from 20–70 μm at point "A", and range from 2–5 μm, five cycles post-inverse charging at Point "B". Significant enhancements in reactive surface area are also evident. Inverse charging for Test 3 was seen to only produce superficial oxidation of large $PbSO_4$ crystallites, whereas Test 4 yielded no discernable oxidation.

Discharge voltage curves for Test 2 are normalized as a function of state of charge (SOC) in Figure 3-8. The average discharge voltage post-inverse (discharge 36) occurs a few mV lower than discharge voltages immediately after the two week sit (discharge 21) or 14 cycles after this point (discharge 35). This behavior is like observations on inversely charged Pb electrodes on the first cycle in Figure 3-4.

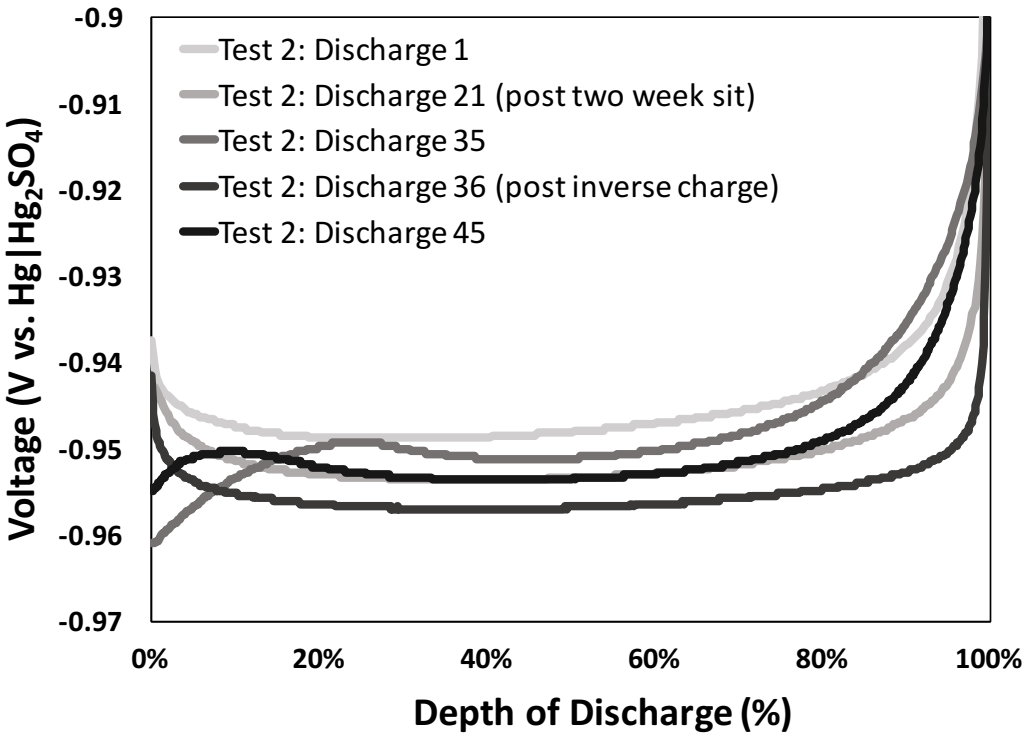


**Figure 3-8:** Voltage discharge data for Pb rod Test 2 at various stages of life pre- and post- inverse charging.

Lower overpotentials are attributed to minor improvements in electrode reversibility, perhaps due to an average decrease in $PbSO_4$ radius. The minor improvement observed in discharge 36, however, is lost in subsequent cycles (discharge 45), indicating rapid crystal coarsening per Ostwald-Fruendlich driving forces. Capacity increases (not illustrated) are maintained, and are attributable to sustained increases in electroactive surface area.

The initial discharge voltage dips and spikes are related to the abundance or depletion of $Pb^{2+}$ ions, in an effect termed "Spannungssack" or "coup de fouet". Spikes are related to the chemical process of crystallization being suppressed at the beginning of a discharge process if no sulfate crystal seeds are present already [94]. During discharge, $Pb^{2+}$ ions are produced above the equilibrium concentration, and an additional overvoltage occurs per Eqn. 3-3.

$$E_{Pb^{2+}} = \frac{RT}{nF} ln\left(\frac{C_{Pb^{2+}}}{C_S}\right) \qquad (3\text{-}3)$$

Where $c_S$ is the equilibrium concentration derived from $PbSO_4$ solubility at a specific temperature and acid concentration. As such, Spannungssack phenomena is more pronounced the better the previous charging has been. In the cycle immediately post inverse charging (discharge 36), Spannungssack phenomena is especially pronounced, indicating a substantial reduction in the number of $PbSO_4$ seed crystals through more effective recharging than previous cycling.

### 3.2.2. Effect of inverse-charge voltage and hydration

A Pb rod was cycled in an optimal fashion (1-3 h discharge rate) until capacities fell to <50% of peak to examine the effects of sulfation reversal at the end of life, with results illustrated in Figure 3-9. The rod peaked in capacity after 100 cycles at ~3300 $mC/cm^2$ before exhibiting rapid declines due to sulfation failure. Inverse charging was conducted at cycle 208 per a +1.3 V hold

as outlined in *Section 3.1.1*, resulting in exacerbated failure (Figure 3-9b). The rod was then oxidized using a +1.5 V hold, and significant capacity recovery was observed (Figure 3-9c) coupled with an exfoliation of the outer $PbSO_4$ layer illustrated in Figure 3-10. Subsequent +1.5 V inverse charges continued to increase electrode capacity until failing to do so after the 5$^{th}$ trial.

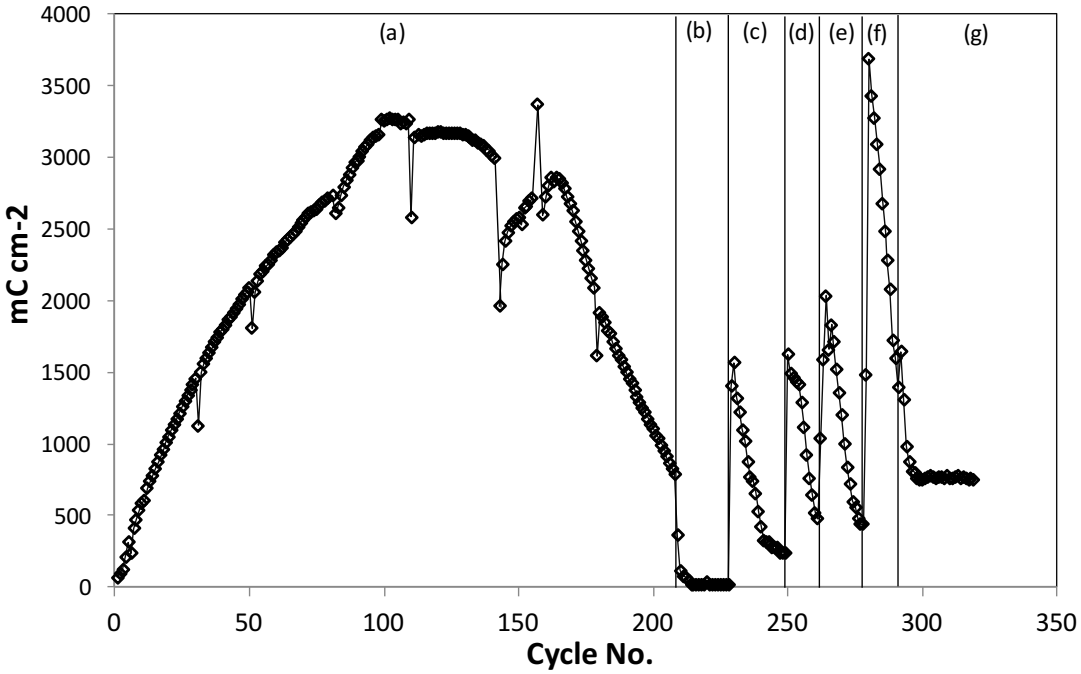


**Figure 3-9**: Long-term cycling of lead rod in 4M $H_2SO_4$ **a)** discharging at +50/-200 μA/cm$^2$ for first 20 cycles, +200/-400 μA/cm$^2$ for remainder. **b)** cycling at +200/-400 μA/cm$^2$ after inverse charging at +1.3 V. **c-f)** cycling at +200/-400 μA/cm$^2$ after inverse charging at +1.5 V. **g)** cycling at +50/-400 μA/cm$^2$ after inverse charging at +1.5 V.

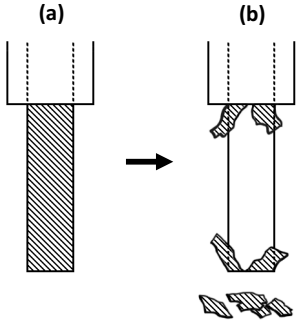


**Figure 3-10:** Peeling $PbSO_4$ film from heavily sulfated lead metal samples pre- and post-inverse charging at +1.5 V.

These results indicate that inverse charging is substantially more complete at more oxidizing voltages (+1.5V) on the negative electrode. Final SEM images of the Pb rod's active material (after cycle 319) are given in the image in Figure 3-11. Rod peeling and electrode expansion evident in Figures 3-10 – 3-11 show progressive displacement of crystalline $PbSO_4$ via hydration of pore interiors, resulting in higher prevalence of macropores at the expense of micropores after successive inverse charging.

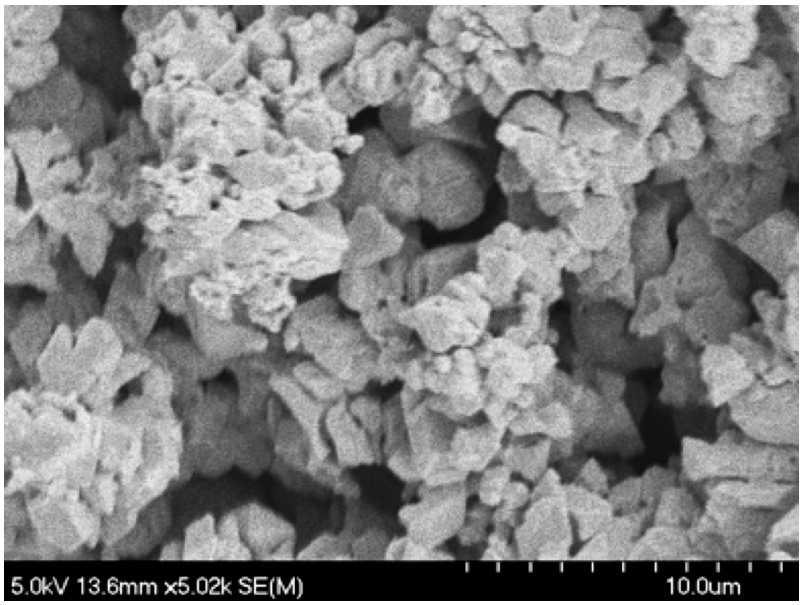


**Figure 3-11:** SEM image of active material for Pb rod after 319 cycles and 6 consecutive inverse charges.

Hydration of the electrodes is a condition whereby $PbSO_4$ solubility and dissolution increases considerably in weakly acidic pore structures, resulting in a tendency for more voluminous precipitation reactions in alkaline pH, resulting in outward electrode growth [20]. Outward electrode growth is also observable on slowly cycled Pb rods, whereby cycling at +10/-200 $\mu A/cm^2$ creates plate-like Pb structures that impede $H_2SO_4$ transport (Figure 3-12). During inverse charging, voluminous $PbSO_4$ structures are observed in Figure 3-12b, coupled with a significant decrease in rod capacity. For failed inverse charging experiments with dense $PbSO_4$

films (Tests 3 and 4) it is speculated that loss of inter-particle contact results from either volumetric expansion through hydration effects, or substantial growth of a non-conductive corrosion (a-PbO) under layer.

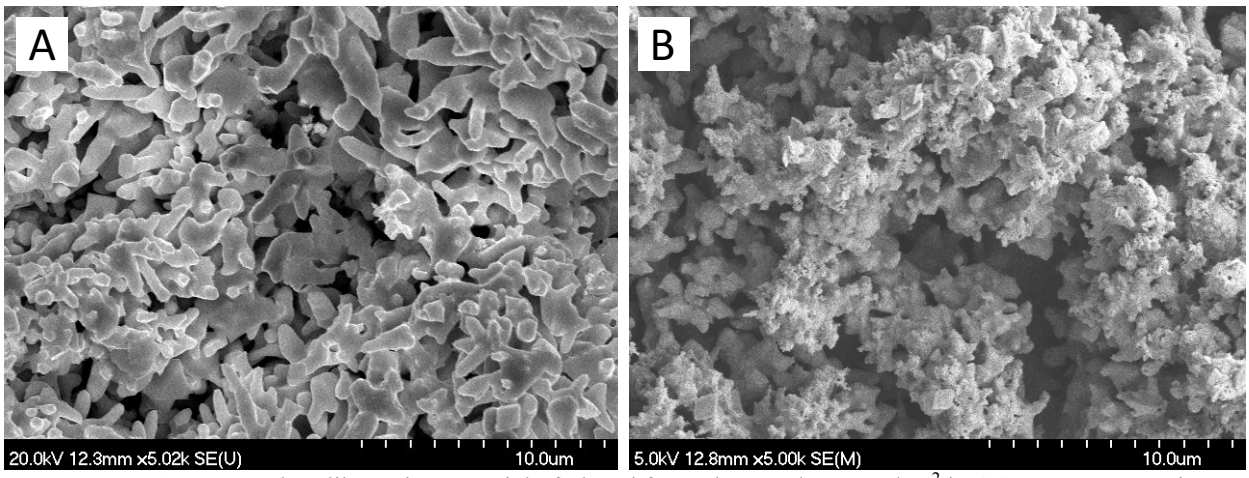


**Figure 3-12:** Compact, plate-like active material of Pb rod formed at +10/-200 μA/cm$^2$ in 4.6 M $H_2SO_4$ **A)** prior to inverse charging, **B)** post-inverse charging.

### 3.2.3. Electrochemical impedance spectroscopy results

Electrochemical impedance spectroscopy (EIS) is a useful technique to establish kinetic parameters in aqueous electrochemical systems. Zhang [48] conducted EIS tests on lead rods to illustrate the differences in electrochemical activity between $PbSO_4(O)$ (from lead oxidation) and $PbSO_4(R)$ (from lead dioxide reduction), with results displayed in Nyquist plot in Figure 3-13.

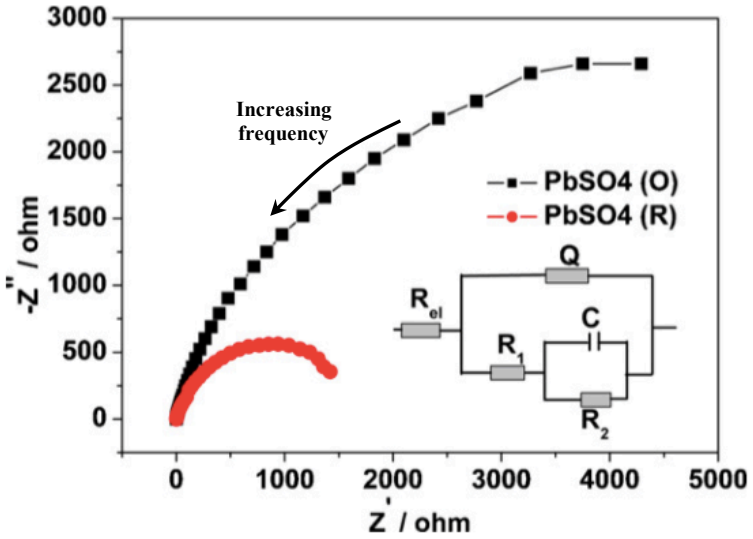


**Figure 3-13:** Nyquist plot for Pb electrode in 4 M $H_2SO_4$. Potentiostatic impedance for $PbSO_4$(O) at -0.95 V hold after reduction at -2 V. Impedance for $PbSO_4$(R) conducted at +0.96 V hold after oxidation at +2 V. Source: Ref. [48].

Impedance spectra illustrated in Figure 3-13 are typical when the kinetics of charge transfer are slower than ion diffusion in the electrolyte, resulting in a single semi-circle, with inductance on the ordinate (–*Z''*) and resistance on the abscissa (*Z'*) [95]. High frequency intercepts at zero inductance give the ohmic resistance of ionic transport through the electrolyte and electrode film, $R_\Omega$. Low frequency intercepts of extended semicircles give the sum of ohmic and charge transfer resistances, $R_\Omega + R_{CT}$, where $R_{CT}$ relates to the kinetics of reaction [95]. Zhang reports a nine-fold reduction in $R_{CT}$ for $PbSO_4(R)$ as compared to $PbSO_4(O)$.

Similar impedance investigations on Pb rods were conducted both potentiostatically and galvanostatically to determine resistivity differences of electrodes prior to and after inverse charging. Measurements were conducted using a frequency range of 0.1 Hz - 10 kHz, eight frequencies per decade. Potentiostatic impedance tests were conducted on rods after each consecutive inverse charge. Inverse charging was conducted at +50 μA/cm$^2$ CC for 40 h after polarity reversal (> +1 V) and then recharged to -1.1 V at -200 μA/cm$^2$. Rods were discharged at

+50 μA/cm$^2$ to -0.8 V, held potentiostatically for 1 h, and analyzed for impedance spectra changes (Figure 3-14). Results show that $R_{CT}$ improvements described by Zhang from inverse charging are not sustained after discharging, resulting in negligible electrode changes to $PbSO_4$ films ($R_\Omega$), and $PbSO_4$ activity ($R_{CT}$), possibly because of particle agglomeration or detachment.

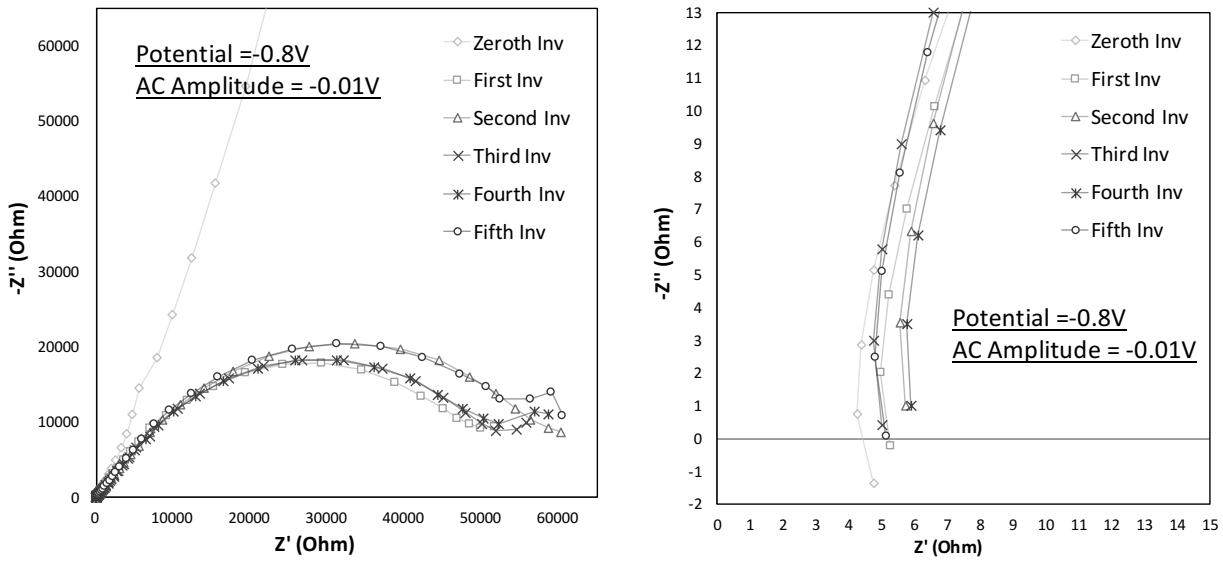


**Figure 3-14:** Potentiostatic Nyquist plot for Pb rod after consecutive inverse charging. Prior to each EIS run, rods were discharged at +50 μA/cm$^2$ to -0.8 V and held for 1 h. EIS run from 0.1Hz - 10kHz.

Similar results were exhibited for Pb rods that were subjected to pre-cycling before inverse charging. Figure 3-15 shows the results of a Pb rod cycled 17 times and inversely charged per the same protocol, with negligible differences in $R_\Omega$ and $R_{CT}$.

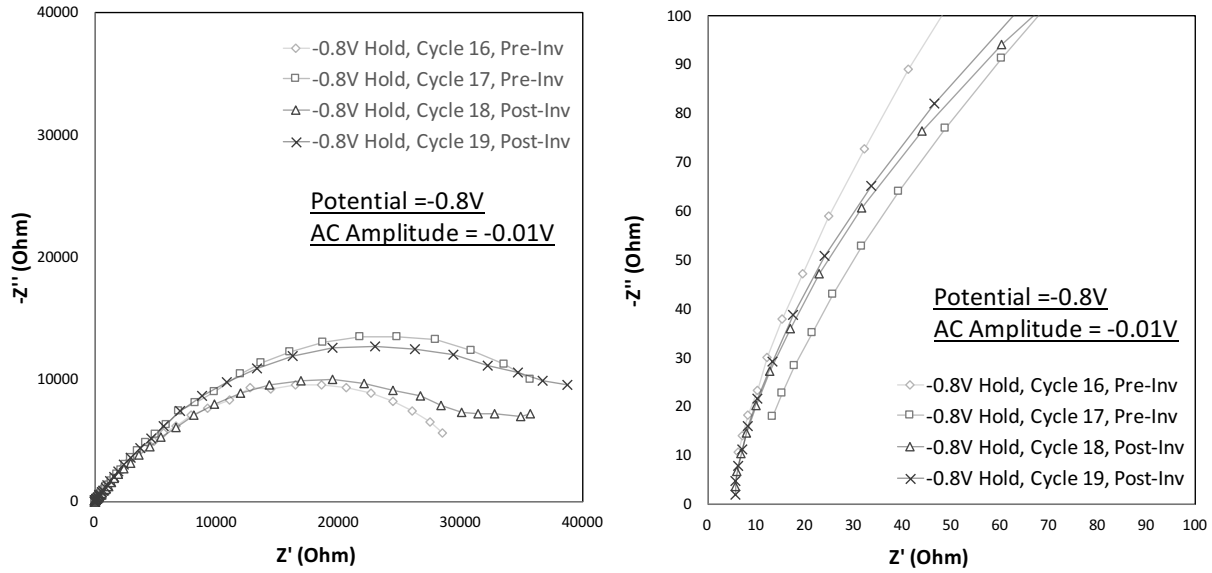


**Figure 3-15:** Potentiostatic Nyquist plot for Pb rod pre-cycled 17 times prior to inverse charging. Prior to each EIS run, rods were discharged at +50 μA/cm$^2$ to -0.8 V and held for 1 h. EIS run from 0.1 Hz - 10kHz.

Pb rods were monitored at open circuit and allowed to self-discharge over a 36 h period. Periodic galvanostatic impedance testing was conducted every 4 h, and ohmic resistance changes were observed to correlate with the thickness of $PbSO_4$ films (a function of open circuit voltage) during Pb discharge (Figure 3-16).

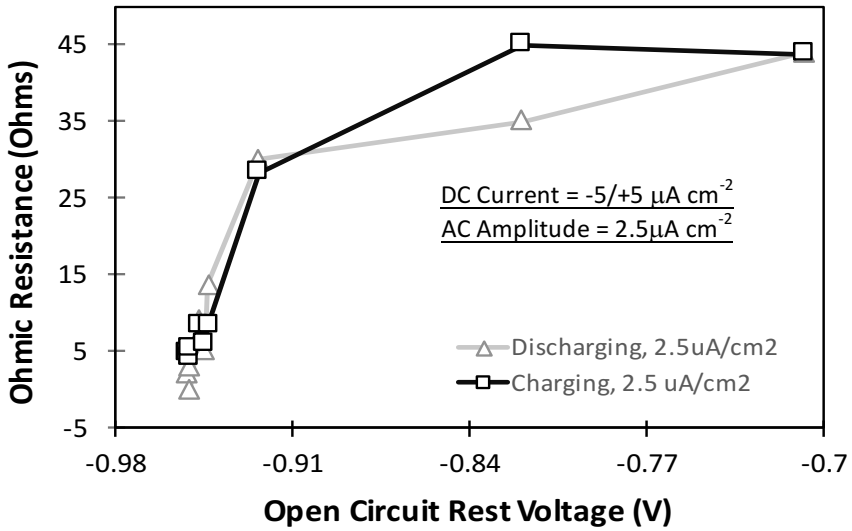


**Figure 3-16:** $R_\Omega$ measurements from galvanostatic EIS results for Pb rod held at OCV for 36 h. Galvanostatic EIS runs used an applied current of -5/+5 μA/cm$^2$ with an AC amplitude of 2.5 μA/cm$^2$. Frequency range from 0.1 Hz - 10 kHz.

Galvanostatic impedance tests were subsequently run on a Pb rod pre-cycled 12 times, inversely charged, and impedance spectra analyzed (Figure 3-17). Like potentiostatic EIS, galvanostatic testing results indicated no reduction in ohmic resistance within $PbSO_4$ from inverse charging.

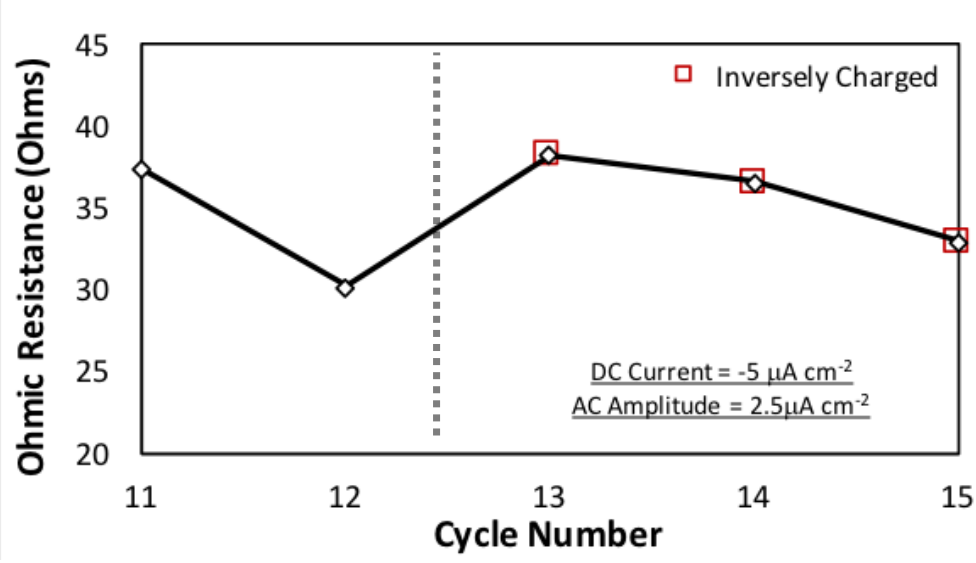


**Figure 3-17:** $R_\Omega$ measurements from galvanostatic EIS results for Pb pre-cycled 12 times prior to inverse charging. Prior to each EIS run, rods were discharged at 50 μA/cm$^2$ to -0.8 V. EIS runs used an applied current of -5 μA/cm$^2$ with an AC amplitude of 2.5 μA/cm$^2$, 0.1 Hz - 10 kHz.

## 3.3. Battery Electrode Tests

### 3.3.1. Battery tests with Pb-Ca/Pb-Ca-Sn grid alloy electrodes

Reconstructed PowerSonic Pb-Ca/Pb-Ca-Sn VRLA flooded equivalents were assembled (*Section 3.1.2*) and allowed to sit at OCV in 4 M $H_2SO_4$ for 1 month in a discharged state, to form dense $PbSO_4$ films. Powder X-ray analysis reveals $PbSO_4$ content increased from 45% to 55.3% during this period. Inverse charging was subsequently conducted for 24 h at the $C_{20}$/13.3 rate per the protocol outlined by Karami. Negative electrodes were observed to spontaneously evolve hydrogen gas (verified by gas chromatography). Monitoring of negative electrode voltages at open circuit yielded the information presented in Figure 3-18. Self-discharge of the negative

electrode is accelerated, and full capacity of the electrode is lost in a 32 h timeframe. Voltages are observed to obey a discharge plateau corresponding to the $Pb/PbSO_4$ couple under the influence of a strong oxidant (–0.96 V) until the reaction terminates. Post completion, the voltages are observed to drift to a plateau between –0.4 and –0.6 V, corresponding to a Pb/PbO electrode in neutral pH [60,96]. Consequently, after the reaction is complete, the electrode is no longer able to store charge. X-ray analysis shows $PbSO_4$ content made up 96.6% of the electrode mass, and reduction of the negative electrode to stable potentials other than this plateau were not achievable, as the electrode remains semipermeable indefinitely [15,60]. Failed inverse charging data for heavily sulfated porous electrodes are analogous to failures observed on heavily sulfated Pb rods. Like results with Pb rod Tests 3–4, the difficulty of oxidizing dense $PbSO_4$ films, coupled with impeded $H_2SO_4$ transport works to damage conductive pathways within the electrode, creating an unusable semipermeable membrane through excessive hydration. Gassing behavior is attributed to galvanic interactions with electrodeposited and dissolved species of tin introduced during inverse charging.

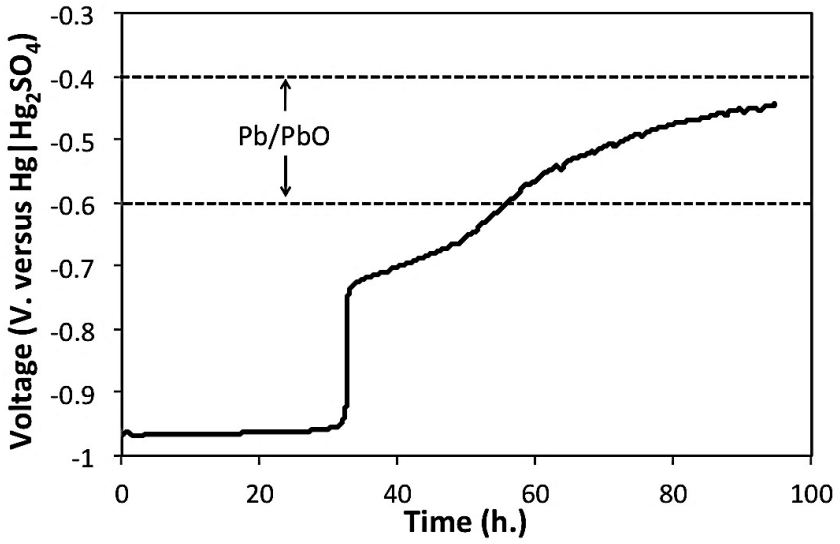


**Figure 3-18:** Observed voltage drift post-inverse charging of heavily sulfated Pb-Ca negative electrode at the $C_{20}$/13.3 rate in constructed Pb-Ca/Pb-Ca-Sn grid alloy batteries. Battery was fully charged post-inverse charging and monitored at open circuit.

Capacity versus current relationships were subsequently developed for new OEM PowerSonic VRLA batteries as well as reconstructed flooded cell equivalents with results given in Figure 3-19a. Batteries are pre-cycled 10 times, inversely charged per the protocol outlined in section 3.1.2, and then continuously cycled (Figure 3-19b). Significantly higher capacities are observed for flooded cells as compared to OEM VRLA batteries, despite the equivalence of the electrodes used. This is attributable to the use of excess sulfuric acid, allowing for greater active material utilization ($\eta_{util}$). Interestingly, all capacity-current relationships and regular cycling data for Pb-Ca/Pb-Ca-Sn batteries post-inverse charging show capacity declines ranging from 30–67%.

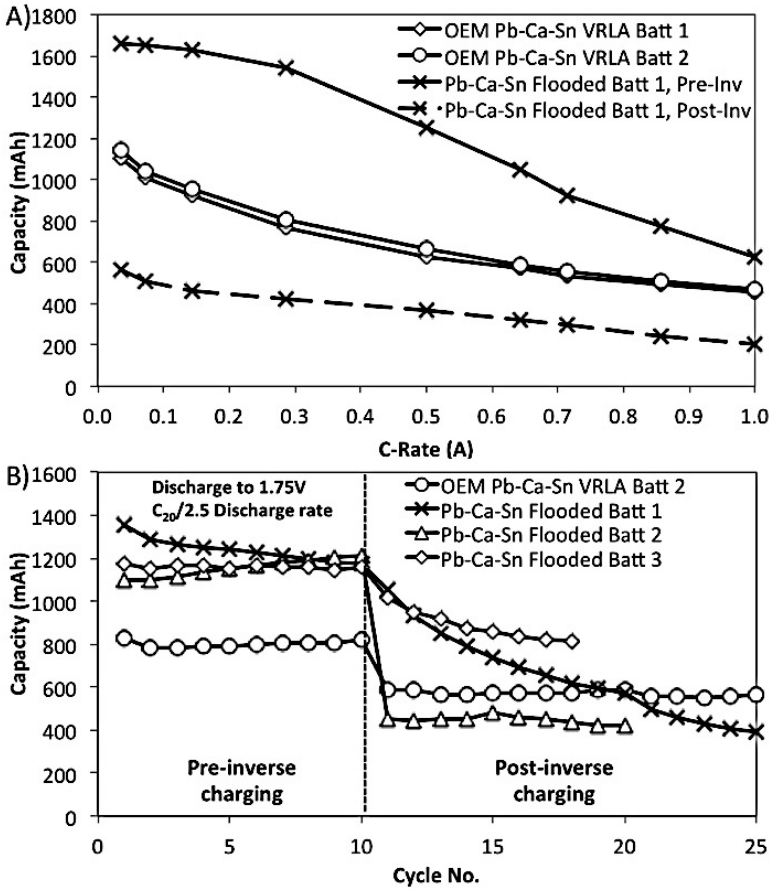


**Figure 3-19: A)** Galvanostatic discharge amp-hour capacity versus current draw for different PowerSonic™ Pb-Ca/Pb-Ca-Sn battery electrode formats. Electrodes from OEM VRLA and constructed flooded arrangements are equivalent. **B)** Discharge capacity by cycle number. Inverse charging of new batteries is conducted after cycle 10. All studies (except OEM VRLA) conducted in 4M $H_2SO_4$ electrolytes. Charging protocol: current limited CCCV charge at $0.1C_{20}$, +2.45 V cutoff held until $C_{20}/35$. Discharge protocol: CC discharge to a +1.75 V cell voltage cutoff.

When positive and negative electrode groups are tested independently after inverse charging, it is discovered that the positive electrodes are responsible for capacity declines, whereas negative electrode capacity performance is improved. In Figure 3-20b, negative electrode discharge capacity increases by 28%. In addition, the electrodes discharge at higher initial voltages of –0.96 V, an observation consistent with voltage discharge data for formed pure Pb metals post-inverse charging. Figure 3-20a shows positive Pb-Ca-Sn electrodes suffer significantly reduced discharge times.

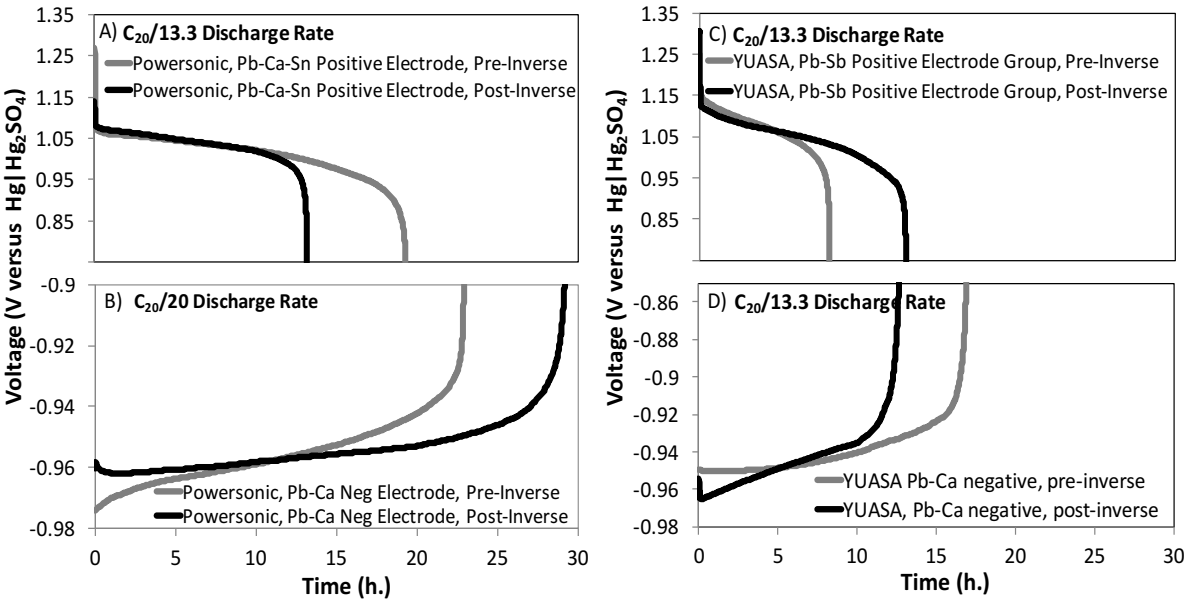


**Figure 3-20:** Galvanostatic discharge voltages for **A)** Porous Pb-Ca-Sn positive electrode pre- and post-inverse charging (4 M $H_2SO_4$). **B)** Porous PowerSonic Pb-Ca negative electrodes pre- and post-inverse charging (4 M $H_2SO_4$). **C)** Porous Pb-Sb positive electrodes pre- and post-inverse charging (4.64 M $H_2SO_4$). **D)** Porous Yuasa Pb-Ca positive electrodes pre- and post-inverse charging (4.64 M $H_2SO_4$).
Negative electrode charging protocol: CCCV charge at $0.1C_{20}$ to -1.1 V hold.
Positive electrode charging protocol: CCCV charge at $0.1C_{20}$ to +1.3 V hold.

**Table 3-1:** Discharge capacity, specific capacity and estimated electrode active material utilization for battery electrodes in Figure 3-20, pre-and post- inverse charging.

| | | Pre-inverse | | | Post-inverse | | |
|---|---|---|---|---|---|---|---|
| *Battery* | *Electrode* | *Capacity (mAh)* | *σ (mAh/g)* | *$\eta_{util}$ (%)* | *Capacity (mAh)* | *σ (mAh/g)* | *$\eta_{util}$ (%)* |
| **YUASA** | Positives, Pb-Sb | 1234 | 85.0 | 37 | 1959 | 135.0 | 60 |
| | Negatives, Pb-Ca | 2538 | 135.3 | 53 | 1901 | 101.4 | 38 |
| **PowerSonic** | Positives, Pb-Ca-Sn | 2031 | 105.1 | 47 | 1387 | 71.7 | 32 |
| | Negatives, Pb-Ca | 1602 | 121.9 | 46 | 2043 | 155.5 | 60 |

### 3.3.2. Battery tests with Pb-Ca/Pb-Sb grid alloy electrodes

New Yuasa Pb-Ca/Pb-Sb grid alloy batteries were similarly cycled and inversely charged. Capacity versus current relationships were developed using the same current rate and voltage cutoffs as for Pb-Ca/Pb-Ca-Sn batteries, with results presented in Figure 3-21a. Batteries tested at the $C_{20}$/20 rate had discharge capacities that were lower than nominal (2 Ah). Battery 2 was observed to have significant trouble in handling moderate to high currents. Subsequently, this Pb-Ca/Pb-Sb battery was cycled 10 times and inversely charged. The capacity versus current data was subsequently tested, and the performance of this battery was seen to be significantly enhanced for all currents. Post inverse charging, battery 2 performed significantly better than brand new overcharged Yuasa batteries. Figure 3-21b contains the complete dataset, as compared with the results of the Pb-Ca/Pb-Ca-Sn batteries. Inverse charging for Pb-Sb flooded batteries is seen to be beneficial overall, with positive electrode capacity improvements illustrated in Figure 3-20c. For Pb-Ca/Pb-Sb couples, negative electrode capacities were diminished by 25% post-inverse charging, figure 3-20d.

Grid alloys effects are directly responsible for observed capacity declines in Pb-Ca-Sn batteries. Positive electrode grids without conductive alloys of tin or antimony suffer from premature capacity loss (PCL effect) (*Section 1.4.4*) [31,40,97]. 1.2 wt. % additions of tin (Sn) ensure connectivity at the grid/active material interface, present as tin dioxide ($SnO_2$), a conductive and relatively stable compound. Inverse charging of Pb-Ca-Sn electrodes converts $SnO_2$ to Sn during cell reversal, and spikes in $SnSO_4$ concentration are observed in Table 3-2 [98].

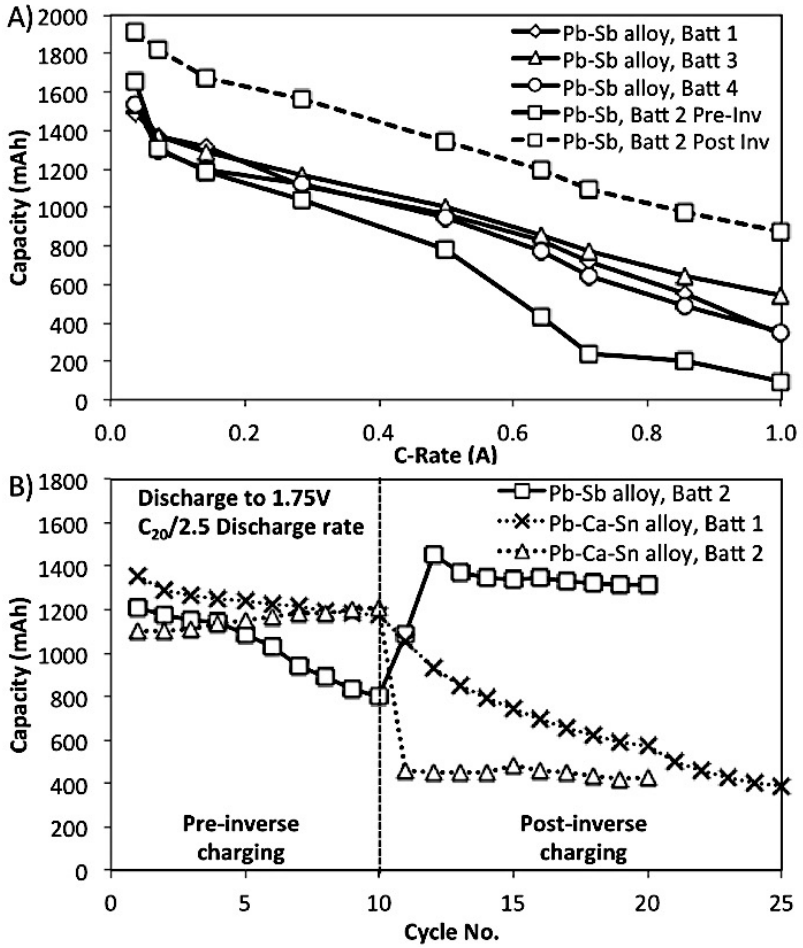


**Figure 3-21: A)** Galvanostatic discharge amp-hour capacity versus current for new flooded Yuasa™ Pb-Ca/Pb-Sb batteries. **B)** Discharge capacity by cycle number for Yuasa batteries (Pb-Sb grid alloy) as compared to Pb-Ca-Sn grid alloy batteries. Inverse charging of new flooded batteries was conducted after cycle 10. All Yuasa Pb-Sb batteries use 4.64 M $H_2SO_4$ electrolyte.
Charging protocol: current limited CCCV charge at $0.1C_{20}$, +2.45 V cutoff held until $C_{20}/35$.
Discharge protocol: CC discharge to a +1.75 V cell voltage cutoff.

**Table 3-2:** GFAAS analysis of dissolved metal concentrations at different stages of inverse-charging. Wavelength of analysis for tin, 286.3 nm; wavelength of analysis for antimony, 217.6 nm.

| *Samples* | *Fully charged* | *Discharged to 1.75V* | *Reversed polarity* | *Recharged, post-inverse* | *Total mL* |
|---|---|---|---|---|---|
| | **Tin concentration (ppm)** | | | | |
| New Pb-Sn-Ca/Pb-Ca Couple | 2.2 | 4.3 | 10.3 | 8.1 | 70.0 |
| New Pb-Sn-Ca/Pb-Ca Couple | 3.4 | 5.8 | 10.0 | 8.0 | 70.0 |
| | **Antimony concentration (ppm)** | | | | |
| New Pb-Sb/Pb-Ca Couple | <1 | <1 | 1.4 | 4.5 | 35 |

Tin metal is highly soluble in sulfuric acid electrolytes, forming aqueous tin sulfate ($E_{Sn/Sn^{2+}}$= –0.09 V vs. STP $H_2$ electrode) [27,99]. Loss of tin likely explains observed positive electrode capacity declines while likely improving the efficacy of the process on the anode. Karami [46] conducted inverse charging on traditional flooded PbA batteries, typically constructed with Pb-Sb grid alloys, possibly explaining capacity retention in studied batteries. Antimony concentrations are observed to increase to a lesser degree after inverse charging, due to antimony metal's nobility with respect to hydrogen ($E_{Sb/Sb_2O_3}$ = +0.15 V vs. STP $H_2$ electrode) [27,99]. Additionally, anodic dissolution of alloyed antimony in Pb-Sb has been found to incorporate into the PAM in the form of hydrated antimony oxides, cementing $PbO_2$ particles and ensuring conductivity at the grid/PAM interface [39].

### 3.3.3. Effect of curing and $SnSO_4$ additives in negative electrode inverse charging

Figure 3-20b illustrates that dissolved quantities of tin (~0.015 mol SnSO4/L in 70 mL setups) may have worked to enhance inter-particle connectivity during the inverse charging of PowerSonic Pb-Ca negative electrodes as compared to YUASA Pb-Ca electrodes (Figure 3-20d). Additionally, the influence of particle size on positive PbA battery electrode formation has been adequately described in the literature. $PbO_2$ active material consists of gel/crystal zones that grow to substitute large $PbSO_4$ via metasomatic endotaxy, Figure 3-22a [15,44]. Oxidation of small crystallites proceeds through a displacement dissolution process that migrates active material from the host, forming small ringlets of $PbO_2$ active material, Figure 3-22b [100]. Particles less than 10 μm × 4 μm are fully oxidized and do not leave behind a conductive skeleton. Particles 15-20 μm × 8-10 μm are superficially oxidized metasomatically [101–103].

To test the influence of $SnSO_4$ and particle size, inverse charging of new PowerSonic and Yuasa Pb-Ca negative battery electrodes was conducted in isolation using an H-cell setup. Surface area, x-ray and SEM measurements were taken prior to and after the technique. PowerSonic Pb-Ca negatives were composed of significantly larger active material crystals (Figure 3-23a), compared to Yuasa negative electrodes (Figure 3-23b). The results after the protocol indicate that inverse charging of these small feature sizes completely alters (and destroys) structural connections and conductive pathways, resulting in observed capacity declines (Figure 3-23a', 3-23b').

New PowerSonic Pb-Ca negatives were enclosed in polyethylene and placed into a furnace at 80 °C for 24 h to cure and coarsen electrode particles. During plate manufacture, curing creates 4BS from 3BS at 80°C when allowed to react with dilute acid [23]. X-ray phase analysis of cured samples showed that the sulfation process was accelerated as opposed to 4BS formation, due to highly concentrated >4.6 M (1.265 specific gravity) pore acid concentration (Appendix B). However, SEM images of cured electrode samples at 6 h increments indicate particle fusion and growth (Figure 3-24). Inverse charging of the cured battery electrode (Figure 2-24f) indicates slightly more compact particulate morphology and structure retention post-inverse charging as compared to new uncured electrodes.

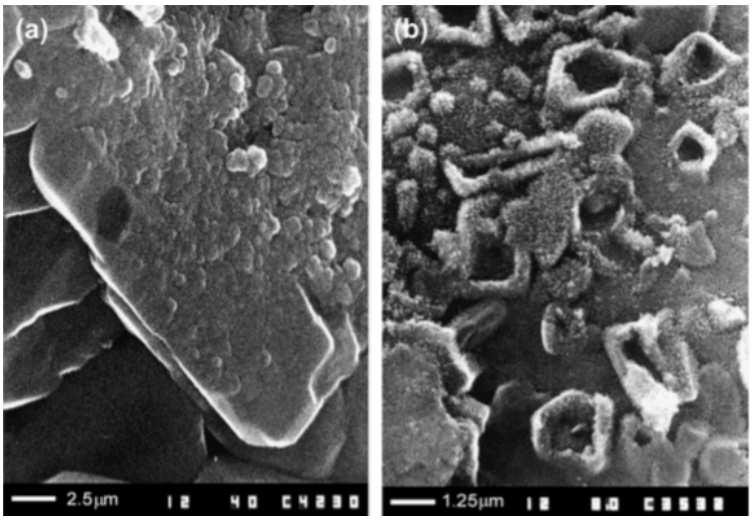


**Figure 3-22: (a)** Oxidation of large $PbSO_4$ maintains structure. **(b)** Oxidation of small $PbSO_4$ proceeds with displaced dissolution. Source: Ref. [100]

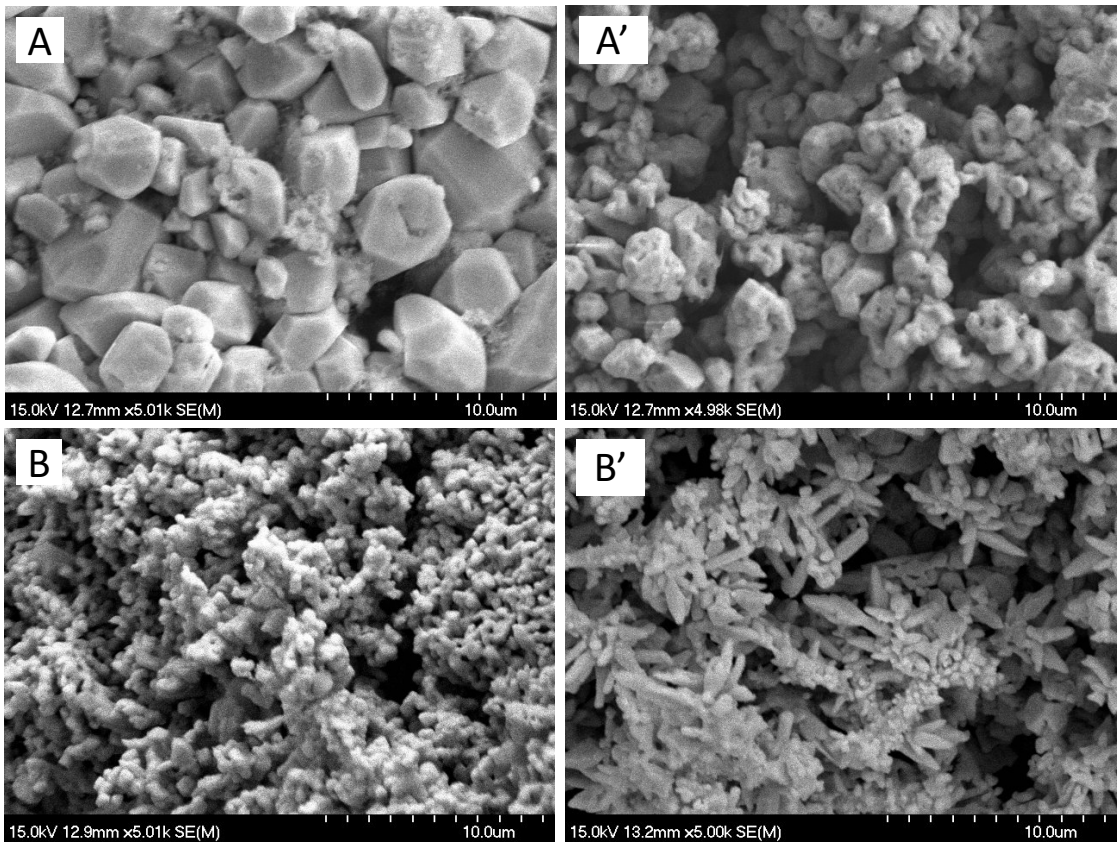


**Figure 3-23:** SEM images of Pb-Ca negative electrodes pre- and post- inverse charging for **A-A')** PowerSonic **B-B')** Yuasa.

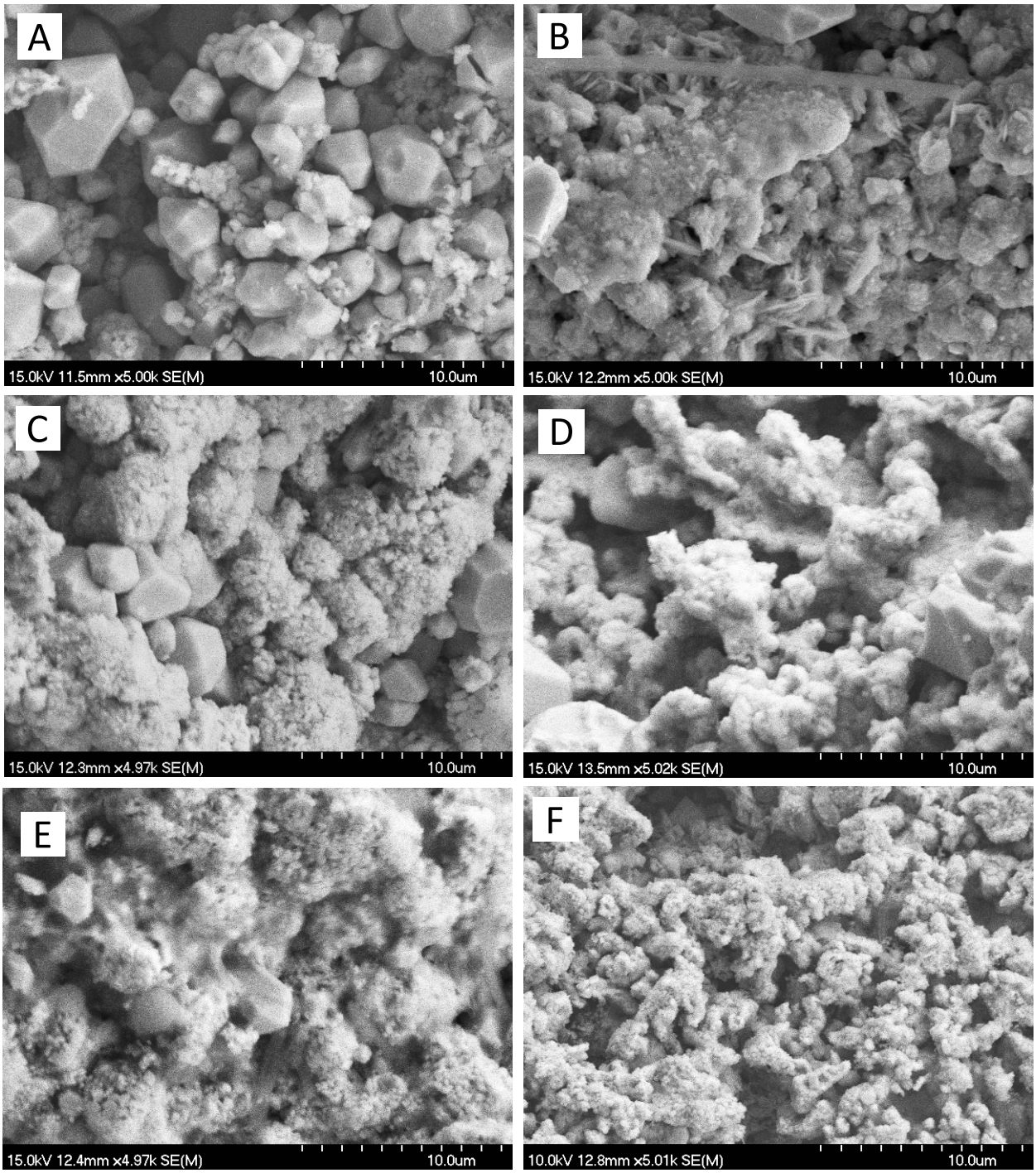


**Figure 3-24: A)-E)** SEM images of PowerSonic Pb-Ca negative electrode during curing at 80°C for 24h. Images are taken every 6 h. **F)** Cured electrode post-inverse charging.

The effect of $SnSO_4$ was investigated using individual YUASA Pb-Ca electrodes (Figure 3-25) and PowerSonic Pb-Ca electrodes (Figure 3-26). 60 mg of $SnSO_4$ was dissolved in the electrolytes for PowerSonic Pb-Ca electrodes, and 140 mg $SnSO_4$ added to YUASA Pb-Ca electrolytes (~85 mg/Ah for both). Electrodes were cycled 5 times, inversely charged at the $C_{20}$/13.3 rate, and then cycled another 10 times. The results show no effect for YUASA negatives, but demonstrate consistent improvements in mitigating post-inverse charging capacity losses in PowerSonic Pb-Ca electrodes. The combined effects of curing were also examined using PowerSonic Pb-Ca electrodes, indicating additional benefits were obtained through this measure. The observed anomalous jump in capacity for cycle 12 is attributable to the inconsistent local improvements afforded by $SnSO_4$ in improving inter-particle contact and conductivity.

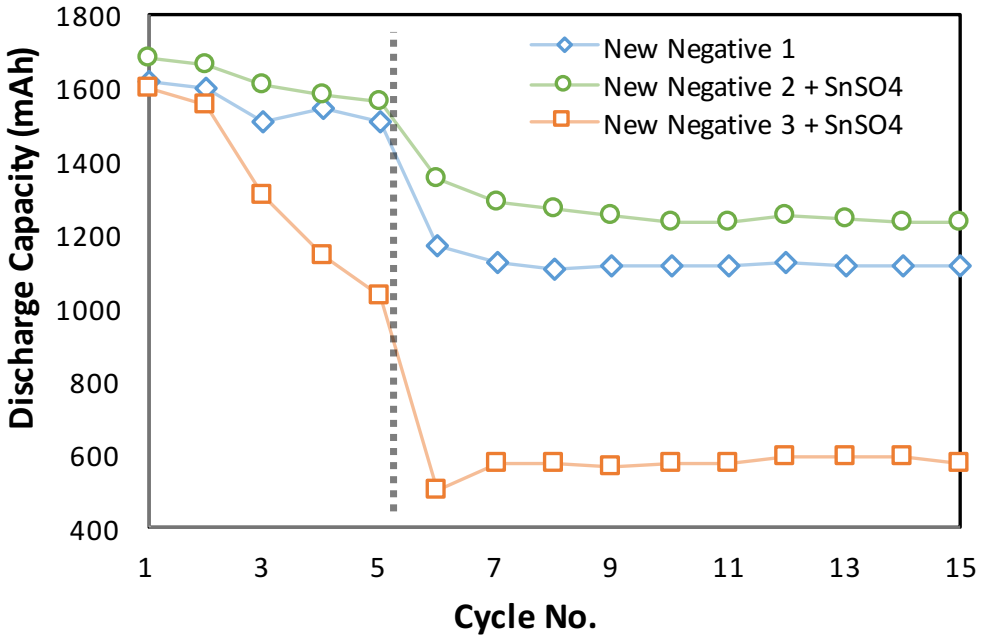


**Figure 3-25:** Effect of $SnSO_4$ additions to Yuasa Pb-Ca electrodes pre-and post- inverse charging. Electrodes charging protocol: current limited CCCV charge at 0.1$C_{20}$, -1.1V cutoff held until $C_{20}$/35. Discharge protocol: CC discharge to a -0.8 V. Inverse charging conducted using constant current at 20/13.3 rate.

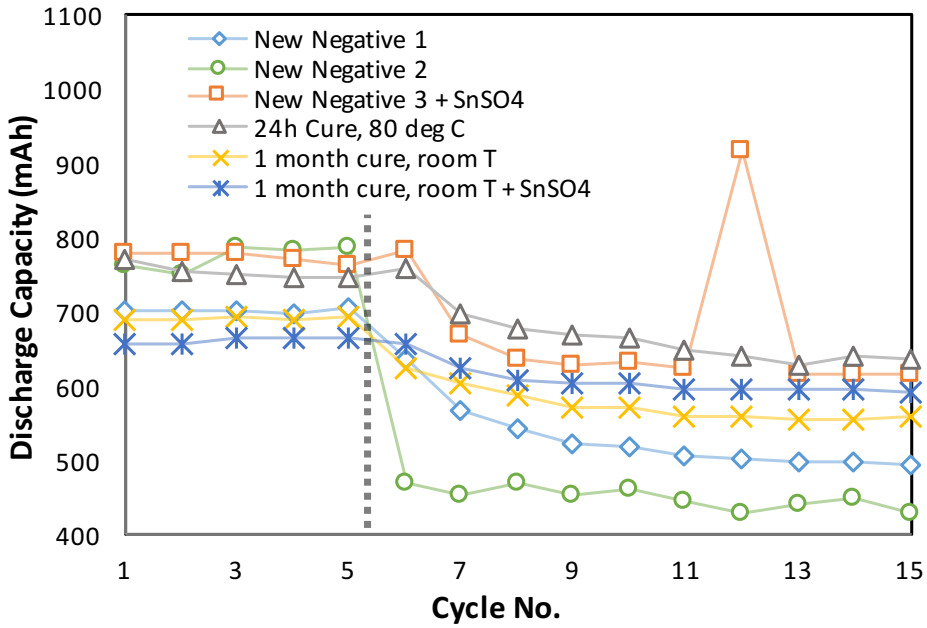


**Figure 3-26:** Effect of $SnSO_4$ additions and electrode curing on PowerSonic Pb-Ca electrodes pre- and post- inverse charging. Electrodes charging protocol: current limited CCCV charge at $0.1C_{20}$, -1.1 V cutoff held until $C_{20}/35$. Discharge protocol: CC discharge to a -0.8 V cutoff. Inverse charging conducted using constant current at $C_{20}/13.3$ rate.

Yuasa and PowerSonic BET and phase analysis of x-ray data for samples before and after inverse charging are presented in Table 3-3, with the full data available in Appendix B. BET and x-ray data indicate similar findings to capacity data. Both Yuasa and PowerSonic electrodes suffer surface area declines post-inverse charging because of small particle dissolution, fusion, and macropore generation (electrode growth) [104]. Inverse charging of PowerSonic Pb-Ca electrodes is seen to dramatically increase the content of Pb at the expense of $PbSO_4$. This finding substantiates the reported desulfation property of inverse charging exhibited on pure lead metals, when successful. On the contrary, pathway destruction during inverse charging of Yuasa Pb-Ca electrodes is seen to form irreducible $PbSO_4$ at the expense of Pb and PbO, due to the loss of interparticle contact (with few exceptions).

**Table 3-3:** Electrode BET and x-ray phase analysis results for Yuasa and PowerSonic Pb-Ca electrodes pre- and post-inverse charging, examining the effects of $SnSO_4$ additions and curing.

| YUASA Pb-Ca Electrodes | | | | | | |
|---|---|---|---|---|---|---|
| | **BET Area** | **XRD Phase Composition** (%) | | | | |
| | *($m^2/g$)* | *Pb* | *PbO* | *$PbSO_4$* | *3BS* | *Other* |
| New Negative 1 | 0.85 | 54.2 | 26.9 | 0.4 | 3.7 | 14.7 |
| New 1, post-inverse | 0.36 | 61.1 | 17.4 | 6.4 | 14.8 | 0.3 |
| New 2 + $SnSO_4$ (post-inv) | 0.60 | 48.5 | 0.0 | 46.7 | 2.5 | 2.2 |
| New 3 +$SnSO_4$ (post-inv) | 0.90 | 23.0 | 1.4 | 69.1 | 0.8 | 5.8 |

| PowerSonic Pb-Ca Electrodes | | | | | | |
|---|---|---|---|---|---|---|
| | **BET Area** | **XRD Phase Composition** (%) | | | | |
| | *($m^2/g$)* | *Pb* | *PbO* | *$PbSO_4$* | *3BS* | *Other* |
| New Negative 1 | 1.38 | 35.2 | 1.8 | 45.5 | 17.2 | 0.2 |
| New 1, post-inverse | 0.93 | 85.6 | 4.8 | 3.4 | 0.2 | 6.0 |
| New 2, post-inverse | - | 38.1 | 5.1 | 54.3 | 1.8 | 0.8 |
| New 3 + $SnSO_4$ (post-inv) | 0.41 | 88.7 | 1.0 | 5.9 | 4.1 | 0.3 |
| 24h cure, post-inverse | 0.77 | 59.2 | 9.9 | 12.8 | 14.5 | 3.7 |

### 3.3.4. Impact of peak oxidation voltage

The total sample of results from inverse charging carried out on PowerSonic Pb-Ca negative electrodes (both constant current and constant voltage protocols) is presented Figure 3-27. From this figure a correlation is observed between peak oxidation voltage experienced by the negative electrode during inverse charging and the subsequent capacity declines. Strongly oxidizing voltages are known to exhibit substantial corrosive attack (Figure 1-3). It is speculated that strong oxidizing voltages work to thin structural connections by increasing the penetration depth of the energetic structure.

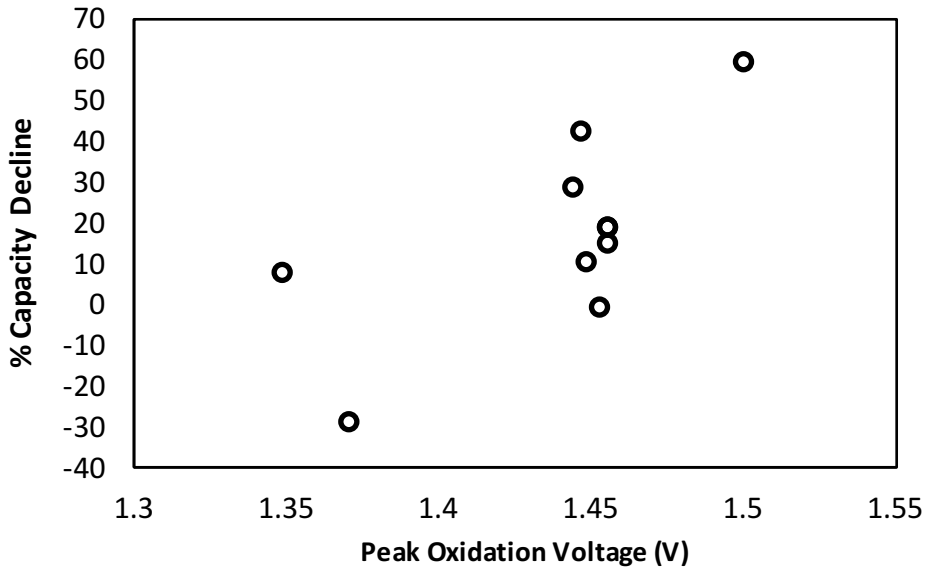


**Figure 3-27**: Impact of peak oxidation voltage during inverse charging on the capacity decline of PowerSonic Pb-Ca negative electrodes.

## 3.4. Conclusion

The investigations of Zhang [48], Karami [46], and the present study indicate battery capacity recovery and sulfation reversal post-inverse charging is possible. Table 3-1 illustrates that, when successful, inverse charging increases the specific capacity and active material utilization of studied battery electrodes significantly. Successful inverse charging of battery electrodes and pure Pb rods show improvements in discharge capacities over a range of discharge rates and no discernable negative impact to coulombic and energy efficiency values. The extent of success, however, depends on several important variables. Examination of inverse charging on Pb rods and porous battery electrodes illustrates the importance of the degree of electrode sulfation and transport of $H_2SO_4$, composition of electrode grid alloys, peak oxidizing voltage applied on the negative electrode, initial particle sizes and electrolyte additives.

Pb rod tests illustrate that capacity improvement is heavily dependent on the degree of initial sulfation and electrolyte transport in the interior pore structures of the electrode. Oxidation

of lightly sulfated Pb was easily converted to $PbO_2$ (Figure 3-5, Test 1), whereas dense layers of large $PbSO_4$ crystals (Figure 3-5, Tests 3–4) presented a significant challenge. For heavily sulfated batteries, $PbO_2$ growth on $PbSO_4$ is superficial during inverse charging, and impeded electrolyte transport results in excessive internal pore pH increases, creating semipermeable membranes through an electrode hydration mechanism or corrosion layer growth, resulting in dramatic inverse charging failure (Figures 3-9b, 3-18).

Until now, little had been investigated on how inverse charging modifies inter-particle connectivity or how it may lead to other failure routes. PbA battery active materials are tightly controlled throughout battery manufacturing to ensure electrodes have an optimal balance of structural integrity, capacity, and low internal resistance [15]. Aggressive electrode oxidation was seen to be beneficial for Pb rods (Figure 3-9), and destructive for porous Pb-Ca negatives. Constant voltage inverse charging of PowerSonic Pb-Ca/Pb-Ca-Sn batteries using the 24 h protocol outlined in *Section 3.1.2* resulted in capacity improvements for Pb-Ca negatives (Figure 3-20b). On the other hand, the constant current methods of *Section 3.1.2* on individual electrodes in H-cell setups resulted in capacity declines due to higher overall peak voltages experienced (Figure 3-26). Despite the equivalence of electrodes, higher peak voltages in constant current protocols resulted in greater oxidative penetration depths and enhanced reaction of the structural component of active mass, $G_s$, resulting in a subsequent loss of connectivity and capacity. This indicates a possible optimum voltage cutoff may be necessary to prevent conductive pathway destruction in traditionally prepared Pb-Ca negatives.

The impact of particle size on the degree of oxidation to $PbO_2$ has been studied by Pavlov on the formation of PbA battery electrodes from tetrabasic sulfates ($4PbO•PbSO_4$) whose large crystals (>20 μm) require 10–20 cycles before full capacity is reached [105]. Inverse

charging of well-cured battery electrodes with large particles is seen to retain the structure of the anode upon completion due to partial oxidation of exposed crystals (Figures 3-23 and 3-24). Porous Pb-Ca grid electrodes can experience better capacity retention when conducted on larger particle feature sizes (well cured), while suffering greater capacity declines and excessive electrode growth when conducted on small particle features. Additionally, the influence of dissolved $SnSO_4$ was seen to slightly improve inter-particle connectivity and improving the efficacy of the process. These results highlight the importance of investigating the role of electrolyte additives, and electrode particle structure.

The type of positive electrode alloy is observed to impact the efficacy of the process. Pb-Ca-Sn electrodes experience degradation during inverse charging due to Sn dissolution, while Pb-Sb electrodes appear to benefit due to Sb hydrate integration into PAM. This has important implications for conducting inverse charging in VRLA batteries with predominantly tin-based positives. No significant volumetric changes were observed for positive electrodes.

Zhang [48] describes Pb electrodes post-inverse charging as having increased surface area. Similarly, our studies on Pb indicate that surface area increases dramatically (Figure 3-7b), coinciding with increases in discharge capacity. Surface area and volumetric growth are coupled with a decrease in average lead sulfate crystal size. However, impedance and voltage data hint that post-inverse charging, agglomeration of finely divided Pb and $PbSO_4$ particles occurs. Pure metals are known to undergo a contact fusion at a temperature well below their melting point. As such, the influence of expander materials and nucleation additives should be investigated to better control the nucleation and growth of structures during inverse charging in porous electrodes. Of interest are recent advancements on the introduction of electroactive carbons (graphenes, nanotubes and carbon black to serve as nucleation sites). Additionally, the

introduction of a supporting electrolytes (e.g. $Na_2SO_4$) should be investigated to prevent electrode hydration and ensure that the ionic strength of the electrolyte never reaches that of pure water [20].

# 4. Effects of inverse charging on cycle life and battery failure modes

No research to date has been conducted on understanding the influence of inverse charging on long-term battery performance, as well as on understanding structural and compositional transformations to positive and negative electrodes as compared to regular cycling. *Chapter 3* investigated the impacts of inverse charging on the discharge capacity and electrode structure of new electrodes. This chapter investigates the influence of inverse-charging on ultimate cycle-life and battery failure modes, to inform future PbA design and to better leverage potential benefits.

## 4.1. Experimental Setup

Inverse charging can irreversibly damage electrodes, causing the dramatic capacity declines illustrated in *Chapter 3*. Pb-Ca-Sn positives (the predominant alloy for VRLA batteries) are susceptible to premature capacity losses post-inverse charging due to tin dissolution during cell reversal. Pb-Sb positives were seen to yield capacity increases, hence Yuasa Pb-Sb/Pb-Ca batteries are studied further for cycling behavior and for understanding impacts of battery inverse charging on ultimate failure. An investigation on inverse charging of failed PowerSonic VRLA Pb-Ca negative electrodes is also conducted.

Sulfuric acid was prepared by diluting to 4.64 M (1.265 specific gravity $H_2SO_4$) with de-ionized water. 7 conventional Yuasa (model no. 6N2-6A) 6 V, 2 Ah flooded motorcycle starter batteries were topped with 35 mL of acid per cell, creating an excess acid environment (1 L = ~131 Ah). Each Yuasa battery is composed of 3 cells, two ~1.6 Ah Pb-Ca negative electrodes and one ~1.3 (confirm not 1.2) Ah Pb-Sb positive, capacities individually determined at the $C_{20}$/13.3 rate. All measurements are with respect to a 4.64 M Hg|$Hg_2SO_4$ reference electrode

(+0.61 V versus S.T.P. $H^+/H_2$). One PowerSonic (model no. 612) 6 V, 1.4 Ah VRLA battery was also studied for long-term cycling, and inverse charging was conducted on failed Pb-Ca electrodes. Four distinct experiments were conducted: 1) periodic inverse charging of Yuasa batteries, 2) Yuasa battery post-mortem analysis, 3) Extended overcharging tests on failed Yuasa batteries, and 4) Inverse charging of failed PowerSonic Pb-Ca electrodes.

### 4.1.1. Cycling and periodic inverse charging of Yuasa Pb-Ca/Pb-Sb batteries

Battery cycling and capacity testing was undertaken on a Neware BTS 4000 10 V, 6 A designated battery cycler for 5 YUASA batteries until failure (discharge capacity <15% of initial values) per the following protocol: 1) charge at $C_{20}/10$ until +2.45 volts-per-cell (vpc), 2) hold at +2.45 vpc until $C_{20}/35$ current cutoff, 3) discharge at $C_{20}/2.5$ until +1.75 vpc cutoff. Periodic overcharging was conducted on Yuasa batteries every 20 cycles per the following protocol to ensure electrode state of charge was not responsible for capacity deviations: 1) charge at $C_{20}/10$ until +2.5 vpc, 2) CV hold at +2.5 vpc for 3h, 3) OCV hold for 1 h. Inverse charging was employed as a recovery strategy per the 4-step protocol for battery cells outlined in *Section 3.1.2* using an Ivium-n-Stat 10 V/10 A potentiostat, and cycling recommenced afterward.

### 4.1.2. Post-inverse charging characterization studies and post-mortem analysis

All inversely charged Yuasa batteries were dissected and a full post-mortem examination was undertaken to investigate the modes of ultimate failure. Measurements of active material shedding, x-ray phase analysis, and BET surface areas pre- and post-inverse charging were determined. Shedding was analyzed by electrode weight change studies. Positive and negative electrodes were rinsed in 3 washes of de-ionized water and then dehydrated in multiple acetone

baths, and allowed to air dry prior to plate weighing. Elevated temperature drying techniques were not conducted to avoid altering chemical composition.

### 4.1.3. Overcharging investigations on failed Yuasa Pb-Ca/Pb-Sb batteries

2 Yuasa batteries were cycled to failure per the same protocol in 4.1.1. The failed batteries were then subjected to an extensive overcharge to examine capacity recoverable, using the following protocol: 1) charge at $C_{20}/10$ until +2.5 vpc, 2) CV hold at +2.5 vpc for 5 days.

### 4.1.4. Inverse charging of failed PowerSonic Pb-Ca negative electrodes

A PowerSonic 6V 1.4Ah VRLA battery was cycled until approximately 50% of initial discharge capacity, using the cycling protocol in *Section 4.1.1*. The PowerSonic VRLA battery was not regularly overcharged. Post-failure, PowerSonic VRLA battery electrodes were extracted and absorbed glass mat microfiber separators were removed and discarded. The effect of inverse charging on individual negative electrodes was evaluated using a standard three-electrode H-cell (Figure 3-1). Individual negative electrode plates were sandwiched between Daramic porous polyethylene separators and Teflon compression endplates, and immersed in beakers of 70 mL pre-sparged (argon gas) 4.64 M $H_2SO_4$, constituting an excess electrolyte environment. Inverse charging was conducted using the following inverse charge protocol: 1) CC discharge at the $C_{20}/13.3$ rate until fully discharged (–0.8 V), 2) continued CC discharge for an additional 40 hours, 3) recharge at the $C_{20}/13.3$ rate to -1.1 V, 4) -1.1 V hold until $C_{20}/35$ (like figure 3-2).

## 4.2. Results and discussion

### 4.2.1. The effects of periodic inverse charging on cycle life and roundtrip efficiency

4 YUASA batteries were cycled per the scheme outlined in *Section 4.1.1*. Each battery contained significant performance differences due to manufacturing variability. Batteries were inversely charged when capacities fell to less than 15% of initial discharge capacity (except for Battery 2 which was also inverse charged after 10 initial cycles). The results of the long-term testing are displayed in Figures 4-1(a-d). Small jumps in discharge capacity every 20 cycles are a result of periodic overcharging. For every cycle, roundtrip efficiency (RTE) values were calculated per Eqn. 4-1, using numerical integration with a 1 min data resolution:

$$Roundtrip\ Efficiency = \eta_{RTE} = \frac{\int_{T_{0,D}}^{T_{f,D}} I_D V_D dt}{\int_{T_{0,C}}^{T_{f,C}} I_C V_C dt} \qquad (4\text{-}1)$$

Where, $T_{0,D}$, $T_{f,D}$ = times of initial and final discharge at 1.75 vpc
$T_{0,C}$, $T_{f,C}$ = times of initial and final charge
$I_C$, $I_D$ = charge and discharge currents
$V_C$, $V_D$ = battery voltage during charge and discharge

Batteries 1-4 experience nearly complete recovery of discharge capacity post inverse-charging. This is attributable to capacity increases in the positive electrode, coupled with capacity declines in the negative. Capacity decreases of the negative electrode were within ranges to maintain the batteries as a cathode limited design, as was demonstrated in Table 3-1. Battery 1 (Figure 4-1a) performed the most reliably, having the slowest decline in discharge capacity per cycle, whereas Battery 3 experienced the most variability both before and after inverse charging. Batteries 2 and 4 exhibited similar performance, including steep initial capacity declines, and a steep resurgence in capacity values post-inverse charging. All batteries experienced a dramatic drop in RTE

values for the remainder of battery testing either immediately after final inverse charging (Batteries 1, 2, 3) or during regular cycling (Battery 4). This failure phenomenon is examined more fully in post-mortem investigations.

### 4.2.2. Battery post-mortem

The dramatic reductions in RTE illustrated in Figure 4-1 were stable, and occurred after the cumulative quantity of charge passed through each battery (amp-hour throughput) given in table 4-1. Temporary RTE drops were also observed immediately after inverse charging for all batteries studied.

**Table 4-1:** Cumulative amp-hour charge throughput prior to observed stable RTE decline.

| Amp-hour (Ah) throughput | | | |
|---|---|---|---|
| Battery 1 | Battery 2 | Battery 3 | Battery 4 |
| 255.2 | 200.4 | 296.7 | 314.7 |

RTE declines resulted in highly inefficient battery charging, observed both immediately after inverse charging (Figure 4-2), and spontaneously during regular cycling near the end of life (Figure 4-3). Poor battery charging took the form of voltage suppression (or charging overpotential reduction), where voltages during charging were unable to meet +2.45 vpc cutoffs for regular charge currents ($C_{20}$/10), or similarly observed as increased charge currents during applied constant +2.45 V overpotentials. For batteries that were unable to meet +2.45 vpc cutoffs per the protocol in *Section 4.1.1*, a 1.5 Ah charge limit was imposed. Figure 4-2 illustrates periods of charge voltage suppression, and subsequent recuperation during cycling immediately post-inverse charging. Figure 4-3 illustrates decreased charging overpotentials of the negative electrode as it spontaneously emerges in Battery 4 after 534 cycles, with the condition exacerbated through consecutive cycling.

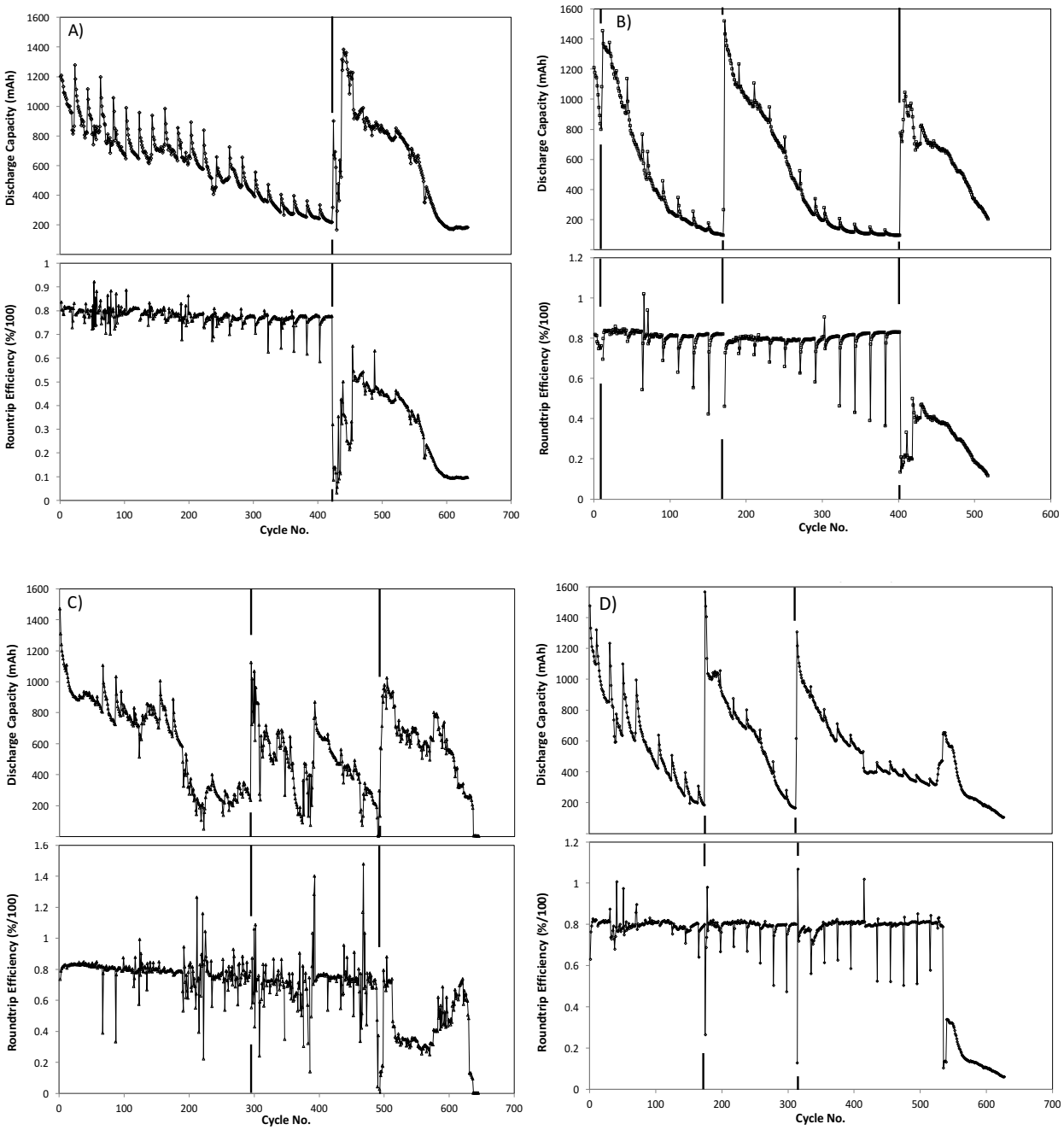


**Figure 4-1:** Yuasa battery discharge capacity and roundtrip efficiency data. Data sections demarcated by broken black bars indicate point of inverse charging. **A)** Battery 1 performance data. **B)** Battery 2 performance data. **C)** Battery 3 performance data. **D)** Battery 4 performance data.

Voltage suppression is attributable to three factors: 1) antimony poisoning intensified by inverse charging, 2) critical active material shedding resulting in short-circuit pathways in batteries, and 3) accelerated battery interconnection shorting.

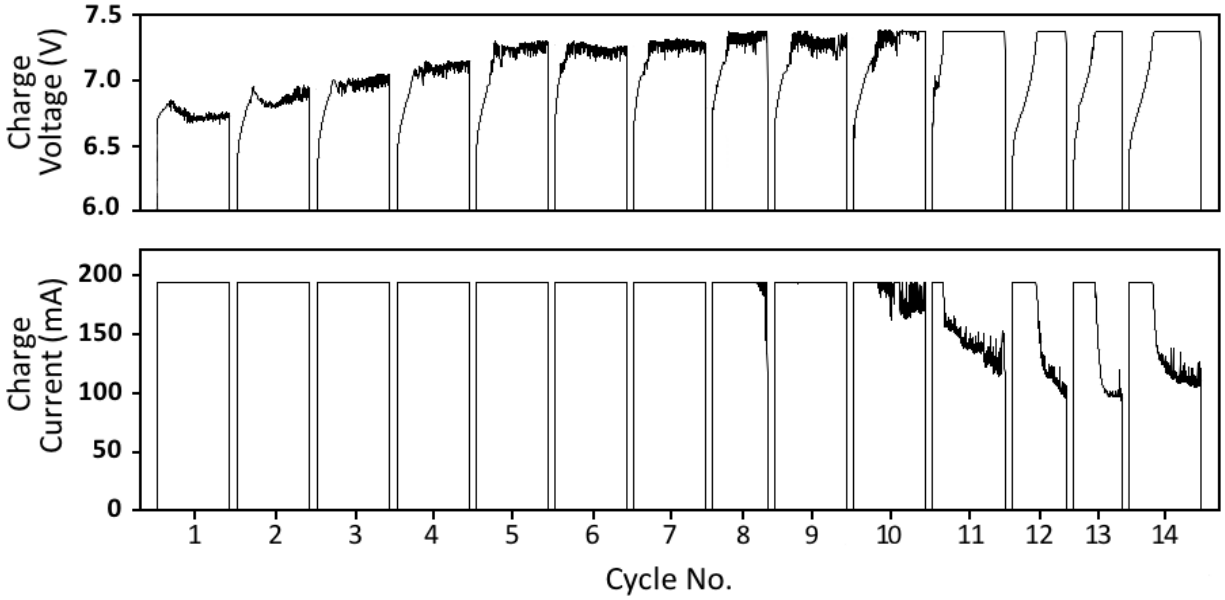


**Figure 4-2:** Temporary voltage suppression for the first few cycles immediately post inverse-charging observed in all studied batteries.

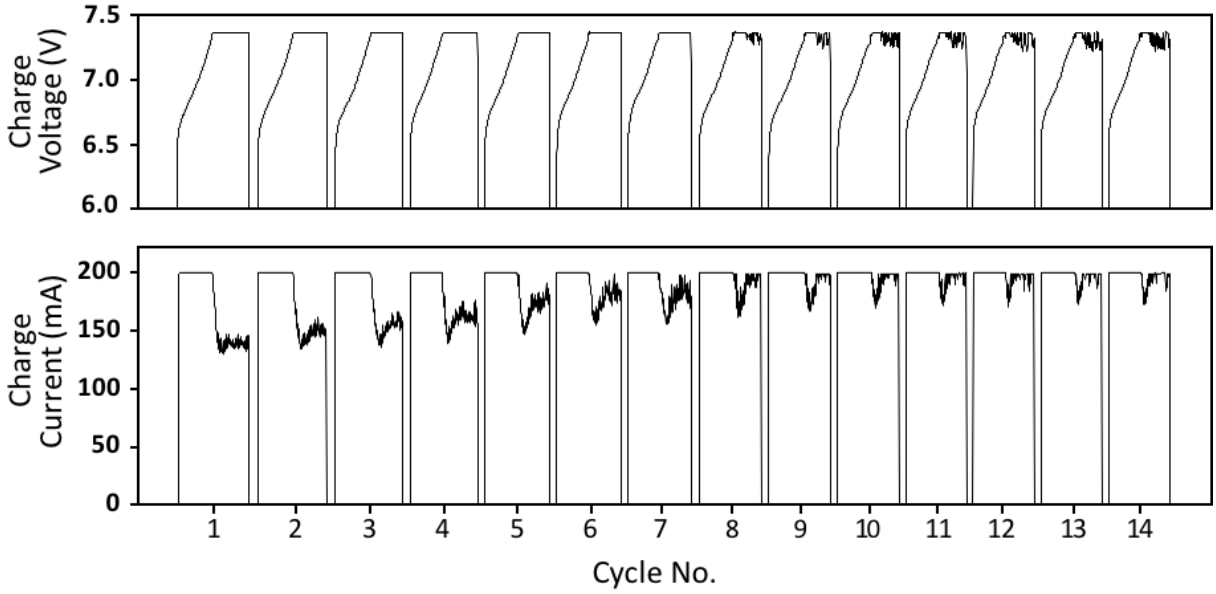


**Figure 4-3:** Charge voltage suppression evolution after cycle 534 for Battery 4. Voltage suppression corresponds with increasing charge currents during CV holds.

### 4.2.3. Antimony poisoning effects

Voltage suppression that temporarily surfaced for the first few cycles after inverse charging in Batteries 1-4 (Figure 4-2) is attributable to local antimony poisoning introduced during the inverse charge protocol. Sb additions of approximately 5.7 wt % are added to flooded PbA positive grid alloys to enhance $PbO_2$ oxidation, reduce PAM crystallinity, and improve PAM reversibility [106]. Dissolved antimony concentrations were observed to increase during inverse charging and recharging (Table 3-2). Pentavalent and trivalent antimony alloys in the positive electrode grid are reduced to antimony metal during inverse charging. Antimony metal is only slowly dissolved by dilute acid. During cell reversal, increased quantities of trivalent antimony are formed during oxidation ($E_{Sb/Sb_2O_3}$ = +0.15 V vs. STP $H_2$ electrode) [27,99]. Trivalent antimony is found to have less ability to form stable hydrates or reincorporate into the PAM than Sb(V), which forms $Sb_4O_4(OH)_2SO_4$. Sb(III) preferentially migrates to the negative electrode [107,108]. Once deposited on the negative electrode, it is well known that metallic antimony (unlike tin) reduces the hydrogen evolution overpotential of the anode, resulting in lower charge voltages, increased hydrogen evolution, and decreasing roundtrip efficiency [19]. As the battery is cycled, local deposits of metallic Sb are covered by lead metal during dissolution precipitation reactions, and antimony effects are diminished with time, causing charge voltages to rebound after 10 cycles (Figure 4-2). Antimony poisoning could also be accelerated during regular cycling of batteries with internal defects or small short circuits. In these cases, slight electrode polarity reversal of positive electrodes in the weakest cells may be occurring.

### 4.3.4. Shedding and intra-cellular short-circuiting

Yuasa 6N2-2A batteries are designed for use as motorcycle starter batteries and are not engineered for deep-cycling applications due to thinner plate construction with weaker particle cohesion. Poor cohesion is a result of smaller paste particle precursors and lower cure times as compared to industrial batteries made of 4BS paste [23]. Additionally, inverse charging of laterally unrestrained new positive and negative Yuasa electrodes indicates that PAM is largely retained while NAM is excessively dislodged and shed (Figure 4-4). Because external negative electrodes in each of the YUASA battery cells is unsupported, accelerated shedding is observed in these plates during battery post-mortem examinations due to active material growth and spall. Plate growth, expansion and buckling are also commonly reported challenges for PbA negative electrodes that experience a full charge after a long period of duty in a partial state of charge. Accumulation of shed active material on the bottom of the battery case provides a conductive path between adjacent electrodes, resulting in electrode shorting upon battery charging. During discharge, conversion to insulating $PbSO_4$ discontinues shorting.

In addition, Yuasa battery separators were observed to undergo significant oxidation for both inversely charged and regularly cycled batteries. In Yuasa starter batteries, the separator contains a mixture of synthetic and organic sheet-forming fibrous materials and binders (resin fibers such as polyester, polypropylene or acrylonitrile, or natural cellulose) [109]. Oxidation of binder materials by the positive plate (or negative during inverse charging) causes a gradual decomposition, dissolution, and loss of structure. Decomposition of battery separators allows electrode piercing and short circuiting [20].

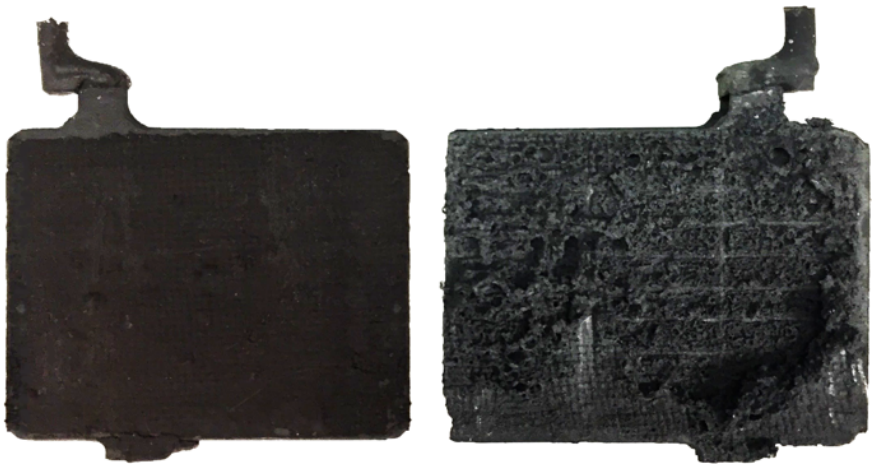

**Figure 4-4:** New Yuasa positive electrode (left) and negative electrode (right) after inverse charging.

The effect of shedding in causing internal shorts and in diminishing discharge capacities is clearly illustrated in Figure 4-5. Figure 4-5 shows battery discharge data for Battery 4 after undergoing a series of tests. Inverse charging at cycle 627 resulted in a modest capacity increase but did not correct for observed charge voltage suppression (Figure 4-5b); Electrolyte replacements and the removal of shed active material sludge was also ineffective (Figure 4-5c,d). Battery 4 was therefore deconstructed; the three cells were wired and cycled independently as three 2 V cells (Figure 4-5e). All three cells exhibited voltage suppression and low discharge capacity. When the oxidized separators of Cell 1 were replaced with a Daramic polyethylene membrane layered with new fiberglass mat, charge voltages resurged, and discharge capacity and efficiency was replenished (Figure 4-5f), indicating prior electrode shorting through the separator.

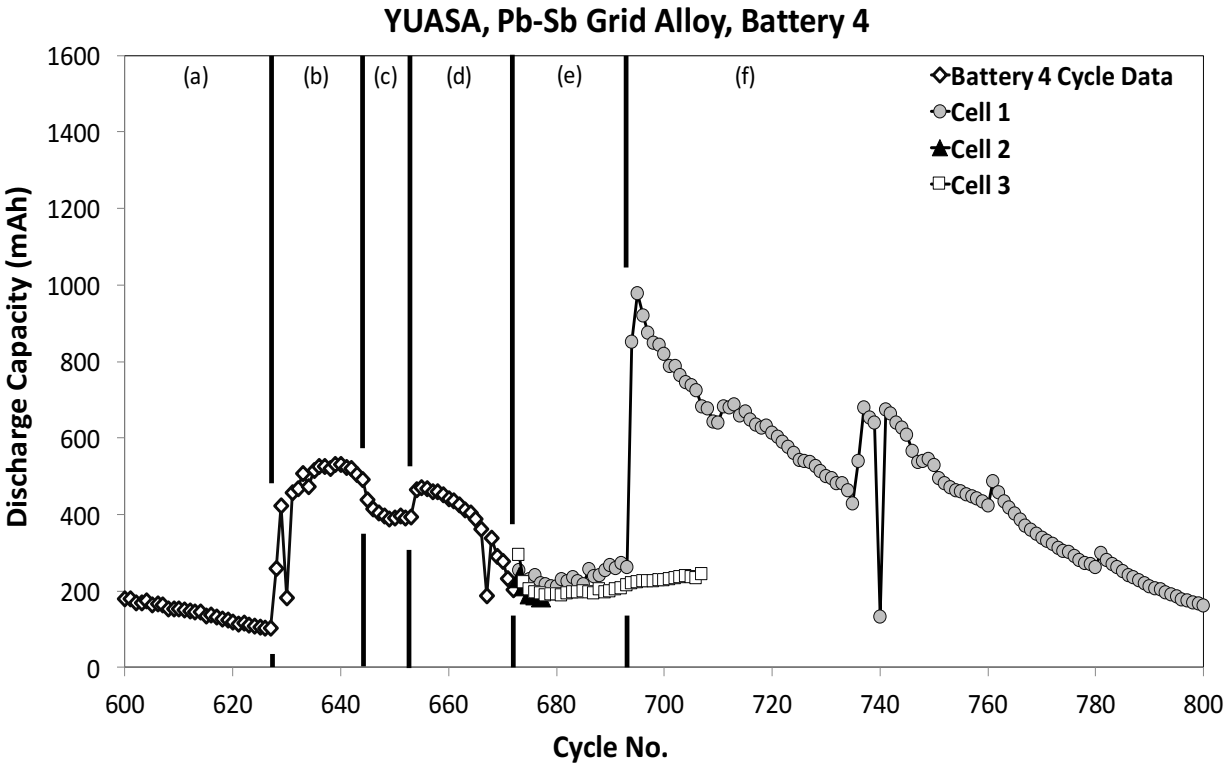


**Figure 4-5:** Cycle performance data for Battery 4 and at cell level: **a)** original unmodified battery. **b)** battery performance after inverse charging. **c)** battery performance after electrolyte replacement. **d)** battery performance after shed active material removal and battery cleaning. **e)** individual cell level performance. **f)** Performance of Cell 1 post-separator replacements.

### 4.2.5. Inter-cellular short-circuiting

Battery 1 was dissected upon final removal from cycling and cleaned of all evident active material sludge that could have shorted electrodes. Oxidized Yuasa separators were discarded and replaced with new OEM fiberglass separators and positive electrodes were encapsulated in Daramic™ porous polyethylene pouches. However, voltage suppression remained unchanged, as displayed in Figure 4-6. Charge voltages remained incapable of reaching the voltage cutoff of +7.35 V (+2.45 vpc) at the $C_{20}$/10 rate.

Although negative electrodes are cathodically protected from grid corrosion, corrosion occurs due to dilute acid sprays, and inverse charging is seen to exacerbate inter-cell connection corrosion [27]. Modern batteries use through the wall welding to connect cells on mono-block

battery cases, which are sealed to prevent inter-cell shorting [20]. Figure 4-7 presents a schematic illustration of inter-cell short-circuiting failure. Dilute films of acid corrode negative terminal interconnects by converting the surface to $PbSO_4$, a 2-electron process penetrating twice the depth of Pb to $PbO_2$ conversion. Pb → $PbSO_4$ corrosion is continuous during regular cycling, and formed $PbSO_4$ films create mechanical stresses and cracks that further increase corrosion rates [27]. Although inter-cell connector corrosion was observed to occur in regularly cycled Yuasa batteries, inverse charging was seen to worsen the condition, causing permanent short-circuiting immediately after inverse charging, as in Battery 1.

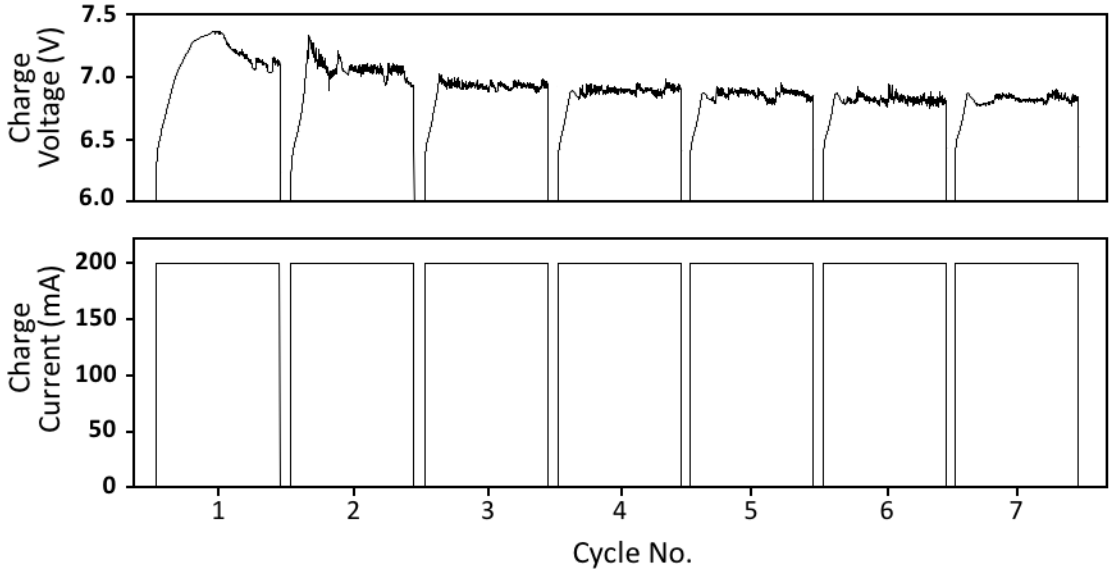


**Figure 4-6:** Charge voltage and current data for battery 1 at the end of life. Separator replacements, battery cleaning efforts and electrolyte replacements were inadequate at eliminating suppressed charge voltage. Charging was limited to 1.5 Ah due to inability to reach voltage limits.

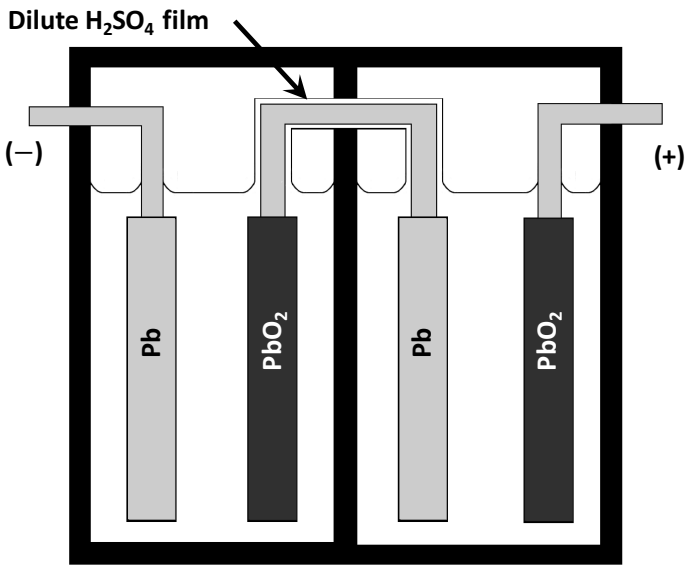


**Figure 4-7:** Inter-cellular short circuiting schematic for a model 4 V (2-cell) PbA battery. Dilute $H_2SO_4$ films create continuous electrolyte contact between previously isolated cells.

### 4.2.6. Active material shedding and BET of failed Yuasa Pb-Ca/Pb-Sb

Battery 5 consisted of a singular Yuasa 6N2-2A battery cell (2 V), fabricated using OEM electrodes and casing dimensions. Additional OEM Yuasa glass mat separators were added to laterally restrain previously unsupported negative plate groups to prevent spall from inverse charging. The battery cell was cycled and overcharged per the protocol in *Section 4.1.1*. Small electrode samples were extracted pre- and post- inverse charging for x-ray phase analysis and BET analysis (full data is presented in Appendix C). The cell voltage was monitored at all stages of cycling and inverse charging. These samples help more fully examine the origins of capacity decline, extent of desulfation, and of active material shedding for each electrode group. The performance data for this battery is displayed in Figure 4-8. and is seen to obey the same performance with cycle number as previously cycled batteries (Figure 4-1), including the same resurgence in capacity post-inverse charging. Discharge capacity is not fully recoverable post inverse charging due to loss of PAM through shedding.

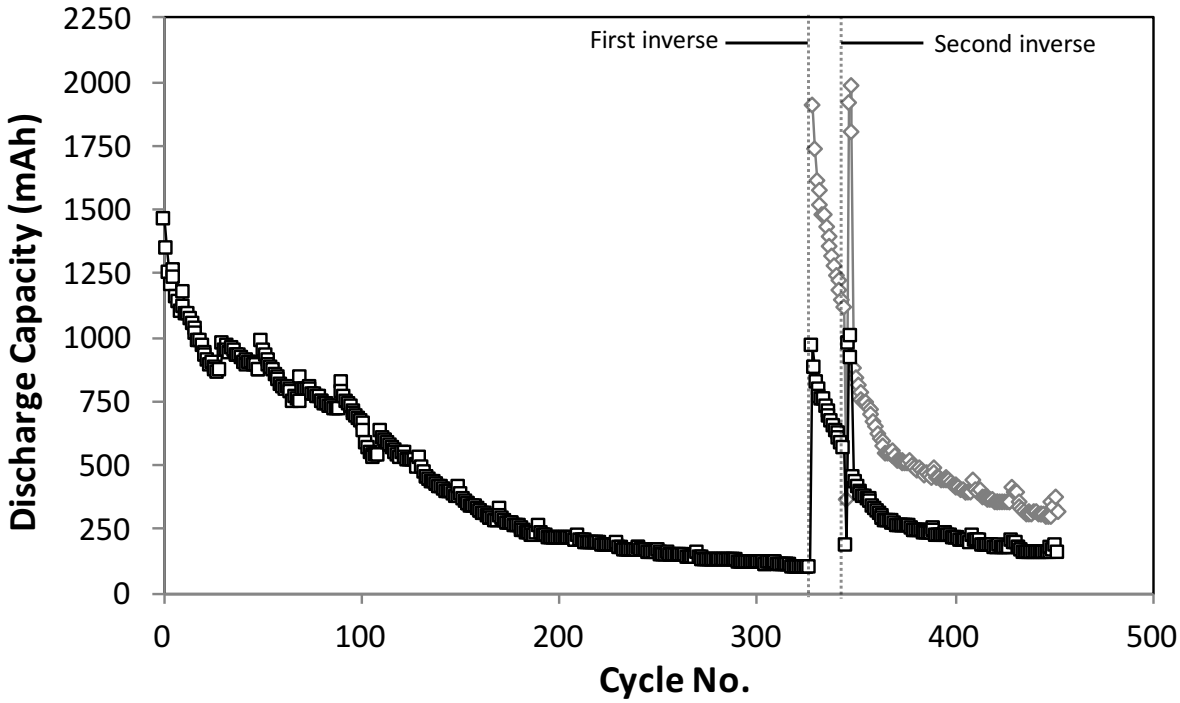


**Figure 4-8:** Discharge capacity for a single YUASA 6N2-2A cell (Battery 5). Data post-inverse charging is shown as actual (measured) in black, and scaled to account for active material loss in grey. Data sections marked by broken black bars indicate points of inverse charging.

During the first 327 cycles, measurements of active material loss indicate that the negative electrode shed 19.0% (0.058%/cycle) during regular cycling, while the positive electrode shed 49.2% (0.15%/cycle). Inverse charging resulted in PAM shedding of 6.93% of pre-inverse weight, while NAM shed 6.93% of pre-inverse weight. Shedding is significantly higher for NAM than PAM per cycle, results in line with PbA research that describe PAM shedding as a predominant failure mode [1,27,40]. Inverse charging is seen to aggravate shedding for both electrodes to an equivalent extent (when laterally restrained). Negative electrode growth has been observed through SEM imaging on all occasions. Inverse charging of positive electrodes largely retains initial structure while significantly altering crystallinity and phase (addressed below), whereas inverse charging of negatives completely reduces particle size and alters structure [110]. Table 4-2 gives the discharge capacity of each electrode normalized by gram of remaining active material.

**Table 4-2:** Measured electrode discharge capacities of Battery 5 at the $C_{20}/10$ discharge rate, using a -0.9 V cutoff for negatives and a +0.75 V cutoff for positives.

| | Discharge Capacity (mAh/g) | | | |
|---|---|---|---|---|
| | New | 327 cycles | Post-inverse | Post-second inverse |
| **Negative** | 154.9 | 177.7 | 155.3 | 145.6 |
| **Positive** | 100.8 | 40.4 | 131.5 | 137.0 |

Capacity is seen to increase for negative electrodes through regular cycling, indicating good electrode health, while positive electrodes are observed to store significantly lower energy per gram. This finding lends support to the theory that positive electrodes experience significant declines in capacity due to loss of cohesion [111]. Positive plates expand and contract on cycling [112,113]. Meissner [114] determined that shedding was exaggerated for batteries cycled at low recharge rates and high discharge rates, selectively degrading the mechanical and electronic contacts of the interparticle neck-zone of PAM structure. Post-inverse charging, discharge capacity is seen to decline 12.6% for the negative electrodes, while increasing by >225% for the positives to levels surpassing new Pb-Sb battery electrodes.

Further analyses were conducted using BET surface area measurements displayed in Table 4-3. Strong sulfation was observed on the lower portion of the negative electrodes (confirmed via x-ray) and results are presented for both upper and lower NAM regions. High BET values are proportional to the quantity of micropores (<0.1 μm pore radius), sites that facilitate chemical reaction so long as adequate transport is provided by macropores (>0.1μm) [112]. BET values are consistent with those reported in the literature. Leady oxide paste is found to vary from 0.7-1.4 $m^2/g$ for Barton pot preparation and 2.4-2.8 $m^2/g$ for ball mill preparation [21]. For PAM in SLI batteries, BET values typically range from 3-8 $m^2/g$ [34].

**Table 4-3:** Electrode BET surface area measurements at key points pre- and post-inverse charging for Battery 5.

| | Surface Area (m2/g) | | | |
|---|---|---|---|---|
| | New | 327 cycles | Post Inverse | Post-second inverse |
| **Negative (upper)** | 0.85 | 1.22 | 0.64 | 0.50 |
| **Negative (lower)** | 0.85 | 0.41 | 0.55 | 0.27 |
| **Positive** | 3.14 | 3.67 | 5.44 | 10.09 |

NAM BET decreases after inverse charging indicate losses of small particles at the expense of large pore formations and sulfation processes [104]. Although inverse charging works to create small Pb and $PbSO_4$ crystals in pure lead metals [51], microstructures are quickly lost upon completion of the procedure on porous negative electrodes (reducing the energetic component, $G_e$) without adequate expanders to control nucleation and prevent particle fusion, [115]. Degradation of the NAM skeleton is also apparent for inversely charged YUASA Pb-Ca negatives (*Section 3.3.3*).

PAM capacity is understood to be proportional to surface area in Pb-Sb electrodes [116], with BET and capacity strongly correlated with the quantity of β-$PbO_2$ [117]. While Table 4-3 indicates inverse charging increases in PAM BET by ~1.5×, the resurgence in positive electrode discharge capacity increased to a much greater extent. Hence, the influence of inverse charging on the positive electrode works by preferentially restoring mechanical and electrical particle neck zones, while also working to increase the number of micropores (β-$PbO_2$ content). During the second inverse charge, further micropore increases fail to result in significant capacity improvement, presumably due to negligible increases to the volume of macropores in positive electrodes. In this instance, PAM utilization is limited by ion diffusion, and not conductivity [118].

Electrode samples were analyzed via x-ray diffraction with results displayed in Table 4-4. New negative electrodes are seen to consist of 62.8% lead metal, with 30.6% as β-PbO, and very

low 3BS. As such, YUASA electrodes appear to be formed from weak 1BS paste, using more concentrated acid during preparation, as β-PbO forms in the presence of abundant $SO_4^{2-}$ [104]. Although thermodynamically unstable in $H_2SO_4$, β-PbO reacts very slowly, due to low solubility and limited $SO_4^{2-}$ diffusion, whereas α-PbO forms in alkaline environments and provides greater structure and cycle life [21,22]. After 327 cycles, electrolyte stratification creates a sulfated lower electrode portion and dilute acid upper regions (high 3BS concentration). Immediately post-inverse charging, sulfate levels are seen to dramatically increase. This is also seen to be true after the second inverse charge. These high sulfate levels correlate with diminished electrode capacity, and decreased interparticle contact.

**Table 4-4:** X-ray diffraction Rietveld refinement phase composition of electrode samples during key points pre- and post-inverse charging for Battery 5. Samples for the second inverse charge were analyzed 5 cycles after inverse charging.

**Negative YUASA Pb-Ca Electrodes**

| | *Pb* | *β-PbO* | *$PbSO_4$* | *3BS* | *Other* |
|---|---|---|---|---|---|
| New | 62.8 | 30.6 | 0 | 6.6 | 0 |
| 327 cycles (upper) | 36.5 | 10.5 | 10.8 | 40.8 | 1.4 |
| 327 cycles (lower) | 8.5 | 0 | 91.5 | 0 | 0 |
| Inverse 1 (upper) | 11.7 | 6.9 | 60.9 | 14.7 | 6 |
| Inverse 1 (lower) | 8.9 | 0.5 | 84.8 | 2.2 | 3.6 |
| Inverse 2 (upper) | 16.2 | 1.7 | 74.2 | 7.7 | 0.2 |
| Inverse 2 (lower) | 6.4 | 0 | 93.6 | 0 | 0 |

**Positive YUASA Pb-Sb Electrodes**

| | α-$PbO_2$ | β-$PbO_2$ | $PbSO_4$ | 3BS | Other |
|---|---|---|---|---|---|
| New | 32.6 | 49.1 | 1 | 7.1 | 10.3 |
| 327 cycles | 90.5 | 9.5 | 0 | 0 | 0 |
| Inverse 1 | 33.7 | 22.9 | 0 | 34.6 | 8.8 |
| Inverse 2 | 4.5 | 95.5 | 0 | 0 | 0 |

Positive electrodes consist primarily of α-$PbO_2$ and β-$PbO_2$, with α-$PbO_2$ forming in alkaline environments and β-$PbO_2$ at the electrolyte interface. Discharge of β-$PbO_2$ proceeds at lower

overpotentials than α-$PbO_2$. α-$PbO_2$ converts to $PbSO_4$ on discharge but the reaction is slowed by dense $PbSO_4$ films, and capacity of this phase is limited [119]. As such, α-$PbO_2$ acts as a glue, while β-$PbO_2$ contributes preferentially to capacity [120,121]. Forming batteries from larger 4BS particle paste precursors (optimally 15-25 μm × 3-5 μm) yields a majority of α-$PbO_2$ phase, giving lower utilization but better mechanical support and cycle life [22]. Conversely, PAM consisting purely of β-$PbO_2$ has high capacity and low cycle life [22]. For paste-based batteries, the proportion of α/β-$PbO_2$ in new positive electrodes should be 1:1 to balance capacity and cycle life. Yuasa positive electrodes have initial α/β-$PbO_2$ = 0.66 [122]. After 327 cycles, β-$PbO_2$ content is seen to decrease, which is attributed to preferential shedding of β-$PbO_2$ active material. BET increases post-inverse charging in PAM are attributable to phase transformation to β-$PbO_2$, yielding increases in capacity, but having greater tendency for active mass shedding.

PAM has both amorphous $PbO(OH)_2$ and crystalline composition, providing electron conductivity and proton transport. Valerioté correlates PAM capacity to the amorphous (hydrate) content, with β-$PbO_2$ hydrated significantly more than α-$PbO_2$ [123–126]. Inverse charging is therefore seen to enhance the amorphous content by converting α-$PbO_2$ to β-$PbO_2$ by exposing greater quantities of PAM agglomerates to $H_2SO_4$. Furthermore, antimony hydrate incorporation slows $PbO_2$ agglomeration and dramatically reduces crystallinity [124,127–129]. General improvements in capacity post-inverse charging indicate improved electrode hydration and a restoration of particle neck zones.

### 4.2.7. Extended overcharging investigations

To understand whether extended overcharging can recover battery capacity in a similar fashion to inverse charging, two YUASA 6N2-2A batteries were cycled per the protocol in *Section 4.1.1* with overcharging every 20 cycles until failure. The batteries were then fully charged and held at +2.5 vpc for 5 days to determine the extent of capacity improvement solely achievable from overcharging. The results presented in Figure 4-9 show that extended overcharging is unsuccessful in recovering battery capacity in the positive electrode. Battery 6 had a negligible capacity increase, whereas Battery 7 had a minor increase of only ~100mAh in total discharge capacity. These results indicate loss of inter-particle contact in the PAM is permanent and not fixed by traditional means of maintenance [114].

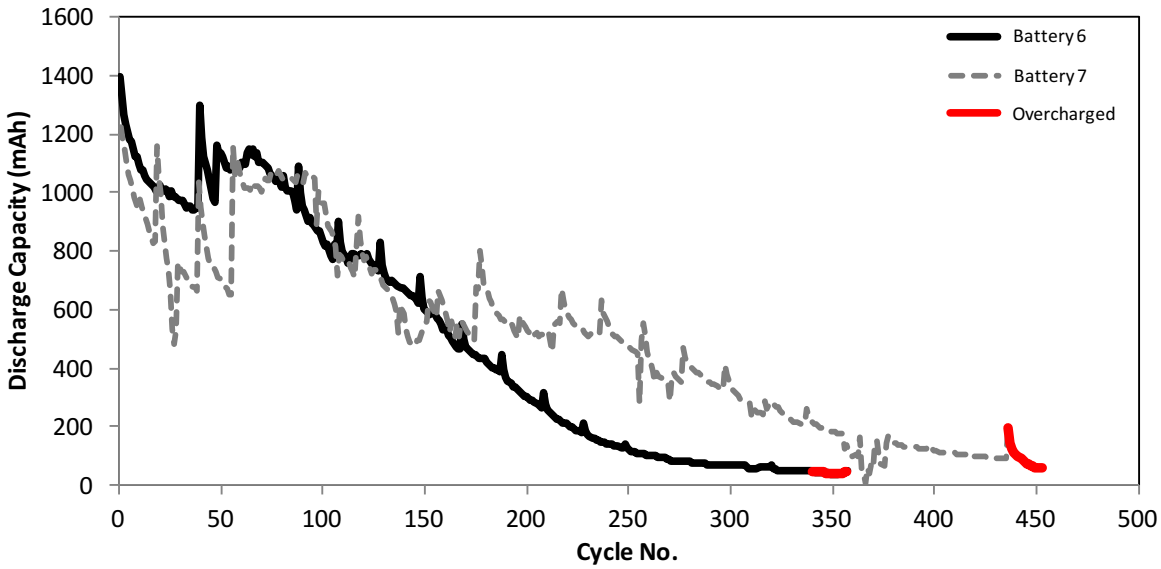


**Figure 4-9:** Discharge performance data illustrating the effects of extended (5 day) overcharging at +2.5 vpc.

### 4.2.8. Characterization of failed Powersonic Pb-Ca/Pb-Ca-Sn

A PowerSonic Pb-Ca/Pb-Ca-Sn VRLA battery was cycled to 52.6% of initial discharge capacity with an average roundtrip efficiency of 81.8% (Figure 4-10). The battery was subsequently

dissected and electrodes removed and cleaned. It was observed that >50% of PAM active material was shed from the positive electrodes. Because inverse charging of Pb-Ca-Sn positives was observed to be destructive (*Section 3.3.1*), only Pb-Ca negatives were examined for extent of sulfation failure and potential recovery.

Two negative electrodes were cycled individually in an H-call setup as described in *Section 4.2.4* and tested independently for phase (x-ray), surface area (BET), and discharge capacity improvements pre- and post- inverse charging with results illustrated in Figure 4-11 and Table 4-5.

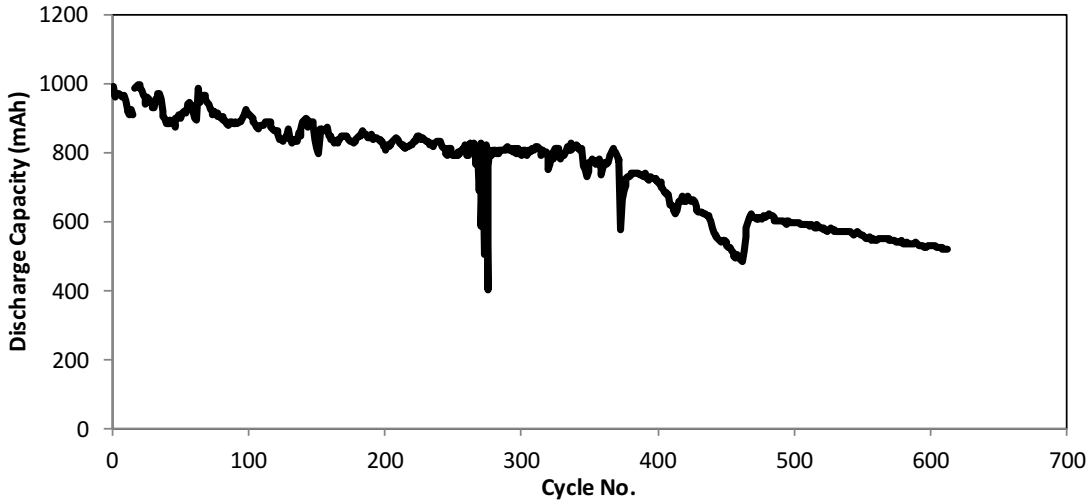


**Figure 4-10:** Discharge performance data for PowerSonic 612 AGM VRLA battery.

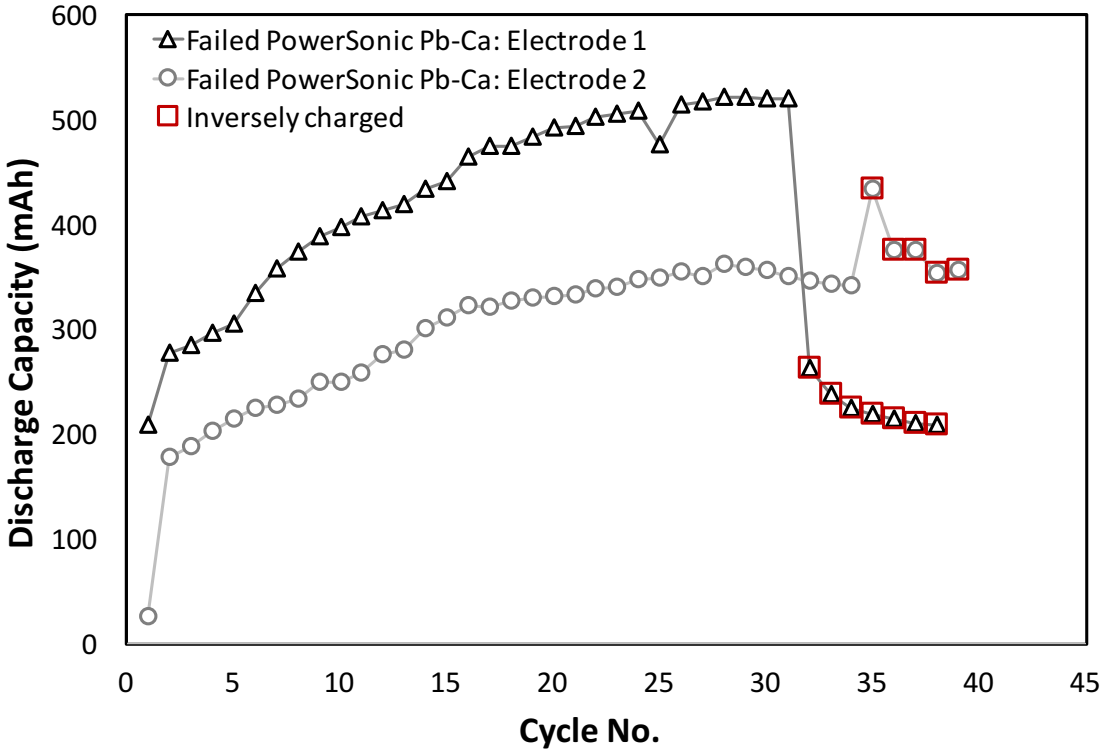


**Figure 4-11:** Performance data for individual failed PowerSonic Pb-Ca negative electrodes.

**Table 4-5:** XRD Rietveld refinement phase composition of failed PowerSonic Pb-Ca electrode samples during key points pre- and post-inverse charging.

| **Failed PowerSonic Pb-Ca Electrodes** | | | | | | |
|---|---|---|---|---|---|---|
| | **BET Area** | **XRD Phase Composition** (%) | | | | |
| | *($m^2/g$)* | *Pb* | *PbO* | *$PbSO_4$* | *3BS* | *Other* |
| Electrode 1: failed | 1.02 | 23.6 | 10.8 | 50.7 | 13.1 | 1.8 |
| Electrode 1: post-inverse | 1.63 | 4.5 | 1.1 | 83.6 | 4.5 | 6.3 |
| Electrode 2: failed | 1.12 | 14.3 | 3.5 | 74.1 | 7.7 | 0.4 |
| Electrode 2: post-inverse | 0.56 | 8 | 1.3 | 83.2 | 6.2 | 1.3 |

As Figure 4-11 illustrates, both electrodes experienced a significant rebound in capacity with repeated cycling, due to prior inadequate charging imposed by positive electrode limits. Once stabilized, both electrodes remained <80% of new PowerSonic Pb-Ca electrode capacity (700 mAh). Prior to inverse charging, electrodes were extensively charged and sampled. X-ray results indicate both electrodes were significantly sulfated (>50% $PbSO_4$), with electrode 2 sulfated to a much greater extent (74.1%). Inverse charging resulted in a dramatic increase in $PbSO_4$ content

for both, but dramatically increased BET surface area for electrode 1. This divergence is comparable to results for inversely charged Yuasa Pb-Ca electrode "New 3" in Table 3-3. The electrode with the greatest capacity decline exhibited an increase in BET values well above initial readings, indicating that conductive pathway destruction resulted in an inability to fully recharge portions of energetic NAM, once structural connections ($G_s$) were fully oxidized to higher surface area $PbO_2$. This result, in contrast with BET decreases for electrode 2 indicate that inverse charging temporarily results in significant micropore increases for the negative electrode during conversion from Pb → $PbO_2$, coupled with even greater losses of this energetic structure during reduction of $PbO_2$→ Pb, depending on the extent of completion of the transformation. These results further emphasize the importance of controlled nucleation and maintaining conductive pathways and interparticle connectivity for NAM electrodes.

## 4.4. Conclusion

Flooded PbA batteries of lead-antimony (Pb-Sb) positive and lead-calcium (Pb-Ca) negative grid alloy construction were continuously cycled and periodically subjected to overcharging and inverse charging as a capacity recovery strategy. Traditional prolonged overcharging techniques were demonstrated to be inadequate at appreciably regenerating battery capacities, providing only marginal increases (Figure 4-9). On the other hand, inverse charging was shown to be highly successful on all batteries independent of states-of-health (Figure 4-1). Batteries with poor states-of-health (discharge capacities <15% of initial values) experienced almost perfect discharge capacity restoration post- inverse charging. Temporary antimony poisoning induced charging inefficiency lead to suppressed voltage, but was recovered after 10 cycles (Figure 4-2).

For the negative electrode, BET and x-ray investigations indicate that large $PbSO_4$ crystals in negative electrodes are oxidized, creating extensive micropore networks during oxidation from Pb → $PbO_2$, gains that are lost during conversion back to sponge lead due to uncontrolled nucleation. Strong differences between PAM and NAM indicate that upon completion of inverse charging, PAM experiences growth in surface area and short-lived regeneration of interparticle connectivity. Inverse charging of PAM largely retains original electrode structure, while undergoing a strong transformation of structural α-$PbO_2$ to energetic β-$PbO_2$ into weakly interconnected agglomerates with higher capacity. On the other hand, complete inverse charging negatively impacts both the energetic (microporous network) and structural components of NAM, as $G_e$ is found to be subsumed into a thinner (macroporous), more fragile skeletal Pb framework.

PAM shedding occurred during regular cycling and overcharging, and shedding spiked during inverse charging. Excessive NAM detachment and loss of cohesion post-inverse charging is also observed on laterally unrestrained electrodes. Although inverse charging was seen to have only a minor influence on the shedding rate of the positive, conversion to weakly interconnected β-$PbO_2$ indicates acceleration of this failure mode. Shedding was responsible for intra-cellular short-circuiting post-inverse charging (Figure 4-5). Grid growth and inter-cellular electrolyte contact resulted in permanent short circuiting that was similarly exacerbated by inverse charging (Figure 4-7).

# 5. Main conclusions and future work

ALAB improvements to cycle life over PbA systems, while significant, must be paired with further improvement to the capital cost of the chemistry to ensure its future viability against Li-ion. Capital cost reductions are achieved through increased active material utilization ($\eta_{util}$) without negatively impacting cycle life. Despite advances toward thinner lead grids and posts in reducing battery lead demand, it is generally understood that cycle life and $\eta_{util}$ are inversely related for battery systems. In traditional PbA batteries, thicker plates constructed with well-cured 4BS paste precursors correlate with lower $\eta_{util}$ and increased battery cycle life. By the same token, increases in active material paste density lowers macroporosity and $\eta_{util}$ while increasing cycle life. $\eta_{util}$ can also be restricted by simply limiting the quantity of acid in the battery available for reaction, again resulting in cycle life enhancement [27]. It becomes clear that current techniques of manufacturing, subjecting paste of a design density to cure, dry, and soak, impose real limitations to sustainable specific energy increases through $\eta_{util}$ improvements.

Inverse charging investigations conducted on Pb metal rods and porous battery electrodes indicate that electrode polarity inversion can potentially yield significant increases in electrode surface area and capacity. However, long-term cycle life investigations illustrate that while potentially beneficial to enhancing electrode energetic capacity, inverse charging significantly aggravates other battery failure modes, accelerating the deterioration created by regular cycling. Inverse charging, as this research has shown, preferentially reduces particle size in both the positive and negative electrodes (micropore generation). This works to increase BET surface area (for negative electrodes, fine particles are observed to agglomerate and BET decreases upon

transformation from $PbO_2$ → Pb) and energetic portions, at the expense of the structural components of the battery electrodes.

For the PAM, dramatic increases in surface area are observed, with capacity regeneration primarily attributable to restoration of inter-particle connectivity coupled with large increases in surface area, achieved by converting structural $\alpha$-$PbO_2$ to energetic $\beta$-$PbO_2$. $\beta$-$PbO_2$ has weaker cohesion with other particles, and weaker adhesion to the current collecting Pb grid than $\alpha$-$PbO_2$. PAM subsequently sheds from the positive electrode grid to a higher degree, although in appearance the electrode seems to be in good condition [1,130].

For the NAM, more limited success was achieved for porous electrodes as compared to Pb rods. Results indicate that inverse charging works to reduce $PbSO_4$ content and improve surface area, with success strongly dependent on initial particle size and cohesion, as well as on the parameters of the protocol itself. PbA batteries contain varying degrees and types of irreducible (or passive) lead sulfate with a wide range in crystallite size differences. It was shown that dense $PbSO_4$ films impede electrolyte transport and fully prevent oxidation, resulting in exacerbating electrode failure post-inverse charging. Successful inverse charging (low peak voltage) on negative electrodes increased surface area while partially modifying structure (Figure 3-20b). Unsuccessful inverse changing (high peak voltage) resulted in a loss of surface area and capacity while completely altering structure (Figure 3-26).

The idea of employing inverse charging as a means of doubling battery cycle life and increasing specific energy on existing varieties of PbA batteries is met with mixed results, as was evident from long-term testing. As such, several main areas of research may work to improve the efficacy of the process and limit the emergence of other failure modes.

## 5.1. Future work

### 5.1.1. Electrode expanders, nucleating agents, and matrix modifiers

Inverse charging destroys structural connectivity in the electrodes while emphasizing energetic capacity. While this has the potential to dramatically increase $\eta_{util}$ and specific energy, alternatives and/or complements to pure Pb as the structural (matrix) material must be identified before the technique can be successfully employed. As such, recent advances by the ALABC on the introduction of electroactive carbons (graphene, nanotubes and activated carbon) to serve as nucleation sites during dissolution-precipitation reactions should be investigated. The addition of activated carbon (from TDA Research, Inc.) in >2 wt% was found to promote nucleation of Pb and maintain electrode conductivity throughout the negative electrode during cycling [131].

Fundamental to the negative electrode is the process of recrystallization, whereby small particles (most often amorphous) dissolve and big crystals grow per the Ostwald-Fruendlich equation (Eqn. 1-24). For traditional PbA manufacturing, this has driven research into expander materials (lignosulfonates, carbon blacks, etc.). More recently, electroactive carbons successfully suppressed sulfation failure, avoiding the emergence of dense $PbSO_4$ films that can contribute to dramatic failures post inverse charging. Future research on inverse charging can leverage promising findings on carbon and other nucleating agents or electrode expanders to retain fine particle size and adequate connectivity post-completion of the technique.

### 5.1.2. Inverse charging of 4BS paste batteries

The study hereby conducted primarily employed batteries of a construction intended for automotive starter applications. Such batteries fabricated with 1BS and 3BS paste are easily damaged by deep discharging, due to smaller particle sizes and weaker structural interconnections. Failures through active material shedding were observed and expected. The

initial particle size of the NAM and PAM, dependent on the extent of plate curing, strongly impacts the degree of structure loss post-inverse charging. As has been shown, in the NAM, particles below a critical size are fully oxidized upon inverse charging, resulting in loss of structure and conductive pathway degradation after the technique is completed. In addition, small particles in PAM are more completely converted to β-$PbO_2$. Inverse charging should be further investigated on the benefits and challenges afforded by the technique on more robust industrial batteries, formed from larger 4BS crystals.

### 5.1.3. Adaptive protocols and maximum voltage limits

Two criteria are deemed important when developing inverse charge protocols. First, low to moderate current densities are preferable for electrode forming processes, as they more closely match $PbSO_4$ nucleation, enable uniform reaction products, and promote greater surface area [18,46]. The second criterion is the penetration depth observed created during inverse charging of the negative electrode, a factor largely controlled by length of time at more oxidizing peak voltages [105]. The length of time at an oxidation voltage necessary to ensure complete oxidation of energetic lead sulfate to lead dioxide, while not disrupting structural Pb depends on the battery's initial state-of-health, and protocols must therefore be adaptive.

Inverse charging was shown to be beneficial to PowerSonic Pb-Ca negatives using CV protocols with lower peak voltage (*Section 3.3.1*), and destructive to negatives studied in isolation with CC protocols, experiencing higher peak voltage (*Section 3.3.3*). These results hint at the importance of the magnitude of corrosive penetration depth that the negative electrode can receive during the process. It is now understood that there may be an optimum voltage that prevents full structural oxidation, and the irreversible loss of structural connections (resulting in capacity declines).

When considering PbA manufacturing, new high-current formation algorithms have been successful in forming new electrodes in 6-8 h (as opposed to 15-30 h), using adaptive current densities. During battery formation algorithms, reverse charges are commonly employed for the creation of conductive pathways. Further, high rates of formation have been described as creating thicker electrode branches, working to increase conductivity and emphasize electrode structure [26]. Inverse charging conducted at the $C_{20}$/13.3 rate may have optimized the formation of energetic capacity, whereas inverse charging at higher currents should be investigated for the emphasis on maintaining electrode structure. The effect of lower acid concentration during formation could also play an important role in reducing crystallinity and sulfation in the NAM, while promoting the formation of $\alpha$-$PbO_2$ skeleton in the PAM, increasing the $\alpha/\beta$-$PbO_2$ ratio [132].

### 5.1.4. Electrolyte additives

Dense $PbSO_4$ failed to be oxidized during the technique, resulting in interior pore hydration, converting the electrode to a semipermeable membrane upon protocol completion (*Section 3.2.1*, Tests 3-4 and *Section 3.3.1*). To avoid negative electrode hydration, $Na_2SO_4$ addition has been proposed to prevent the concentration of acid from approaching pure water, possibly working to better control dissolution-precipitation reactions and prevent voluminous $PbSO_4$ crystal deposits [20]. $Na_2SO_4$, however, has been found to increases corrosion rates sevenfold, due to the high solubility of $PbSO_4$ by $Na^+$, and cycle life impact needs simultaneous examination [133]. In addition, use of electrolyte additives such as $H_3PO_4$, $H_3BO_3$, $SnSO_4$, and picric acid have the potential of reducing grid corrosion while negligibly impacting the water electrolysis reaction at the anode. Additives of ultrafine carbon, electrochemically oxidized graphite, and $Al_2(SO_4)_3$ added directly to the electrolyte work to increase $PbSO_4$ reduction [134].

### 5.1.5. Hydrogen evolution suppression

Antimony oxides are relatively soluble in sulfuric acid, causing increased hydrogen evolution at the negative electrode, particularly at elevated temperature. Hydrogen evolution can be prevented by the addition of aromatic aldehydes, which are selectively adsorbed by protons present on antimony sites [135].

# Works cited


1. Yang J., Hu C., Wang H., Yang K., Liu J.B. & Yan H. (2016). – Review on the research of failure modes and mechanism for lead-acid batteries. *Int. J. Energy Res.* doi:10.1002/er.3613.

2. Jewell W.T., Ramakumar R. & Hill S.R. (1988). – A study of dispersed photovoltaic generation on the PSO system. *IEEE Trans. Energy Convers.*, **3** (3), 473–478. doi:10.1109/60.8053.

3. Advanced Lead Acid Battery Consortium (2015). – *Prospectus: 2016-2018*. Durham, NC. Available at: http://www.alabc.org/publications/alabc-1618-program-prospectus (accessed on 30 January 2017).

4. Spanos C., Turney D.E. & Fthenakis V. (2015). – Life-cycle analysis of flow-assisted nickel zinc-, manganese dioxide-, and valve-regulated lead-acid batteries designed for demand-charge reduction. *Renew. Sustain. Energy Rev.*, **43** (0), 478–494. doi:10.1016/j.rser.2014.10.072.

5. Moseley P.T. & Rand D.A. (2012). – Partial state-of-charge duty: a challenge but not a show-stopper for lead-acid batteries! *ECS Trans.*, **41** (13), 3–16. doi:10.1149/1.3691907.

6. Pavlov D. & Nikolov P. (2012). – Lead–carbon electrode with inhibitor of sulfation for lead-acid batteries operating in the HRPSoC duty. *J. Electrochem. Soc.*, **159** (8), A1215–A1225. doi:10.1149/2.035208jes.

7. Ebner E., Burow D., Panke J., Börger A., Feldhoff A., Atanassova P., Valenciano J., Wark M. & Rühl E. (2013). – Carbon blacks for lead-acid batteries in micro-hybrid applications – studied by transmission electron microscopy and Raman spectroscopy. *J. Power Sources*, **222** (0), 554–560. doi:10.1016/j.jpowsour.2012.08.089.

8. Moseley P.T., Nelson R.F. & Hollenkamp A.F. (2006). – The role of carbon in valve-regulated lead–acid battery technology. *J. Power Sources*, **157** (1), 3–10. doi:10.1016/j.jpowsour.2006.02.031.

9. Advanced Lead Acid Battery Consortium (2015). – *An overview of the 2016-18 ALABC Program Proposal*. Durham, NC. Available at: http://www.alabc.org/publications/overview-of-the-alabc-1618-program (accessed on 30 January 2016).

10. Yuasa Battery (2014). – AGM & EFB automotive batteries explained. Available at: http://www.yuasa.co.uk/info/technical/agm-efb-explained/ (accessed on 4 October 2016).

11. Marom R., Ziv B., Banerjee A., Cahana B., Luski S. & Aurbach D. (2015). – Enhanced performance of starter lighting ignition type lead-acid batteries with carbon nanotubes as an additive to the active mass. *J. Power Sources*, **296**, 78–85. doi:10.1016/j.jpowsour.2015.07.007.

12. Enos D.G., Ferreira S.R. & Shane R. (2011). – *Understanding the function and performance of carbon-enhanced lead-acid batteries*. Sandia National Laboratories. Available at: http://prod.sandia.gov/techlib/access-control.cgi/2011/113459.pdf (accessed on 3 October 2016).

13. Bača P., Micka K., Křivík P., Tonar K. & Tošer P. (2011). – Study of the influence of carbon on the negative lead-acid battery electrodes. *J. Power Sources*, **196** (8), 3988–3992. doi:10.1016/j.jpowsour.2010.11.046.

14. Hund T. (2008). – Testing and evaluation of energy storage devices. Sandia National Laboratories. Available at: http://www.sandia.gov/ess/docs/pr_conferences/2008/hund_snl.pdf (accessed on 5 October 2016).

15. Pavlov D. (2011). – Fundamentals of lead–acid batteries. In Lead-Acid Batteries: Science and Technology, Elsevier. pp 29–114.

16. Pavlov D. (2011). – Calculation of the active materials for lead–acid cells. In Lead-Acid Batteries: Science and Technology, Elsevier. pp 607–622.

17. Stewart L.L., Bennion D.N. & LaFollette R.M. (1994). – Mathematical model of the anodic oxidation of lead. *J. Electrochem. Soc.*, **141** (9), 2416–2421. doi:10.1149/1.2055135.

18. Knehr K.W., Eng C., Chen-Wiegart Y. chen K., Wang J. & West A.C. (2015). – In situ transmission x-ray microscopy of the lead sulfate film formation on lead in sulfuric acid. *J. Electrochem. Soc.*, **162** (3), A255–A261. doi:10.1149/2.0141503jes.

19. Pavlov D. (2011). – Invention and development of the lead–acid battery. In Lead-Acid Batteries: Science and Technology, Elsevier. pp 3–28.

20. Catherino H.A., Feres F.F. & Trinidad F. (2004). – Sulfation in lead–acid batteries. *J. Power Sources*, **129** (1), 113–120. doi:10.1016/j.jpowsour.2003.11.003.

21. Pavlov D. (2011). – Leady oxide. In Lead-Acid Batteries: Science and Technology, Elsevier. pp 223–250

22. Pavlov D. (2011). – Pastes and grid pasting. In Lead-Acid Batteries: Science and Technology, Elsevier. pp 253–309.

23. Pavlov D. (2011). – Curing of battery plates. In Lead-Acid Batteries: Science and Technology, Elsevier. pp 363–404.

24. Culpin B. (1989). – The role of tetrabasic lead sulphate in the lead/acid positive plate. *J. Power Sources*, **25** (4), 305–311. doi:10.1016/0378-7753(89)85018-9.

25. Biagetti R.V. & Weeks M.C. (1970). – Lead-acid battery: tetrabasic lead sulfate as a paste material for positive plates. *Bell Syst. Tech. J.*, **49** (7), 1305–1319. doi:10.1002/j.1538-7305.1970.tb01829.x.

26. Pavlov D. (2011). – Technology of formation. In Lead-Acid Batteries: Science and Technology (D. Pavlov, ed), Elsevier, Amsterdam. pp 501–531.

27. Ruetschi P. (2003). – Aging mechanisms and service life of lead–acid batteries. *J. Power Sources*, **127** (1–2), 33–44. doi:10.1016/j.jpowsour.2003.09.052.

28. Rüetschi P. & Cahan B.D. (1957). – Anodic corrosion and hydrogen and oxygen overvoltage on lead and lead antimony alloys. *J. Electrochem. Soc.*, **104** (7), 406. doi:10.1149/1.2428614.

29. Rocca E. (1999). – Mechanism of formation of dense anodic films of PbO on lead and lead alloys in sulfuric acid: use of an 18O tracer. *J. Electrochem. Soc.*, **146** (1), 54. doi:10.1149/1.1391564.

30. Ruetschi P., Sklarchuk J. & Angstadt R.T. (1963). – Stability and reactivity of lead oxides. *Electrochimica Acta*, **8** (5), 333–342. doi:10.1016/0013-4686(63)80063-8.

31. Moseley P.T. & Rand D.A.J. (2004). – The valve regulated battery – a paradigm shift in lead-acid technology. In Valve-Regulated Lead–Acid Batteries (D.A.J. Rand, P.T. Moseley, J. Garche & C.D. Parker, eds), Elsevier, The Netherlands. pp 29–42

32. Hollenkamp A.F. (1996). – When is capacity loss in lead/acid batteries "premature"? *J. Power Sources*, **59** (1–2), 87–98. doi:10.1016/0378-7753(96)02306-3.

33. Winsel A., Voss E. & Hullmeine U. (1990). – The aggregate-of-spheres ("Kugelhaufen") model of the PbO2/PbSO4 Electrode. *J. Power Sources*, **30** (1–4), 209–226. doi:10.1016/0378-7753(93)80078-4.

34. Pavlov D. (1995). – A theory of the grid/positive active-mass (PAM) interface and possible methods to improve PAM utilization and cycle life of lead/acid batteries. *J. Power Sources*, **53** (1), 9–21. doi:10.1016/0378-7753(94)02152-S.

35. Dyson I. & Griffin P. (2003). – Development of a valve-regulated lead−acid battery with thin tubular positive plates for improved specific energy and optimization for low charge-factor operation. *J. Power Sources*, **116** (1–2), 263–282. doi:10.1016/S0378-7753(03)00031-4.

36. Pavlov D., Papazov G. & Monahov B. (2003). – Strap grid tubular plate—a new positive plate for lead–acid batteries. *J. Power Sources*, **113** (2), 255–270. doi:10.1016/S0378-7753(02)00521-9.

37. Bui N., Mattesco P., Simon P., Steinmetz J. & Rocca E. (1997). – The tin effect in lead-calcium alloys. *J. Power Sources*, **67** (1–2), 61–67. doi:10.1016/S0378-7753(97)02497-X.

38. Hollenkamp A.F., Constanti K.K., Koop M.J., Apăteanu L., Calabek M. & Micka K. (1994). – Effects of grid alloy on the properties of positive-plate corrosion layers in lead/acid batteries. Implications for premature capacity loss under repetitive deep-discharge cycling service. *J. Power Sources*, **48** (1–2), 195–215.

39. Culpin B., Hollenkamp A.F. & Rand D.A.J. (1992). – The effect of tin on the performance of positive plates in lead/acid batteries. *J. Power Sources*, **38** (1–2), 63–74. doi:10.1016/0378-7753(92)80096-T.

40. Culpin B. & Rand D.A.J. (1991). – Failure modes of lead/acid batteries. *J. Power Sources*, **36** (4), 415–438. doi:10.1016/0378-7753(91)80069-A.

41. Pavlov D. & Pashmakova I. (1987). – Influence of the size of PbSO4 crystals on their solubility and the significance of this process in the lead-acid battery. *J. Appl. Electrochem.*, **17** (5), 1075–1082. doi:10.1007/BF01024373.

42. Iliev V. & Pavlov D. (1982). – Self-discharge and passivation phenomena in lead-acid batteries during storage. *J. Electrochem. Soc.*, **129** (3), 458–464. doi:10.1149/1.2123880.

43. Pavlov D. (1967). – Mechanism of the anodic oxidation of lead in sulphuric acid solutions. *Berichte Bunsenges. Für Phys. Chem.*, **71** (4), 398–404. doi:10.1002/bbpc.19670710412.

44. Pavlov D., Kirchev A., Stoycheva M. & Monahov B. (2004). – Influence of H2SO4 concentration on the mechanism of the processes and on the electrochemical activity of the Pb/PbO2/PbSO4 electrode. *J. Power Sources*, **137** (2), 288–308. doi:10.1016/j.jpowsour.2004.06.006.

45. Karami H., Masoomi B. & Asadi R. (2009). – Recovery of discarded sulfated lead-acid batteries by inverse charge. *Energy Convers. Manag.*, **50** (4), 893–898. doi:10.1016/j.enconman.2009.01.010.

46. Karami H. & Asadi R. (2008). – Recovery of discarded sulfated lead-acid batteries. *J. Power Sources*, **191** (1), 165–175. doi:10.1016/j.jpowsour.2008.12.153.

47. Boden D.P., Arias J. & Fleming F.A. (2001). – The effect of organic expander materials on the performance, life, surface area and crystal structure of negative electrodes in valve regulated cells. *J. Power Sources*, **95** (1–2), 277–292. doi:10.1016/S0378-7753(00)00623-6.

48. Zhang B., Zhong J., Li W., Dai Z., Zhang B. & Cheng Z. (2010). – Transformation of inert PbSO4 deposit on the negative electrode of a lead-acid battery into its active state. *J. Power Sources*, **195** (13), 4338–4343. doi:10.1016/j.jpowsour.2010.01.038.

49. Okuno S. (2006). – Method for removing lead sulfate film formed in lead-acid battery. U.S. Patent and Trademark Office 20060065548, issued Mar. 30, 2006.

50. Yamamoto Y., Matsuoka M., Kimoto M., Uemura M. & Iwakura C. (1995). – Potentiodynamic reactivation of a passivated lead negative electrode in sulphuric acid solution. *Electrochimica Acta*, **41** (3), 439–444. doi:10.1016/0013-4686(95)00317-7.

51. Spanos C., Berlinger S.A., Jayan A. & West A.C. (2016). – Inverse charging techniques for sulfation reversal in flooded lead-acid batteries. *J. Electrochem. Soc.*, **163** (8), A1612–A1618. doi:10.1149/2.0761608jes.

52. Koyama J. (2013). – Protective circuit, battery charger, and power storage device. U.S. Patent and Trademark Office 20130257354, issued Oct. 3, 2013.

53. Boivie H.I. (1997). – Reconditioning lead acid batteries for optional use in a reverse operational mode. U.S. Patent and Trademark Office US005652497A, issued Jul. 29, 1997.

54. Khalil R. (2000). – A study of the effect of inverse charging on the service life of a lead acid battery. *Bull. Electrochem.*, **16** (10), 472–475.

55. Codaro E.N. & Vilche J.R. (1996). – A kinetic study of the electroformation of PbO2 on Pb electrodes in sulphuric acid solutions. *Electrochimica Acta*, **42** (4), 549–555. doi:10.1016/S0013-4686(96)00194-6.

56. Pavlov D. (1968). – Processes of formation of divalent lead oxide compounds on anodic oxidation of lead in sulphuric acid. *Electrochimica Acta*, **13** (10), 2051–2061. doi:10.1016/0013-4686(68)80115-X.

57. Ruetschi P. & Angstadt R.T. (1964). – Anodic oxidation of lead at constant potential. *J. Electrochem. Soc.*, **111** (12), 1323–1330. doi:10.1149/1.2425996.

58. Valeriote E.M.L. & Gallop L.D. (1977). – Low temperature oxidation kinetics of anodic films on lead in sulfuric acid solution. *J. Electrochem. Soc.*, **124** (3), 380–387. doi:10.1149/1.2133309.

59. Pavlov D. & Iordanov N. (1970). – Growth processes of the anodic crystalline layer on potentiostatic oxidation of lead in sulfuric acid. *J. Electrochem. Soc.*, **117** (9), 1103–1109. doi:10.1149/1.2407747.

60. Ruetschi P. (1973). – Ion selectivity and diffusion potentials in corrosion layers: films on Pb. *J. Electrochem. Soc.*, **120** (3), 331–336. doi:10.1149/1.2403449.

61. Lazard (2015). – Lazard's levelized cost of energy storage analysis - version 1.0. Available at: https://www.lazard.com/media/2391/lazards-levelized-cost-of-storage-analysis-10.pdf (accessed on 4 October 2016).

62. Schoenung S. (2011). – *Energy storage systems cost update: a study for the DOE Energy Storage Systems program*. Sandia National Laboratories. Available at: http://prod.sandia.gov/techlib/access-control.cgi/2011/112730.pdf.

63. Zakeri B. & Syri S. (2015). – Electrical energy storage systems: a comparative life cycle cost analysis. *Renew. Sustain. Energy Rev.*, **42**, 569–596. doi:10.1016/j.rser.2014.10.011.

64. Rastler D. (2010). – *Electricity energy storage technology options: a white paper primer on applications, costs, and benefits*. Electric Power Research Institute, Palo Alto, CA. Available at: http://large.stanford.edu/courses/2012/ph240/doshay1/docs/EPRI.pdf (accessed on 30 January 2017).

65. Poonpun P. & Jewell W.T. (2008). – Analysis of the cost per kilowatt hour to store electricity. *IEEE Trans. Energy Convers.*, **23** (2), 529–534. doi:10.1109/TEC.2007.914157.

66. Aburub H. & Jewell W.T. (2013). – Revised analysis of the cost per kilowatt hour to store electricity. *IEEE Trans. Energy Convers.*, **3750** (3750), 3750.

67. Li Y. & Dai H. (2014). – Recent advances in zinc–air batteries. *Chem Soc Rev*, **43** (15), 5257–5275. doi:10.1039/C4CS00015C.

68. Schoenung S.M. & Hassenzahl W.V. (2003). – Long vs. short-term energy storage technologies analysis. a life-cycle cost study. a study for the DOE Energy Storage Systems program. Sandia National Laboratories. Available at: http://infoserve.sandia.gov/sand_doc/2003/032783.pdf (accessed on 4 October 2016).

69. Schoenung S. & Eyer J. (2008). – *Benefit/cost framework for evaluating modular energy storage*. Sandia National Laboratories. Available at: http://prod.sandia.gov/techlib/access-control.cgi/2008/080978.pdf (accessed on 30 January 2017).

70. Concorde Battery Corporation (2014). – Technical manual for chairman series batteries. West Covina, CA 91790. Available at: http://www.concordebattery.com/Chairman_Technical_Manual.pdf (accessed on 27 October 2016).

71. Weber A.Z., Mench M.M., Meyers J.P., Ross P.N., Gostick J.T. & Liu Q. (2011). – Redox flow batteries: a review. *J. Appl. Electrochem.*, **41** (10), 1137–1164. doi:10.1007/s10800-011-0348-2.

72. Yoshio M. & Noguchi H. (2009). – A review of positive electrode materials for lithium-ion batteries. In Lithium-Ion Batteries: Science and Technologies (M. Yoshio, R.J. Brodd & A. Kozawa, eds), Springer New York, New York, NY. pp 9–48.

73. Rushing A.S., Kneifel J.D. & Lippiatt B.L. (2013). – *Energy price indices and discount factors for life-cycle cost analysis: annual supplement to NIST Handbook 135 and NBS Special Publication 709*. National Institute of Standards and Technology. Available at: http://nvlpubs.nist.gov/nistpubs/ir/2013/NIST.IR.85-3273-28.pdf (accessed on 18 October 2016).

74. Liebrich M. (2016). – *Bloomberg New Energy Finance summit: in search of the miraculous*. Market Brief, Bloomberg. Available at: http://www.bbhub.io/bnef/sites/4/2016/04/BNEF-Summit-Keynote-2016.pdf (accessed on 25 January 2017).

75. Nykvist B. & Nilsson M. (2015). – Rapidly falling costs of battery packs for electric vehicles. *Nat. Clim. Change*, **5** (4), 329–332. doi:10.1038/nclimate2564.

76. U.S. Environmental Protection Agency (2016). – EPA battery sizing and cost analysis for future plug-in vehicles: for the midterm evaluation of the 2022-2025 light-duty GHG standards. Available at: https://www.epa.gov/sites/production/files/2016-11/documents/epa-battery-analysis-2016-09-15.pdf (accessed on 25 January 2017).

77. Jülch V. (2016). – Comparison of electricity storage options using levelized cost of storage (LCOS) method. *Appl. Energy*, **183**, 1594–1606. doi:10.1016/j.apenergy.2016.08.165.

78. International Renewable Energy Agency (2015). – Battery storage for renewables: market studies and technology outlook. Available at: http://www.irena.org/documentdownloads/publications/irena_battery_storage_report_2015.pdf.

79. Bullis K. (2013). – Cheap batteries for backup renewable energy: a battery made of cheap materials could store power when it's windy for use when it's not. Available at: https://www.technologyreview.com/s/515076/cheap-batteries-for-backup-renewable-energy/ (accessed on 24 January 2017).

80. Luo X., Wang J., Dooner M. & Clarke J. (2015). – Overview of current development in electrical energy storage technologies and the application potential in power system operation. *Appl. Energy*, **137**, 511–536. doi:10.1016/j.apenergy.2014.09.081.

81. U.S. Department of Energy (2016). – *Hydropower vision: a new chapter for America's 1st renewable electricity source*. Available at: http://energy.gov/eere/water/articles/hydropower-vision-new-chapter-america-s-1st-renewable-electricity-source (accessed on 27 October 2016).

82. Hensley R., Newman J. & Shahinian M. (2012). – *Battery technology charges ahead*. McKinsey & Company. Available at: http://www.alta-energy.com/reports/Battery%20technology%20charges%20ahead%20-%20McKinsey.pdf (accessed on 25 January 2016).

83. Manghani R. (2016). – *U.S. energy storage: 2015 year in review*. Market Brief, Greentech Media Research. Available at: https://votesolar.org/files/7714/6240/1432/Energy-Storage-2015-YIR-Votesolar.pdf (accessed on 25 January 2017).

84. Ortiz L. (2016). – *Grid-scale energy storage balance of systems 2015-2020: architectures, costs and players*. Available at: https://www.greentechmedia.com/research/report/grid-scale-energy-storage-balance-of-systems-2015-2020 (accessed on 30 January 2017).

85. The World Bank Group (2016). – Inflation, GDP deflator (annual %). Available at: http://data.worldbank.org/indicator/NY.GDP.DEFL.KD.ZG?locations=US (accessed on 23 October 2016).

86. U.S. Environmental Protection Agency – Clean Power Plan for existing power plants. Available at: https://www.epa.gov/cleanpowerplan/clean-power-plan-existing-power-plants (accessed on 25 October 2016).

87. Binnie W. (1951). – The crystal structure of lanarkite, PbO.PbSO4. *Acta Crystallogr.*, **4** (5), 471–472. doi:10.1107/S0365110X51001501.

88. Esdaile J.D. (1966). – The lead oxide-lead sulfate system. *J. Electrochem. Soc.*, **113** (1), 71–75. doi:10.1149/1.2423868.

89. Mentzen B.F., Latrach A., Bouix J. & Hewat A.W. (1984). – The crystal structures of PbO.PbXO4 (X = S, Cr, Mo) at 5K by neutron powder profile refinement. *Mater. Res. Bull.*, **19** (5), 549–554. doi:10.1016/0025-5408(84)90121-1.

90. Steele I.M. & Pluth J.J. (1998). – Crystal Structure of tetrabasic lead sulfate (4PbO · PbSO4): an intermediate phase in the production of lead-acid batteries. *J. Electrochem. Soc.*, **145** (2), 528–533. doi:10.1149/1.1838298.

91. Steele I.M., Pluth J.J. & Richardson Jr J.W. (1997). – Crystal structure of tribasic lead sulfate (3PbO·PbSO4·H2O) by x-rays and neutrons: an intermediate phase in the production of lead-acid batteries. *J. Solid State Chem.*, **132** (1), 173–181. doi:10.1006/jssc.1997.7440.

92. Böhnstedt W. (1996). – Automotive lead/acid battery separators: a global overview. *J. Power Sources*, **59** (1–2), 45–50. doi:10.1016/0378-7753(95)02299-6.

93. Endoh H. (1996). – Separators for automotive lead/acid batteries: selection of suitable types for different climate zones. *J. Power Sources*, **59** (1–2), 51–55. doi:10.1016/0378-7753(95)02300-3.

94. Thele M., Karden E., Surewaard E. & Sauer D.U. (2006). – Impedance-based overcharging and gassing model for VRLA/AGM batteries. *J. Power Sources*, **158** (2), 953–963. doi:10.1016/j.jpowsour.2005.11.025.

95. Macdonald J.R. & Johnson W.B. (2005). – Fundamentals of impedance spectroscopy. In Impedance Spectroscopy (E. Barsoukov & J.R. Macdonald, eds), John Wiley & Sons, Inc., Hoboken, NJ, USA. pp 1–26.

96. Pavlov D. & Popova R. (1970). – Mechanism of passivation processes of the lead sulphate electrode. *Electrochimica Acta*, **15** (9), 1483–1491. doi:10.1016/0013-4686(70)80069-X.

97. Prengaman R.D. (2004). – Lead alloys for valve-regulated lead-acid batteries. In Valve-Regulated Lead–Acid Batteries (D.A.J. Rand, P.T. Moseley, J. Garche & C.D. Parker, eds), Elsevier, The Netherlands. pp 43–63.

98. Bullock K.R. & Dayton T.C. (2004). – Positive-plate additives to enhance formation and battery performance. In Valve-Regulated Lead–Acid Batteries (D.A.J. Rand, P.T. Moseley, J. Garche & C.D. Parker, eds), Elsevier, The Netherlands. pp 137–162.

99. Pourbaix M. (1974). – Atlas of electrochemical equilibria in aqueous solutions. National Association of Corrosion Engineers.

100. Dimitrov M., Pavlov D., Rogachev T., Matrakova M. & Bogdanova L. (2005). – Processes taking place in the paste of lead-acid battery plates during soaking prior to formation and their influence on battery performance. *J. Power Sources*, **140** (1), 168–180. doi:10.1016/j.jpowsour.2004.08.006.

101. Laruelle S., Grugeon-Dewaele S., Torcheux L. & Delahaye-Vidal A. (1999). – The curing reaction study of the active material in the lead-acid battery. *J. Power Sources*, **77** (1), 83–89. doi:10.1016/S0378-7753(98)00187-6.

102. Torcheux L., Vaurijoux J.P. & Guibert A. de (1997). – Improvement of the formation efficiency of the tetrabasic lead sulfate for lead/acid batteries. *J. Power Sources*, **64** (1–2), 81–89. doi:10.1016/S0378-7753(96)02506-2.

103. Pavlov D. & Bashtavelova E. (1990). – A study of the oxidation of 4PbO·PbSO4 crystals in cured paste to PbO2 agglomerates during formation of positive plates for lead/acid batteries. *J. Power Sources*, **31** (1–4), 243–254. doi:10.1016/0378-7753(90)80076-P.

104. Pavlov D. & Papazov G. (1976). – Dependence of the properties of the lead-acid battery positive plate paste on the processes occurring during its production. *J. Appl. Electrochem.*, **6** (4), 339–345. doi:10.1007/BF00608919.

105. Pavlov D. & Kapkov N. (1990). – Lead-acid battery pastes containing 4PbO·PbSO4 and Pb3O4. *J. Electrochem. Soc.*, **137** (1), 16–21. doi:10.1149/1.2086354.

106. Boggio A., Maja M. & Penazzi N. (1983). – Effects of antimony on the electrochemical behaviour of lead dioxide in sulphuric acid. *J. Power Sources*, **9** (2), 221–230. doi:10.1016/0378-7753(83)80034-2.

107. Dawson J.L., Wilkinson J. & Gillibrand M.I. (1970). – Antimony species in aqueous sulphuric acid solutions. *J. Inorg. Nucl. Chem.*, **32** (2), 501–517. doi:10.1016/0022-1902(70)80259-7.

108. Laitinen L., Revitzer H., Sundholm G., Vilhunen J.K., Pavlov D. & Bojinov M. (1991). – Electrochemical behaviour of the antimony electrode in sulphuric acid solutions—III. identification of corrosion products after long-term polarization. *Electrochimica Acta*, **36** (14), 2093–2102. doi:10.1016/0013-4686(91)85215-S.

109. Kono M., Igarashi H. & Kishimoto K. (1980). – Glass fiber separator for storage batteries. U.S. Patent and Trademark Office 4216280A, issued Aug. 5, 1980.

110. Burbank J. (1966). – Anodic oxidation of the basic sulfates of lead. *J. Electrochem. Soc.*, **113** (1), 10. doi:10.1149/1.2423844.

111. Humphreys M.E.D., Taylor R. & Barnes S.C. (1970). – The curing of lead-acid battery plates. In Research and Development in Non-Mechanical Electrical Power Sources, Elsevier. pp 55–67.

112. Pavlov D. (1986). – Structural properties of the PbO2 active mass determining its capacity and the "breathing" of the positive plate during cycling. *J. Electrochem. Soc.*, **133** (2), 241. doi:10.1149/1.2108555.

113. Pavlov D. & Ignatova S. (1987). – Breathing of the lead-acid battery negative plate during cycling. *J. Appl. Electrochem.*, **17** (4), 715–723. doi:10.1007/BF01007806.

114. Meissner E. (1999). – How to understand the reversible capacity decay of the lead dioxide electrode. *J. Power Sources*, **78** (1–2), 99–114. doi:10.1016/S0378-7753(99)00019-1.

115. Iliev V. & Pavlov D. (1985). – The effect of the expander upon the two types of negative active mass structure in lead-acid batteries. *J. Appl. Electrochem.*, **15** (1), 39–52. doi:10.1007/BF00617739.

116. Lam L.T., Ozgun H., Lim O.V., Hamilton J.A., Vu L.H., Vella D.G. & Rand D.A.J. (1995). – Pulsed-current charging of lead/acid batteries — a possible means for overcoming premature capacity loss? *J. Power Sources*, **53** (2), 215–228. doi:10.1016/0378-7753(94)01988-8.

117. Lam L.T., Vecchio-Sadus A.M., Ozgun H. & Rand D.A.J. (1992). – Conversion of tetrabasic lead sulfate to lead dioxide in lead/acid battery plates. *J. Power Sources*, **38** (1–2), 87–102. doi:10.1016/0378-7753(92)80098-V.

118. Appel P.W. & Edwards D.B. (1995). – Capacity predictions for lead/acid battery plates having conductive additives. *J. Power Sources*, **55** (1), 81–85. doi:10.1016/0378-7753(94)02176-4.

119. Pavlov D. (1992). – The PbO2 particle: exchange reactions between ions of the electrolyte and the PbO2 particles of the lead-acid battery positive active mass. *J. Electrochem. Soc.*, **139** (7), 1830. doi:10.1149/1.2069506.

120. Guo Y. (2005). – Investigation of active mass utilization of positive plate in automotive lead-acid batteries. *J. Electrochem. Soc.*, **152** (6), A1136. doi:10.1149/1.1914749.

121. Papazov G. & Pavlov D. (1996). – Influence of cycling current and power profiles on the cycle life of lead/acid batteries. *J. Power Sources*, **62** (2), 193–199. doi:10.1016/S0378-7753(96)02422-6.

122. Eisenhut N.R. & Kseniak E.M. (1991). – Formation of wrought lead-calcium batteries for consistency. *J. Power Sources*, **33** (1–4), 77–85. doi:10.1016/0378-7753(91)85050-7.

123. Manders J.E., Lam L.T., Peters K., Prengaman R.D. & Valeriote E.M. (1996). – Lead/acid battery technology. *J. Power Sources*, **59** (1–2), 199–207. doi:10.1016/0378-7753(96)02323-3.

124. Monahov B. (1994). – Influence of antimony on the structure and the degree of hydration of the anodic PbO2 layer formed on Pb-Sb electrodes. *J. Electrochem. Soc.*, **141** (9), 2316. doi:10.1149/1.2055119.

125. Mindt W. (1969). – Electrical properties of electrodeposited PbO2 films. *J. Electrochem. Soc.*, **116** (8), 1076. doi:10.1149/1.2412217.

126. Pavlov D. (1980). – Zone processes at the formation of the lead acid battery positive plate. *J. Electrochem. Soc.*, **127** (10), 2104. doi:10.1149/1.2129355.

127. Hampson N.A., Kelly S., Peters K. & Whyatt P. (1980). – Morphological examination of the effect of antimony on the electrochemistry of lead. *J. Appl. Electrochem.*, **10** (5), 597–602. doi:10.1007/BF00615482.

128. Pavlov D., Dakhouche A. & Rogachev T. (1990). – Influence of arsenic, antimony and bismuth on the properties of lead/acid battery positive plates. *J. Power Sources*, **30** (1–4), 117–129. doi:10.1016/0378-7753(93)80068-Z.

129. Pavlov D. (1991). – Effect of dopants (Group Va) on the performance of the positive lead/acid battery plate. *J. Power Sources*, **33** (1–4), 221–229. doi:10.1016/0378-7753(91)85061-Z.

130. Pavlov D. (1992). – The lead-acid battery lead dioxide active mass: a gel-crystal system with proton and electron conductivity. *J. Electrochem. Soc.*, **139** (11), 3075. doi:10.1149/1.2069034.

131. Boden D.P., Loosemore D.V., Spence M.A. & Wojcinski T.D. (2010). – Optimization studies of carbon additives to negative active material for the purpose of extending the life of VRLA batteries in high-rate partial-state-of-charge operation. *J. Power Sources*, **195** (14), 4470–4493. doi:10.1016/j.jpowsour.2009.12.069.

132. Dodson V.H. (1961). – Some important factors that influence the composition of the positive plate material in the lead-acid battery. *J. Electrochem. Soc.*, **108** (5), 401. doi:10.1149/1.2428100.

133. Pavlov D. (1995). – The effect of selenium on the electrochemical behavior and corrosion of Pb-Sn alloys used in lead-acid batteries. *J. Electrochem. Soc.*, **142** (9), 2919. doi:10.1149/1.2048666.

134. Pavlov D. (2011). – H2SO4 electrolyte – an active material in the lead–acid cell. In Lead-Acid Batteries: Science and Technology, Elsevier. pp 117–148.

135. Saakes M., J. Van Duin P., C.P. Ligtvoet A. & Schmal D. (1994). – Investigations of the negative plate of lead/acid cells 1. Selection of additives. *J. Power Sources*, **47** (1–2), 129–147. doi:10.1016/0378-7753(94)80056-1.

# Appendix A – Model data and results for chapter 2

**Table A-1:** LCOE model and data for a transmission system, 20 yr life, 8 h discharge, 1 cycle/day, 300 days/yr

| Transmission | | | | | | | | | | | | | | | | | | | | | |
|---|---|---|---|---|---|---|---|---|---|---|---|---|---|---|---|---|---|---|---|---|---|
| | Units | PbA | | PbA (5-yr) | | ALAB | | ALAB (5-yr) | | Li-Ion | | Li-Ion (5-yr) | | NaS | | NaS (5-yr) | |
| Power Rating | MW | 100 | 100 | 100 | 100 | 100 | 100 | 100 | 100 | 100 | 100 | 100 | 100 | 100 | 100 | 100 | 100 |
| Duration | Hours | 8 | 8 | 8 | 8 | 8 | 8 | 8 | 8 | 8 | 8 | 8 | 8 | 8 | 8 | 8 | 8 |
| Cycle Life | Cycles | 1500 | 250 | 1500 | 250 | 4500 | 2000 | 4500 | 2000 | 5000 | 1000 | 5000 | 1000 | 5000 | 4000 | 5000 | 4000 |
| Usable Energy | MWh | 800 | 800 | 800 | 800 | 800 | 800 | 800 | 800 | 800 | 800 | 800 | 800 | 800 | 800 | 800 | 800 |
| 100% Depth of Discharge Cycles/Day | | 1 | 1 | 1 | 1 | 1 | 1 | 1 | 1 | 1 | 1 | 1 | 1 | 1 | 1 | 1 | 1 |
| $f_{SoC}$ | | 1 | 1 | 1 | 1 | 1 | 1 | 1 | 1 | 1 | 1 | 1 | 1 | 1 | 1 | 1 | 1 |
| Operating Days/Year | | 300 | 300 | 300 | 300 | 300 | 300 | 300 | 300 | 300 | 300 | 300 | 300 | 300 | 300 | 300 | 300 |
| Operating Hours/Year | | 2400 | 2400 | 2400 | 2400 | 2400 | 2400 | 2400 | 2400 | 2400 | 2400 | 2400 | 2400 | 2400 | 2400 | 2400 | 2400 |
| Project Life | Years | 20 | 20 | 20 | 20 | 20 | 20 | 20 | 20 | 20 | 20 | 20 | 20 | 20 | 20 | 20 | 20 |
| Annual Used Energy | MWh | 240000 | 240000 | 240000 | 240000 | 240000 | 240000 | 240000 | 240000 | 240000 | 240000 | 240000 | 240000 | 240000 | 240000 | 240000 | 240000 |
| Project Used Energy | MWh | 4800000 | 4800000 | 4800000 | 4800000 | 4800000 | 4800000 | 4800000 | 4800000 | 4800000 | 4800000 | 4800000 | 4800000 | 4800000 | 4800000 | 4800000 | 4800000 |
| Initial Capital Cost - DC | $/kWh | 150 | 200 | 114 | 152 | 200 | 330 | 152 | 250.8 | 300 | 500 | 159 | 265 | 350 | 450 | 350 | 450 |
| Initial Capital Cost - AC | $/kW | 450 | 650 | 265.5 | 383.5 | 450 | 650 | 265.5 | 383.5 | 450 | 650 | 265.5 | 383.5 | 450 | 650 | 265.5 | 383.5 |
| Total Initial Installed Cost | $/kW | 1650 | 2250 | 1177.5 | 1599.5 | 2050 | 3290 | 1481.5 | 2389.9 | 2850 | 4650 | 1537.5 | 2503.5 | 3250 | 4250 | 3065.5 | 3983.5 |
| Replacement Cost - DC | $/kWh | 150 | 200 | 114 | 152 | 200 | 330 | 152 | 250.8 | 300 | 500 | 159 | 265 | 350 | 450 | 350 | 450 |
| Replacement Period | Years | 5.00 | 0.83 | 5.00 | 0.83 | 15.00 | 6.67 | 15.00 | 6.67 | 16.67 | 3.33 | 16.67 | 3.33 | 16.67 | 13.33 | 16.67 | 13.33 |
| O&M % of CAPEX | % | 2.0% | 2.5% | 2.0% | 2.5% | 2.0% | 2.5% | 2.0% | 2.5% | 1.5% | 2.0% | 1.5% | 2.0% | 2.0% | 2.0% | 2.0% | 2.0% |
| O&M Cost | $/kW-year | 33 | 56.25 | 23.55 | 39.9875 | 41 | 82.25 | 29.63 | 59.7475 | 42.75 | 93 | 23.0625 | 50.07 | 65 | 85 | 61.31 | 79.67 |
| Charging Cost | $/MWh | 50 | 50 | 50 | 50 | 50 | 50 | 50 | 50 | 50 | 50 | 50 | 50 | 50 | 50 | 50 | 50 |
| Annual Cost Escalator | % | 1.5% | 1.5% | 1.5% | 1.5% | 1.5% | 1.5% | 1.5% | 1.5% | 1.5% | 1.5% | 1.5% | 1.5% | 1.5% | 1.5% | 1.5% | 1.5% |
| Efficiency | | 80% | 75% | 80% | 75% | 80% | 75% | 80% | 75% | 90% | 85% | 90% | 85% | 85% | 75% | 85% | 75% |
| Levelized Cost of Storage | $/kW-year | 509 | 2650 | 390 | 2013 | 415 | 859 | 319 | 651 | 528 | 1919 | 309 | 1049 | 616 | 830 | 589 | 791 |
| Levelized Cost of Storage D | $/MWh | 212 | 1104 | 163 | 839 | 173 | 358 | 133 | 271 | 220 | 799 | 129 | 437 | 257 | 346 | 246 | 330 |

| Transmission (continued) | | | | | | | | | | | | | | | | | | | | | |
|---|---|---|---|---|---|---|---|---|---|---|---|---|---|---|---|---|---|---|---|---|---|
| | Units | Flow | | Flow (5-yr) | | Zn-Hyb | | Zn-Hyb (5-yr) | | PHS | | CAES | |
| Power Rating | MW | 100 | 100 | 100 | 100 | 100 | 100 | 100 | 100 | 100 | 100 | 100 | 100 |
| Duration | Hours | 8 | 8 | 8 | 8 | 8 | 8 | 8 | 8 | 8 | 8 | 8 | 8 |
| Cycle Life | Cycles | 10000 | 5000 | 10000 | 5000 | 2500 | 2000 | 2500 | 2000 | 50000 | 20000 | 13000 | 13000 |
| Usable Energy | MWh | 800 | 800 | 800 | 800 | 800 | 800 | 800 | 800 | 800 | 800 | 800 | 800 |
| 100% Depth of Discharge Cycles/Day | | 1 | 1 | 1 | 1 | 1 | 1 | 1 | 1 | 1 | 1 | 1 | 1 |
| fSoC | | 1 | 1 | 1 | 1 | 1 | 1 | 1 | 1 | 1 | 1 | 1 | 1 |
| Operating Days/Year | | 300 | 300 | 300 | 300 | 300 | 300 | 300 | 300 | 300 | 300 | 300 | 300 |
| Operating Hours/Year | | 2400 | 2400 | 2400 | 2400 | 2400 | 2400 | 2400 | 2400 | 2400 | 2400 | 2400 | 2400 |
| Project Life | Years | 20 | 20 | 20 | 20 | 20 | 20 | 20 | 20 | 20 | 20 | 20 | 20 |
| Annual Used Energy | MWh | 240000 | 240000 | 240000 | 240000 | 240000 | 240000 | 240000 | 240000 | 240000 | 240000 | 240000 | 240000 |
| Project Used Energy | MWh | 4800000 | 4800000 | 4800000 | 4800000 | 4800000 | 4800000 | 4800000 | 4800000 | 4800000 | 4800000 | 4800000 | 4800000 |
| Initial Capital Cost - DC | $/kWh | 210 | 367 | 130.2 | 227.54 | 160 | 300 | 152 | 285 | 0 | 0 | 0 | 0 |
| Initial Capital Cost - AC | $/kW | 1100 | 1181 | 649 | 696.79 | 450 | 650 | 265.5 | 383.5 | 1500 | 3000 | 1000 | 2000 |
| Total Initial Installed Cost | $/kW | 2780 | 4117 | 1690.6 | 2517.11 | 1730 | 3050 | 1481.5 | 2663.5 | 1500 | 3000 | 1000 | 2000 |
| Replacement Cost - DC | $/kWh | 210 | 367 | 130.2 | 227.54 | 160 | 300 | 152 | 285 | 0 | 0 | 0 | 0 |
| Replacement Period | Years | - | 16.67 | - | 16.67 | 8.33 | 6.67 | 8.33 | 6.67 | - | - | - | - |
| O&M % of CAPEX | % | 2.0% | 3.0% | 2.0% | 3.0% | 1.0% | 2.0% | 1.0% | 2.0% | 1.0% | 3.0% | 2.0% | 2.0% |
| O&M Cost | $/kW-year | 55.6 | 123.51 | 33.812 | 75.5133 | 17.3 | 61 | 14.815 | 53.27 | 15 | 90 | 20 | 40 |
| Charging Cost | $/MWh | 50 | 50 | 50 | 50 | 50 | 50 | 50 | 50 | 50 | 50 | 50 | 50 |
| Annual Cost Escalator | % | 1.5% | 1.5% | 1.5% | 1.5% | 1.5% | 1.5% | 1.5% | 1.5% | 1.5% | 1.5% | 1.5% | 1.5% |
| Efficiency | | 75% | 65% | 75% | 65% | 75% | 60% | 75% | 60% | 82% | 70% | 55% | 70% |
| Levelized Cost of Storage | $/kW-year | 465 | 804 | 308 | 521 | 419 | 796 | 380 | 726 | 260 | 531 | 259 | 357 |
| Levelized Cost of Storage D | $/MWh | 194 | 335 | 128 | 217 | 175 | 332 | 158 | 303 | 108 | 221 | 108 | 149 |

**Table A-2:** LCOE results for a transmission system, 20 yr life, 8 h discharge, 1 cycle/day, 300 days/yr

| Transmission LCOE Data ($/MWh) | | | | | | | | | | | | | | | | | | | | | | | |
|---|---|---|---|---|---|---|---|---|---|---|---|---|---|---|---|---|---|---|---|---|---|---|---|
| | Units | PbA | | | PbA (5-yr) | | | ALAB | | | ALAB (5-yr) | | | Li-Ion | | | Li-Ion (5-yr) | | | NaS | | | NaS (5-yr) | | |
| Capital Cost | $/MWh | 72 | - | 98 | 51 | - | 70 | 90 | - | 144 | 65 | - | 104 | 125 | - | 203 | 67 | - | 109 | 142 | - | 186 | 134 | - | 174 |
| Charging | $/MWh | 25 | - | 27 | 25 | - | 27 | 25 | - | 27 | 25 | - | 27 | 22 | - | 24 | 22 | - | 24 | 24 | - | 27 | 24 | - | 27 |
| O&M | $/MWh | 14 | - | 23 | 10 | - | 17 | 17 | - | 34 | 12 | - | 25 | 18 | - | 39 | 10 | - | 21 | 27 | - | 35 | 26 | - | 33 |
| Replacement | $/MWh | 74 | - | 792 | 56 | - | 602 | 21 | - | 107 | 16 | - | 81 | 27 | - | 419 | 15 | - | 222 | 32 | - | 54 | 32 | - | 54 |
| Taxes | $/MWh | 27 | - | 164 | 20 | - | 124 | 20 | - | 46 | 15 | - | 34 | 28 | - | 115 | 15 | - | 61 | 32 | - | 44 | 31 | - | 42 |
| Total | $/MWh | 212 | - | 1104 | 163 | - | 839 | 173 | - | 358 | 133 | - | 271 | 220 | - | 799 | 129 | - | 437 | 257 | - | 346 | 246 | - | 330 |

| | | Flow | | | Flow (5-yr) | | | Zn-Hyb | | | Zn-Hyb (5-yr) | | | PHS | | | CAES | | |
|---|---|---|---|---|---|---|---|---|---|---|---|---|---|---|---|---|---|---|---|
| Capital Cost | $/MWh | 121 | - | 180 | 74 | - | 110 | 76 | - | 133 | 65 | - | 116 | 66 | - | 131 | 44 | - | 87 |
| Charging | $/MWh | 27 | - | 31 | 27 | - | 31 | 27 | - | 33 | 27 | - | 33 | 24 | - | 29 | 48 | - | 29 |
| O&M | $/MWh | 23 | - | 51 | 14 | - | 31 | 7 | - | 25 | 6 | - | 22 | 6 | - | 38 | 8 | - | 17 |
| Replacement | $/MWh | 0 | - | 33 | 0 | - | 21 | 43 | - | 97 | 41 | - | 92 | 0 | - | 0 | 0 | - | 0 |
| Taxes | $/MWh | 22 | - | 39 | 14 | - | 24 | 22 | - | 43 | 20 | - | 39 | 12 | - | 24 | 8 | - | 16 |
| Total | $/MWh | 194 | - | 335 | 128 | - | 217 | 175 | - | 332 | 158 | - | 303 | 108 | - | 221 | 108 | - | 149 |

**Table A-3:** LCOE model and data for frequency regulation, 20 yr life, 0.5 h discharge, 4.8 cycles/day, 350 days/yr.

| | | Frequency Regulation | | | | | | | | | | | | | | | | | | | | | |
|---|---|---|---|---|---|---|---|---|---|---|---|---|---|---|---|---|---|---|---|---|---|---|---|
| | **Units** | **ALAB** | | | **ALAB (5-yr)** | | | **Li-Ion** | | | **Li-Ion (5-yr)** | | | **Flywheel** | | | **Flywheel (5-yr)** | | | | | | |
| Power Rating | MW | 10 | - | 10 | 10 | - | 10 | 10 | - | 10 | 10 | - | 10 | 10 | - | 10 | 10 | - | 10 | | | | |
| Duration | Hours | 0.5 | - | 0.5 | 0.5 | - | 0.5 | 0.5 | - | 0.5 | 0.5 | - | 0.5 | 0.5 | - | 0.5 | 0.5 | - | 0.5 | | | | |
| Cycle Life | Cycles | 9000 | - | 4000 | 9000 | - | 4000 | 6250 | - | 1250 | 6250 | - | 1250 | 20000 | - | 20000 | 20000 | - | 20000 | | | | |
| Usable Energy | MWh | 5 | - | 5 | 5 | - | 5 | 5 | - | 5 | 5 | - | 5 | 5 | - | 5 | 5 | - | 5 | | | | |
| 100% Depth of Discharge Cycles/Day | | 2.4 | - | 2.4 | 2.4 | - | 2.4 | 3.84 | - | 3.84 | 3.84 | - | 3.84 | 4.8 | - | 4.8 | 4.8 | - | 4.8 | | | | |
| fSoC | | 0.5 | - | 0.5 | 0.5 | - | 0.5 | 0.8 | - | 0.8 | 0.8 | - | 0.8 | 1 | - | 1 | 1 | - | 1 | | | | |
| Operating Days/Year | | 350 | - | 350 | 350 | - | 350 | 350 | - | 350 | 350 | - | 350 | 350 | - | 350 | 350 | - | 350 | | | | |
| Operating Hours/Year | | 840 | - | 840 | 840 | - | 840 | 840 | - | 840 | 840 | - | 840 | 840 | - | 840 | 840 | - | 840 | | | | |
| Project Life | Years | 20 | - | 20 | 20 | - | 20 | 20 | - | 20 | 20 | - | 20 | 20 | - | 20 | 20 | - | 20 | | | | |
| Annual Used Energy | MWh | 8400 | - | 8400 | 8400 | - | 8400 | 8400 | - | 8400 | 8400 | - | 8400 | 8400 | - | 8400 | 8400 | - | 8400 | | | | |
| Project Used Energy | MWh | 168000 | - | 168000 | 168000 | - | 168000 | 168000 | - | 168000 | 168000 | - | 168000 | 168000 | - | 168000 | 168000 | - | 168000 | | | | |
| Initial Capital Cost - DC | $/kWh | 200 | - | 330 | 152 | - | 250.8 | 300 | - | 500 | 159 | - | 265 | 1400 | - | 4000 | 1260 | - | 3600 | | | | |
| Initial Capital Cost - AC | $/kW | 450 | - | 650 | 265.5 | - | 383.5 | 450 | - | 650 | 265.5 | - | 383.5 | 450 | - | 650 | 265.5 | - | 383.5 | | | | |
| Total Initial Installed Cost | $/kW | 650 | - | 980 | 417.5 | - | 634.3 | 637.5 | - | 962.5 | 364.875 | - | 549.125 | 1150 | - | 2650 | 805.95 | - | 1965.15 | | | | |
| Replacement Cost - DC | $/kWh | 200 | - | 330 | 152 | - | 250.8 | 300 | - | 500 | 159 | - | 265 | 1400 | - | 4000 | 1260 | - | 3600 | | | | |
| Replacement Period | Years | - | - | 11.43 | - | - | 11.43 | 17.86 | - | 3.57 | 17.86 | - | 3.57 | - | - | - | - | - | - | | | | |
| O&M % of CAPEX | % | 2.0% | - | 2.5% | 2.0% | - | 2.5% | 1.5% | - | 2.0% | 1.5% | - | 2.0% | 1.5% | - | 1.5% | 1.5% | - | 1.5% | | | | |
| O&M Cost | $/kW-year | 13 | - | 25 | 8 | - | 16 | 10 | - | 19 | 5 | - | 11 | 17 | - | 40 | 12 | - | 29 | | | | |
| Charging Cost | $/MWh | 66 | - | 66 | 66 | - | 66 | 66 | - | 66 | 66 | - | 66 | 66 | - | 66 | 66 | - | 66 | | | | |
| Annual Cost Escalator | % | 1.5% | - | 1.5% | 1.5% | - | 1.5% | 1.5% | - | 1.5% | 1.5% | - | 1.5% | 1.5% | - | 1.5% | 1.5% | - | 1.5% | | | | |
| Efficiency | | 80% | - | 75% | 80% | - | 75% | 90% | - | 85% | 90% | - | 85% | 93% | - | 95% | 93% | - | 95% | | | | |
| Levelized Cost of Storage | $/kW-year | 173 | - | 247 | 140 | - | 192 | 165 | | 302 | 124 | - | 201 | 228 | | 436 | 180 | - | 340 | | | | |
| Levelized Cost of Storage D | $/MWh | 206 | - | 294 | 166 | - | 228 | 196 | | 360 | 148 | - | 239 | 272 | | 519 | 215 | - | 405 | | | | |

**Table A-4:** LCOE results for frequency regulation, 20 yr life, 0.5 h discharge, 4.8 cycles/day, 350 days/yr

| | | Frequency Regulation LCOE Data ($/MWh) | | | | | | | | | | | | | | | | | | | | | |
|---|---|---|---|---|---|---|---|---|---|---|---|---|---|---|---|---|---|---|---|---|---|---|---|
| | **Units** | **ALAB** | | | **ALAB (5-yr)** | | | **Li-Ion** | | | **Li-Ion (5-yr)** | | | **Flywheel** | | | **Flywheel (5-yr)** | | | | | | |
| **Capital Cost** | $/MWh | 81 | - | 122 | 52 | - | 79 | 80 | - | 120 | 46 | - | 69 | 144 | - | 331 | 101 | - | 245 | | | | |
| **Charging** | $/MWh | 94 | - | 101 | 94 | - | 101 | 84 | - | 89 | 84 | - | 89 | 81 | - | 80 | 81 | - | 80 | | | | |
| **O&M** | $/MWh | 15 | - | 29 | 10 | - | 19 | 11 | - | 23 | 7 | - | 13 | 21 | - | 47 | 14 | - | 35 | | | | |
| **Replacement** | $/MWh | 0 | - | 16 | 0 | - | 12 | 6 | - | 89 | 3 | - | 47 | 0 | - | 0 | 0 | - | 0 | | | | |
| **Taxes** | $/MWh | 15 | - | 26 | 10 | - | 17 | 16 | - | 39 | 9 | - | 21 | 27 | - | 61 | 19 | - | 45 | | | | |
| **Total** | $/MWh | 206 | - | 294 | 166 | - | 228 | 196 | - | 360 | 148 | - | 239 | 272 | - | 519 | 215 | - | 405 | | | | |

**Table A-5:** LCOE model and data for PV integration, 20 yr life, 2 h discharge, 1.25 cycles/day, 350 days/year.

| | | PV Integration | | | | | | | | | | | | | | | | | | | | | |
|---|---|---|---|---|---|---|---|---|---|---|---|---|---|---|---|---|---|---|---|---|---|---|---|
| | Units | PbA | | | PbA (5-yr) | | | ALAB | | | ALAB (5-yr) | | | Li-Ion | | | Li-Ion (5-yr) | | |
| Power Rating | MW | 2 | - | 2 | 2 | - | 2 | 2 | - | 2 | 2 | - | 2 | 2 | - | 2 | 2 | - | 2 |
| Duration | Hours | 2 | - | 2 | 2 | - | 2 | 2 | - | 2 | 2 | - | 2 | 2 | - | 2 | 2 | - | 2 |
| Cycle Life | Cycles | 1923 | - | 321 | 1923 | - | 321 | 5769 | - | 2564 | 5769 | - | 2564 | 5263 | - | 1053 | 5263 | - | 1053 |
| Usable Energy | MWh | 4 | - | 4 | 4 | - | 4 | 4 | - | 4 | 4 | - | 4 | 4 | - | 4 | 4 | - | 4 |
| 100% Depth of Discharge Cycles/Day | | 0.975 | - | 0.975 | 0.975 | - | 0.975 | 0.975 | - | 0.975 | 0.975 | - | 0.975 | 1.1875 | - | 1.1875 | 1.1875 | - | 1.1875 |
| fSoC | | 0.78 | - | 0.78 | 0.78 | - | 0.78 | 0.78 | - | 0.78 | 0.78 | - | 0.78 | 0.95 | - | 0.95 | 0.95 | - | 0.95 |
| Operating Days/Year | | 350 | - | 350 | 350 | - | 350 | 350 | - | 350 | 350 | - | 350 | 350 | - | 350 | 350 | - | 350 |
| Operating Hours/Year | | 875 | - | 875 | 875 | - | 875 | 875 | - | 875 | 875 | - | 875 | 875 | - | 875 | 875 | - | 875 |
| Project Life | Years | 20 | - | 20 | 20 | - | 20 | 20 | - | 20 | 20 | - | 20 | 20 | - | 20 | 20 | - | 20 |
| Annual Used Energy | MWh | 1750 | - | 1750 | 1750 | - | 1750 | 1750 | - | 1750 | 1750 | - | 1750 | 1750 | - | 1750 | 1750 | - | 1750 |
| Project Used Energy | MWh | 35000 | - | 35000 | 35000 | - | 35000 | 35000 | - | 35000 | 35000 | - | 35000 | 35000 | - | 35000 | 35000 | - | 35000 |
| Initial Capital Cost - DC | $/kWh | 150 | - | 200 | 114 | - | 152 | 200 | - | 330 | 152 | - | 250.8 | 300 | - | 500 | 159 | - | 265 |
| Initial Capital Cost - AC | $/kW | 450 | - | 650 | 265.5 | - | 383.5 | 450 | - | 650 | 265.5 | - | 383.5 | 450 | - | 650 | 265.5 | - | 383.5 |
| Total Initial Installed Cost | $/kW | 834.6 | - | 1162.8 | 557.8 | - | 773.2 | 962.8 | - | 1496.2 | 655.2 | - | 1026.6 | 1081.6 | - | 1702.6 | 600.2 | - | 941.4 |
| Replacement Cost - DC | $/kWh | 150 | - | 200 | 114 | - | 152 | 200 | - | 330 | 152 | - | 250.8 | 300 | - | 500 | 159 | - | 265 |
| Replacement Period | Years | 5.49 | | 0.92 | 5.49 | - | 0.92 | 16.48 | | 7.33 | 16.48 | - | 7.33 | 15.04 | | 3.01 | 15.04 | - | 3.01 |
| O&M % of CAPEX | % | 2.0% | - | 2.5% | 2.0% | - | 2.5% | 2.0% | - | 2.5% | 2.0% | - | 2.5% | 1.5% | - | 2.0% | 1.5% | - | 2.0% |
| O&M Cost | $/kW-year | 17 | - | 29 | 11 | - | 19 | 19 | - | 37 | 13 | - | 26 | 16 | - | 34 | 9 | - | 19 |
| Charging Cost | $/MWh | 58 | - | 58 | 58 | - | 58 | 58 | - | 58 | 58 | - | 58 | 58 | - | 58 | 58 | - | 58 |
| Annual Cost Escalator | % | 0.0% | - | 0.0% | 0.0% | - | 0.0% | 0.0% | - | 0.0% | 0.0% | - | 0.0% | 0.0% | - | 0.0% | 0.0% | - | 0.0% |
| Efficiency | | 80% | - | 75% | 80% | - | 75% | 80% | - | 75% | 80% | - | 75% | 90% | - | 85% | 90% | - | 85% |
| Levelized Cost of Storage | $/kW-year | 246 | - | 895 | 191 | - | 680 | 218 | - | 380 | 170 | - | 288 | 229 | - | 670 | 151 | - | 388 |
| Levelized Cost of Storage D | $/MWh | 281 | - | 1023 | 218 | - | 777 | 249 | - | 435 | 194 | - | 330 | 262 | - | 765 | 173 | - | 443 |

| | | PV Integration (Continued) | | | | | | | | | | | | | | | | | | | | | |
|---|---|---|---|---|---|---|---|---|---|---|---|---|---|---|---|---|---|---|---|---|---|---|---|
| | Units | NaS (5-yr) | | | NaS (5-yr) | | | Flow | | | Flow (5-yr) | | | Zn-Hyb | | | Zn-Hyb (5-yr) | | |
| Power Rating | MW | 2 | - | 2 | 2 | - | 2 | 2 | - | 2 | 2 | - | 2 | 2 | - | 2 | 2 | - | 2 |
| Duration | Hours | 2 | - | 2 | 2 | - | 2 | 2 | - | 2 | 2 | - | 2 | 2 | - | 2 | 2 | - | 2 |
| Cycle Life | Cycles | 5000 | - | 4000 | 5000 | - | 4000 | 10000 | - | 5000 | 10000 | - | 5000 | 2500 | - | 2000 | 2500 | - | 2000 |
| Usable Energy | MWh | 4 | - | 4 | 4 | - | 4 | 4 | - | 4 | 4 | - | 4 | 4 | - | 4 | 4 | - | 4 |
| 100% Depth of Discharge Cycles/Day | | 1.25 | - | 1.25 | 1.25 | - | 1.25 | 1.25 | - | 1.25 | 1.25 | - | 1.25 | 1.25 | - | 1.25 | 1.25 | - | 1.25 |
| fSoC | | 1 | - | 1 | 1 | - | 1 | 1 | - | 1 | 1 | - | 1 | 1 | - | 1 | 1 | - | 1 |
| Operating Days/Year | | 350 | - | 350 | 350 | - | 350 | 350 | - | 350 | 350 | - | 350 | 350 | - | 350 | 350 | - | 350 |
| Operating Hours/Year | | 875 | - | 875 | 875 | - | 875 | 875 | - | 875 | 875 | - | 875 | 875 | - | 875 | 875 | - | 875 |
| Project Life | Years | 20 | - | 20 | 20 | - | 20 | 20 | - | 20 | 20 | - | 20 | 20 | - | 20 | 20 | - | 20 |
| Annual Used Energy | MWh | 1750 | - | 1750 | 1750 | - | 1750 | 1750 | - | 1750 | 1750 | - | 1750 | 1750 | - | 1750 | 1750 | - | 1750 |
| Project Used Energy | MWh | 35000 | - | 35000 | 35000 | - | 35000 | 35000 | - | 35000 | 35000 | - | 35000 | 35000 | - | 35000 | 35000 | - | 35000 |
| Initial Capital Cost - DC | $/kWh | 350 | - | 450 | 350 | - | 450 | 210 | - | 367 | 130.2 | - | 227.54 | 160 | - | 300 | 152 | - | 285 |
| Initial Capital Cost - AC | $/kW | 450 | - | 650 | 265.5 | - | 383.5 | 1100 | - | 1181 | 649 | - | 696.79 | 450 | - | 650 | 265.5 | - | 383.5 |
| Total Initial Installed Cost | $/kW | 1150 | - | 1550 | 965.5 | - | 1283.5 | 1520 | - | 1915 | 909.4 | - | 1151.87 | 770 | - | 1250 | 569.5 | - | 953.5 |
| Replacement Cost - DC | $/kWh | 350 | - | 450 | 350 | - | 450 | 210 | - | 367 | 130.2 | - | 227.54 | 160 | - | 300 | 152 | - | 285 |
| Replacement Period | Years | 14.29 | | 11.43 | 14.29 | - | 11.43 | - | | 14.29 | - | - | 14.29 | 7.14 | | 5.71 | 7.14 | - | 5.71 |
| O&M % of CAPEX | % | 2.0% | - | 2.0% | 2.0% | - | 2.0% | 2.0% | - | 3.0% | 2.0% | - | 3.0% | 1.0% | - | 2.0% | 1.0% | - | 2.0% |
| O&M Cost | $/kW-year | 23 | - | 31 | 19.31 | - | 25.67 | 30.4 | - | 57.45 | 18.188 | - | 34.5561 | 7.7 | - | 25 | 5.695 | - | 19.07 |
| Charging Cost | $/MWh | 58 | - | 58 | 58 | - | 58 | 58 | - | 58 | 58 | - | 58 | 58 | - | 58 | 58 | - | 58 |
| Annual Cost Escalator | % | 0.0% | - | 0.0% | 0.0% | - | 0.0% | 0.0% | - | 0.0% | 0.0% | - | 0.0% | 0.0% | - | 0.0% | 0.0% | - | 0.0% |
| Efficiency | | 85% | - | 75% | 85% | - | 75% | 75% | - | 65% | 75% | - | 65% | 75% | - | 60% | 75% | - | 60% |
| Levelized Cost of Storage | $/kW-year | 252 | - | 334 | 225 | - | 296 | 286 | - | 401 | 198 | - | 272 | 205 | - | 359 | 176 | - | 311 |
| Levelized Cost of Storage D | $/MWh | 288 | - | 382 | 258 | - | 338 | 326 | - | 458 | 226 | - | 311 | 234 | - | 410 | 201 | - | 356 |

**Table A-6:** LCOE results for PV integration, 20 yr life, 2 h discharge, 1.25 cycles/day, 350 days/year.

| | | PV Integration LCOE Data ($/MWh) | | | | | | | | | | | |
|---|---|---|---|---|---|---|---|---|---|---|---|---|---|
| | Units | PbA | | PbA (5-yr) | | ALAB | | ALAB (5-yr) | | Li-Ion | | Li-Ion (5-yr) | |
| **Capital Cost** | $/MWh | 100 | 139 | 67 | 93 | 115 | 179 | 79 | 123 | 130 | 204 | 72 | 113 |
| **Charging** | $/MWh | 71 | 76 | 71 | 76 | 71 | 76 | 71 | 76 | 63 | 67 | 63 | 67 |
| **O&M** | $/MWh | 19 | 33 | 13 | 22 | 22 | 43 | 15 | 29 | 19 | 39 | 10 | 22 |
| **Replacement** | $/MWh | 61 | 632 | 46 | 480 | 16 | 87 | 12 | 66 | 23 | 352 | 12 | 187 |
| **Taxes** | $/MWh | 30 | 142 | 21 | 106 | 24 | 49 | 17 | 35 | 28 | 103 | 15 | 55 |
| **Total** | $/MWh | 281 | 1023 | 218 | 777 | 249 | 435 | 194 | 330 | 262 | 765 | 173 | 443 |

| | | NaS | | NaS (5-yr) | | Flow | | Flow (5-yr) | | Zn-Hyb | | Zn-Hyb (5-yr) | |
|---|---|---|---|---|---|---|---|---|---|---|---|---|---|
| **Capital Cost** | $/MWh | 138 | 186 | 116 | 154 | 182 | 229 | 109 | 138 | 92 | 150 | 68 | 114 |
| **Charging** | $/MWh | 67 | 76 | 67 | 76 | 76 | 88 | 76 | 88 | 76 | 95 | 76 | 95 |
| **O&M** | $/MWh | 26 | 35 | 22 | 29 | 35 | 66 | 21 | 39 | 9 | 29 | 7 | 22 |
| **Replacement** | $/MWh | 27 | 43 | 27 | 43 | 0 | 28 | 0 | 17 | 34 | 92 | 32 | 87 |
| **Taxes** | $/MWh | 30 | 42 | 26 | 36 | 34 | 48 | 20 | 29 | 23 | 45 | 19 | 37 |
| **Total** | $/MWh | 288 | 382 | 258 | 338 | 326 | 458 | 226 | 311 | 234 | 410 | 201 | 356 |

**Table A-7:** LCOE model and data for C&I, 10 yr life, 4 h discharge, 1 cycle/day, 350 days/year.

| | | Commercial & Industrial | | | | | | | | | | | | | | | | | | | | | |
|---|---|---|---|---|---|---|---|---|---|---|---|---|---|---|---|---|---|---|---|---|---|---|---|
| | **Units** | **PbA** | | | **PbA (5-yr)** | | | **ALAB** | | | **ALAB (5-yr)** | | | **Li-Ion** | | | **Li-Ion (5-yr)** | | |
| Power Rating | MW | 1 | - | 1 | 1 | - | 1 | 1 | - | 1 | 1 | - | 1 | 1 | - | 1 | 1 | - | 1 |
| Duration | Hours | 4 | - | 4 | 4 | - | 4 | 4 | - | 4 | 4 | - | 4 | 4 | - | 4 | 4 | - | 4 |
| Cycle Life | Cycles | 1765 | - | 294 | 1765 | - | 294 | 5000 | - | 2222 | 5000 | - | 2222 | 5000 | - | 1000 | 5000 | - | 1000 |
| Usable Energy | MWh | 4 | - | 4 | 4 | - | 4 | 4 | - | 4 | 4 | - | 4 | 4 | - | 4 | 4 | - | 4 |
| 100% Depth of Discharge Cycles/Day | | 0.85 | - | 0.85 | 0.85 | - | 0.85 | 0.9 | - | 0.9 | 0.9 | - | 0.9 | 1 | - | 1 | 1 | - | 1 |
| fSoC | | 0.85 | - | 0.85 | 0.85 | - | 0.85 | 0.9 | - | 0.9 | 0.9 | - | 0.9 | 1 | - | 1 | 1 | - | 1 |
| Operating Days/Year | | 350 | - | 350 | 350 | - | 350 | 350 | - | 350 | 350 | - | 350 | 350 | - | 350 | 350 | - | 350 |
| Operating Hours/Year | | 1400 | - | 1400 | 1400 | - | 1400 | 1400 | - | 1400 | 1400 | - | 1400 | 1400 | - | 1400 | 1400 | - | 1400 |
| Project Life | Years | 10 | - | 10 | 10 | - | 10 | 10 | - | 10 | 10 | - | 10 | 10 | - | 10 | 10 | - | 10 |
| Annual Used Energy | MWh | 1400 | - | 1400 | 1400 | - | 1400 | 1400 | - | 1400 | 1400 | - | 1400 | 1400 | - | 1400 | 1400 | - | 1400 |
| Project Used Energy | MWh | 14000 | - | 14000 | 14000 | - | 14000 | 14000 | - | 14000 | 14000 | - | 14000 | 14000 | - | 14000 | 14000 | - | 14000 |
| Initial Capital Cost - DC | $/kWh | 150 | - | 200 | 114 | - | 152 | 200 | - | 330 | 152 | - | 251 | 300 | - | 500 | 159 | - | 265 |
| Initial Capital Cost - AC | $/kW | 765 | - | 1105 | 451 | - | 652 | 765 | - | 1105 | 451 | - | 652 | 765 | - | 1105 | 451 | - | 652 |
| Total Initial Installed Cost | $/kW | 1471 | - | 2046 | 988 | - | 1367 | 1654 | - | 2572 | 1127 | - | 1767 | 1965 | - | 3105 | 1087 | - | 1712 |
| Replacement Cost - DC | $/kWh | 150 | - | 200 | 114 | - | 152 | 200 | - | 330 | 152 | - | 250.8 | 300 | - | 500 | 159 | - | 265 |
| Replacement Period | Years | 5.04 | - | 0.84 | 5.04 | - | 0.84 | - | - | 6.35 | - | - | 6.35 | - | - | 2.86 | - | - | 2.86 |
| O&M % of CAPEX | % | 2.0% | - | 2.5% | 2.0% | - | 2.5% | 2.0% | - | 2.5% | 2.0% | - | 2.5% | 1.5% | - | 2.0% | 1.5% | - | 2.0% |
| O&M Cost | $/kW-year | 29 | | 51 | 20 | | 34 | 33 | | 64 | 23 | | 44 | 29 | - | 62 | 16 | | 34 |
| Charging Cost | $/MWh | 70 | - | 70 | 70 | - | 70 | 70 | - | 70 | 70 | - | 70 | 70 | - | 70 | 70 | - | 70 |
| Annual Cost Escalator | % | 2.6% | - | 2.6% | 2.6% | - | 2.6% | 2.6% | - | 2.6% | 2.6% | - | 2.6% | 2.6% | - | 2.6% | 2.6% | - | 2.6% |
| Efficiency | | 80% | - | 75% | 80% | - | 75% | 80% | - | 75% | 80% | - | 75% | 90% | - | 85% | 90% | - | 85% |
| Levelized Cost of Storage | $/kW-year | 467 | | 1778 | 351 | | 1336 | 420 | | 779 | 315 | | 577 | 462 | | 1394 | 291 | | 792 |
| Levelized Cost of Storage D | $/MWh | 334 | | 1270 | 251 | | 954 | 300 | | 556 | 225 | | 412 | 330 | | 996 | 208 | | 566 |

| | | Commercial & Industrial (Continued) | | | | | | | | | | | | | | | | | | | | | |
|---|---|---|---|---|---|---|---|---|---|---|---|---|---|---|---|---|---|---|---|---|---|---|---|
| | **Units** | **NaS** | | | **NaS (5-yr)** | | | **Flow** | | | **Flow (5-yr)** | | | **Zn-Hyb** | | | **Zn-Hyb (5-yr)** | | |
| Power Rating | MW | 1 | - | 1 | 1 | - | 1 | 1 | - | 1 | 1 | - | 1 | 1 | - | 1 | 1 | - | 1 |
| Duration | Hours | 4 | - | 4 | 4 | - | 4 | 4 | - | 4 | 4 | - | 4 | 4 | - | 4 | 4 | - | 4 |
| Cycle Life | Cycles | 5000 | - | 4000 | 5000 | - | 4000 | 10000 | - | 5000 | 10000 | - | 5000 | 2500 | - | 2000 | 2500 | - | 2000 |
| Usable Energy | MWh | 4 | - | 4 | 4 | - | 4 | 4 | - | 4 | 4 | - | 4 | 4 | - | 4 | 4 | - | 4 |
| 100% Depth of Discharge Cycles/Day | | 1 | - | 1 | 1 | - | 1 | 1 | - | 1 | 1 | - | 1 | 1 | - | 1 | 1 | - | 1 |
| fSoC | | 1 | - | 1 | 1 | - | 1 | 1 | - | 1 | 1 | - | 1 | 1 | - | 1 | 1 | - | 1 |
| Operating Days/Year | | 350 | - | 350 | 350 | - | 350 | 350 | - | 350 | 350 | - | 350 | 350 | - | 350 | 350 | - | 350 |
| Operating Hours/Year | | 1400 | - | 1400 | 1400 | - | 1400 | 1400 | - | 1400 | 1400 | - | 1400 | 1400 | - | 1400 | 1400 | - | 1400 |
| Project Life | Years | 10 | - | 10 | 10 | - | 10 | 10 | - | 10 | 10 | - | 10 | 10 | - | 10 | 10 | - | 10 |
| Annual Used Energy | MWh | 1400 | - | 1400 | 1400 | - | 1400 | 1400 | - | 1400 | 1400 | - | 1400 | 1400 | - | 1400 | 1400 | - | 1400 |
| Project Used Energy | MWh | 14000 | - | 14000 | 14000 | - | 14000 | 14000 | - | 14000 | 14000 | - | 14000 | 14000 | - | 14000 | 14000 | - | 14000 |
| Initial Capital Cost - DC | $/kWh | 350 | - | 450 | 350 | - | 450 | 210 | - | 367 | 130.2 | - | 227.54 | 160 | - | 300 | 152 | - | 285 |
| Initial Capital Cost - AC | $/kW | 765 | - | 1105 | 451 | - | 652 | 1870 | - | 2008 | 1103 | - | 1185 | 765 | - | 1105 | 451 | - | 652 |
| Total Initial Installed Cost | $/kW | 2165 | - | 2905 | 1851 | - | 2452 | 2710 | - | 3476 | 1624 | - | 2095 | 1405 | - | 2305 | 1059 | - | 1792 |
| Replacement Cost - DC | $/kWh | 350 | - | 450 | 350 | - | 450 | 210 | - | 367 | 130.2 | - | 227.54 | 160 | - | 300 | 152 | - | 285 |
| Replacement Period | Years | - | - | - | - | - | - | - | - | - | - | - | - | 7.14 | - | 5.71 | 7.14 | - | 5.71 |
| O&M % of CAPEX | % | 2.0% | - | 2.0% | 2.0% | - | 2.0% | 2.0% | - | 3.0% | 2.0% | - | 3.0% | 1.0% | - | 2.0% | 1.0% | - | 2.0% |
| O&M Cost | $/kW-year | 43 | | 58 | 37 | | 49 | 54 | | 104 | 32 | | 63 | 14 | | 46 | 11 | | 36 |
| Charging Cost | $/MWh | 70 | - | 70 | 70 | - | 70 | 70 | - | 70 | 70 | - | 70 | 70 | - | 70 | 70 | - | 70 |
| Annual Cost Escalator | % | 2.6% | - | 2.6% | 2.6% | - | 2.6% | 2.6% | - | 2.6% | 2.6% | - | 2.6% | 2.6% | - | 2.6% | 2.6% | - | 2.6% |
| Efficiency | | 85% | - | 75% | 85% | - | 75% | 75% | - | 65% | 75% | - | 65% | 75% | - | 60% | 75% | - | 60% |
| Levelized Cost of Storage | $/kW-year | 516 | | 675 | 454 | | 585 | 636 | | 838 | 420 | | 549 | 426 | | 715 | 358 | | 606 |
| Levelized Cost of Storage D | $/MWh | 369 | | 482 | 324 | | 418 | 454 | | 599 | 300 | | 392 | 305 | | 511 | 256 | | 433 |

**Table A-8:** LCOE results for C&I, 10 yr life, 4 h discharge, 1 cycle/day, 350 days/year.

| | | Commercial & Industrial LCOE Data ($/MWh) | | | | | | | | | | | | | | | | | | | | | |
|---|---|---|---|---|---|---|---|---|---|---|---|---|---|---|---|---|---|---|---|---|---|---|---|
| | Units | PbA | | | PbA (5-yr) | | | ALAB | | | ALAB (5-yr) | | | Li-Ion | | | Li-Ion (5-yr) | | | | | | |
| **Capital Cost** | $/MWh | 159 | - | 222 | 107 | - | 148 | 179 | - | 279 | 122 | - | 191 | 213 | - | 336 | 118 | - | 185 | | | | |
| **Charging** | $/MWh | 64 | - | 69 | 64 | - | 69 | 64 | - | 69 | 64 | - | 69 | 57 | - | 61 | 57 | - | 61 | | | | |
| **O&M** | $/MWh | 21 | - | 37 | 14 | - | 24 | 24 | - | 46 | 16 | - | 32 | 21 | - | 44 | 12 | - | 24 | | | | |
| **Replacement** | $/MWh | 51 | - | 764 | 39 | - | 581 | 0 | - | 95 | 0 | - | 72 | 0 | - | 417 | 0 | - | 221 | | | | |
| **Taxes** | $/MWh | 38 | - | 179 | 26 | - | 132 | 33 | - | 68 | 22 | - | 48 | 39 | - | 137 | 21 | - | 74 | | | | |
| **Total** | $/MWh | 334 | - | 1270 | 251 | - | 954 | 300 | - | 556 | 225 | - | 412 | 330 | - | 996 | 208 | - | 566 | | | | |

| | | NaS | | | NaS (5-yr) | | | Flow | | | Flow (5-yr) | | | Zn-Hyb | | | Zn-Hyb (5-yr) | | | | | | |
|---|---|---|---|---|---|---|---|---|---|---|---|---|---|---|---|---|---|---|---|---|---|---|---|
| **Capital Cost** | $/MWh | 235 | - | 315 | 201 | - | 266 | 294 | - | 377 | 176 | - | 227 | 152 | - | 250 | 115 | - | 194 | | | | |
| **Charging** | $/MWh | 61 | - | 69 | 61 | - | 69 | 69 | - | 79 | 69 | - | 79 | 69 | - | 86 | 69 | - | 86 | | | | |
| **O&M** | $/MWh | 31 | - | 42 | 26 | - | 35 | 39 | - | 74 | 23 | - | 45 | 10 | - | 33 | 8 | - | 26 | | | | |
| **Replacement** | $/MWh | 0 | - | 0 | 0 | - | 0 | 0 | - | 0 | 0 | - | 0 | 39 | - | 82 | 37 | - | 78 | | | | |
| **Taxes** | $/MWh | 43 | - | 57 | 36 | - | 48 | 53 | - | 68 | 32 | - | 41 | 35 | - | 60 | 28 | - | 49 | | | | |
| **Total** | $/MWh | 369 | - | 482 | 324 | - | 418 | 454 | - | 599 | 300 | - | 392 | 305 | - | 511 | 256 | - | 433 | | | | |

**Table A-9:** LCOE model and data for residential systems, 10 yr life, 2 h discharge, 1 cycle/day, 300 days/year.

| | | Residential | | | | | | | | | | | | | | | | | | | | | |
|---|---|---|---|---|---|---|---|---|---|---|---|---|---|---|---|---|---|---|---|---|---|---|---|
| | Units | PbA | | | PbA (5-yr) | | | ALAB | | | ALAB (5-yr) | | | Li-Ion | | | Li-Ion (5-yr) | | | | | |
| Power Rating | MW | 0.005 | - | 0.005 | 0.005 | - | 0.005 | 0.005 | - | 0.005 | 0.005 | - | 0.005 | 0.005 | - | 0.005 | 0.005 | - | 0.005 | | | |
| Duration | Hours | 2 | - | 2 | 2 | - | 2 | 2 | - | 2 | 2 | - | 2 | 2 | - | 2 | 2 | - | 2 | | | |
| Cycle Life | Cycles | 1923 | - | 321 | 1923 | - | 321 | 5769 | - | 2564 | 5769 | - | 2564 | 5263 | - | 1053 | 5263 | - | 1053 | | | |
| Usable Energy | MWh | 0.01 | - | 0.01 | 0.01 | - | 0.01 | 0.01 | - | 0.01 | 0.01 | - | 0.01 | 0.01 | - | 0.01 | 0.01 | - | 0.01 | | | |
| 100% Depth of Discharge Cycles/Day | | 0.78 | - | 0.78 | 0.78 | - | 0.78 | 0.78 | - | 0.78 | 0.78 | - | 0.78 | 0.95 | - | 0.95 | 0.95 | - | 0.95 | | | |
| fSoC | | 0.78 | - | 0.78 | 0.78 | - | 0.78 | 0.78 | - | 0.78 | 0.78 | - | 0.78 | 0.95 | - | 0.95 | 0.95 | - | 0.95 | | | |
| Operating Days/Year | | 300 | - | 300 | 300 | - | 300 | 300 | - | 300 | 300 | - | 300 | 300 | - | 300 | 300 | - | 300 | | | |
| Operating Hours/Year | | 600 | - | 600 | 600 | - | 600 | 600 | - | 600 | 600 | - | 600 | 600 | - | 600 | 600 | - | 600 | | | |
| Project Life | Years | 10 | - | 10 | 10 | - | 10 | 10 | - | 10 | 10 | - | 10 | 10 | - | 10 | 10 | - | 10 | | | |
| Annual Used Energy | MWh | 3 | - | 3 | 3 | - | 3 | 3 | - | 3 | 3 | - | 3 | 3 | - | 3 | 3 | - | 3 | | | |
| Project Used Energy | MWh | 30 | - | 30 | 30 | - | 30 | 30 | - | 30 | 30 | - | 30 | 30 | - | 30 | 30 | - | 30 | | | |
| Initial Capital Cost - DC | $/kWh | 150 | - | 200 | 114 | - | 152 | 200 | - | 330 | 152 | - | 250.8 | 300 | - | 500 | 159 | - | 265 | | | |
| Initial Capital Cost - AC | $/kW | 1013 | - | 1463 | 597 | - | 863 | 1013 | - | 1463 | 597 | - | 863 | 1013 | - | 1463 | 597 | - | 863 | | | |
| Total Initial Installed Cost | $/kW | 1397 | - | 1975 | 890 | - | 1253 | 1525 | - | 2309 | 987 | - | 1506 | 1644 | - | 2515 | 932 | - | 1421 | | | |
| Replacement Cost - DC | $/kWh | 150 | - | 200 | 114 | - | 152 | 200 | - | 330 | 152 | - | 250.8 | 300 | - | 500 | 159 | - | 265 | | | |
| Replacement Period | Years | 6.41 | - | 1.07 | 6.41 | - | 1.07 | - | - | 8.55 | - | - | 8.55 | - | - | 3.51 | - | - | 3.51 | | | |
| O&M % of CAPEX | % | 2.0% | - | 2.5% | 2.0% | - | 2.5% | 2.0% | - | 2.5% | 2.0% | - | 2.5% | 1.5% | - | 2.0% | 1.5% | - | 2.0% | | | |
| O&M Cost | $/kW-year | 28 | - | 49 | 18 | - | 31 | 31 | - | 58 | 20 | - | 38 | 25 | - | 50 | 14 | - | 28 | | | |
| Charging Cost | $/MWh | 125 | - | 125 | 125 | - | 125 | 125 | - | 125 | 125 | - | 125 | 125 | - | 125 | 125 | - | 125 | | | |
| Annual Cost Escalator | % | 2.5% | - | 2.5% | 2.5% | - | 2.5% | 2.5% | - | 2.5% | 2.5% | - | 2.5% | 2.5% | - | 2.5% | 2.5% | - | 2.5% | | | |
| Efficiency | | 80% | - | 75% | 80% | - | 75% | 80% | - | 75% | 80% | - | 75% | 90% | - | 85% | 90% | - | 85% | | | |
| Levelized Cost of Storage | $/kW-year | 479 | | 1125 | 369 | | 845 | 464 | | 718 | 357 | | 536 | 462 | | 901 | 323 | | 566 | | | |
| Levelized Cost of Storage D | $/MWh | 799 | | 1875 | 614 | | 1409 | 773 | | 1197 | 594 | | 894 | 769 | | 1502 | 539 | | 943 | | | |

| | | Residential (Continued) | | | | | | | | | | | |
|---|---|---|---|---|---|---|---|---|---|---|---|---|---|
| | Units | Flow | | | Flow (5-yr) | | | Zn-Hyb | | | Zn-Hyb (5-yr) | | |
| Power Rating | MW | 0.005 | - | 0.005 | 0.005 | - | 0.005 | 0.005 | - | 0.005 | 0.005 | - | 0.005 |
| Duration | Hours | 2 | - | 2 | 2 | - | 2 | 2 | - | 2 | 2 | - | 2 |
| Cycle Life | Cycles | 10000 | - | 5000 | 10000 | - | 5000 | 2500 | - | 2000 | 2500 | - | 2000 |
| Usable Energy | MWh | 0.01 | - | 0.01 | 0.01 | - | 0.01 | 0.01 | - | 0.01 | 0.01 | - | 0.01 |
| 100% Depth of Discharge Cycles/Day | | 1 | - | 1 | 1 | - | 1 | 1 | - | 1 | 1 | - | 1 |
| fSoC | | 1 | - | 1 | 1 | - | 1 | 1 | - | 1 | 1 | - | 1 |
| Operating Days/Year | | 300 | - | 300 | 300 | - | 300 | 300 | - | 300 | 300 | - | 300 |
| Operating Hours/Year | | 600 | - | 600 | 600 | - | 600 | 600 | - | 600 | 600 | - | 600 |
| Project Life | Years | 10 | - | 10 | 10 | - | 10 | 10 | - | 10 | 10 | - | 10 |
| Annual Used Energy | MWh | 3 | - | 3 | 3 | - | 3 | 3 | - | 3 | 3 | - | 3 |
| Project Used Energy | MWh | 30 | - | 30 | 30 | - | 30 | 30 | - | 30 | 30 | - | 30 |
| Initial Capital Cost - DC | $/kWh | 210 | - | 367 | 130.2 | - | 227.54 | 160 | - | 300 | 152 | - | 285 |
| Initial Capital Cost - AC | $/kW | 2475 | - | 2657 | 1460 | - | 1568 | 1013 | - | 1463 | 597 | - | 863 |
| Total Initial Installed Cost | $/kW | 2895 | - | 3391 | 1721 | - | 2023 | 1333 | - | 2063 | 901 | - | 1433 |
| Replacement Cost - DC | $/kWh | 210 | - | 367 | 130.2 | - | 227.54 | 160 | - | 300 | 152 | - | 285 |
| Replacement Period | Years | - | - | - | - | - | - | 8.33 | - | 6.67 | 8.33 | - | 6.67 |
| O&M % of CAPEX | % | 2.0% | - | 3.0% | 2.0% | - | 3.0% | 1.0% | - | 2.0% | 1.0% | - | 2.0% |
| O&M Cost | $/kW-year | 57.9 | - | 101.7 | 34.4 | - | 60.7 | 13.3 | - | 41.3 | 9.0 | - | 28.7 |
| Charging Cost | $/MWh | 125 | - | 125 | 125 | - | 125 | 125 | - | 125 | 125 | - | 125 |
| Annual Cost Escalator | % | 2.5% | - | 2.5% | 2.5% | - | 2.5% | 2.5% | - | 2.5% | 2.5% | - | 2.5% |
| Efficiency | | 75% | - | 65% | 75% | - | 65% | 75% | - | 60% | 75% | - | 60% |
| Levelized Cost of Storage | $/kW-year | 747 | | 906 | 513 | | 620 | 452 | | 687 | 369 | | 558 |
| Levelized Cost of Storage D | $/MWh | 1246 | | 1511 | 856 | | 1034 | 754 | | 1145 | 615 | | 931 |

**Table A-10:** LCOE results for residential systems, 10 yr life, 2 h discharge, 1 cycle/day, 300 days/year.

| | | Residential LCOE Data ($/MWh) | | | | | | | | | | | |
|---|---|---|---|---|---|---|---|---|---|---|---|---|---|
| | Units | PbA | | PbA (5-yr) | | ALAB | | ALAB (5-yr) | | Li-Ion | | Li-Ion (5-yr) | |
| **Capital Cost** | $/MWh | 353 | 499 | 225 | 317 | 386 | 584 | 250 | 381 | 416 | 636 | 236 | 359 |
| **Charging** | $/MWh | 267 | 284 | 267 | 284 | 267 | 284 | 267 | 284 | 237 | 251 | 237 | 251 |
| **O&M** | $/MWh | 47 | 82 | 30 | 52 | 51 | 96 | 33 | 63 | 41 | 84 | 23 | 47 |
| **Replacement** | $/MWh | 58 | 777 | 44 | 591 | 0 | 107 | 0 | 82 | 0 | 352 | 0 | 186 |
| **Taxes** | $/MWh | 75 | 232 | 49 | 165 | 70 | 125 | 45 | 84 | 75 | 179 | 43 | 99 |
| **Total** | $/MWh | 799 | 1875 | 614 | 1409 | 773 | 1197 | 594 | 894 | 769 | 1502 | 539 | 943 |

| | | Flow | | Flow (5-yr) | | Zn-Hyb | | Zn-Hyb (5-yr) | |
|---|---|---|---|---|---|---|---|---|---|
| **Capital Cost** | $/MWh | 732 | 857 | 435 | 511 | 337 | 521 | 228 | 362 |
| **Charging** | $/MWh | 284 | 328 | 284 | 328 | 284 | 356 | 284 | 356 |
| **O&M** | $/MWh | 97 | 170 | 57 | 101 | 22 | 69 | 15 | 48 |
| **Replacement** | $/MWh | 0 | 0 | 0 | 0 | 41 | 89 | 39 | 84 |
| **Taxes** | $/MWh | 133 | 156 | 79 | 93 | 69 | 111 | 49 | 81 |
| **Total** | $/MWh | 1246 | 1511 | 856 | 1034 | 754 | 1145 | 615 | 931 |

# Appendix B – Rietveld refinement data for chapter 3

**Table B-1:** Phase analysis results for 24 h curing of PowerSonic Pb-Ca electrode during curing at 80 °C.

| Electrode curing x-ray data | | | | | | | | | | | | | | |
|---|---|---|---|---|---|---|---|---|---|---|---|---|---|---|
| | Pb | αPbO | β-PbO | $Pb_3(CO_3)_2(OH)_2$ | $PbSO_4$ | 1BS | 3BS | 4BS | $Pb_3O_4$ | $\alpha PbO_2$ | $\beta-PbO_2$ | Total | Rwp | GOF |
| New Negative - Curing 0h | 35.2 | 1.5 | 0.3 | 0.0 | 45.5 | 0.2 | 17.2 | 0.0 | 0.0 | 0.0 | 0.0 | 99.9 | 7.37 | 1.71 |
| New Negative - Curing 6h | 37.4 | 0.7 | 0.8 | 1.0 | 40.0 | 0.0 | 19.9 | 0.0 | 0.2 | 0.0 | 0.0 | 100.0 | 6.52 | 1.38 |
| New Negative - Curing 12h | 27.7 | 0.8 | 0.6 | 0.0 | 64.5 | 0.1 | 6.3 | 0.0 | 0.0 | 0.0 | 0.0 | 100.0 | 7.70 | 1.84 |
| New Negative - Curing 18h | 28.4 | 0.4 | 0.0 | 0.0 | 62.7 | 0.0 | 8.5 | 0.0 | 0.0 | 0.0 | 0.0 | 100.0 | 7.47 | 1.57 |
| New Negative - Curing 24h | 35.5 | 0.6 | 0.0 | 0.2 | 50.8 | 0.0 | 12.7 | 0.0 | 0.0 | 0.0 | 0.0 | 99.8 | 8.31 | 1.73 |

**Table B-2:** X-ray phase analysis results for Yuasa and PowerSonic Pb-Ca electrodes pre- and post-inverse charging

| Electrode curing and $SnSO_4$ x-ray data | | | | | | | | | | | | | | |
|---|---|---|---|---|---|---|---|---|---|---|---|---|---|---|
| **YUASA** | **Pb** | **α-PbO** | **β-PbO** | $Pb_3(CO_3)_2(OH)_2$ | $PbSO_4$ | **1BS** | **3BS** | **4BS** | $Pb_3O_4$ | $\alpha-PbO_2$ | $\beta-PbO_2$ | **Total** | **Rwp** | **GOF** |
| New Negative 1 | 54.2 | 4.4 | 22.5 | 14.2 | 0.4 | 0.0 | 3.7 | 0.0 | 0.5 | 0.0 | 0.0 | 99.9 | 11.51 | 4.16 |
| New 1, post-inverse | 61.1 | 3.3 | 14.1 | 0.0 | 6.4 | 0.0 | 14.8 | 0.0 | 0.3 | 0.0 | 0.0 | 100.0 | 13.12 | 4.68 |
| New 2 + $SnSO_4$ (post-inv) | 48.5 | 0.0 | 0.0 | 2.1 | 46.7 | 0.0 | 2.5 | 0.0 | 0.1 | 0.0 | 0.0 | 99.9 | 9.04 | 3.39 |
| New 3 +$SnSO_4$ (post-inv) | 23.0 | 1.2 | 0.2 | 0.0 | 69.1 | 0.0 | 0.8 | 0.0 | 0.0 | 0.2 | 5.6 | 100.1 | 9.74 | 3.21 |
| **PowerSonic** | | | | | | | | | | | | | | |
| New Negative 1 | 35.2 | 1.5 | 0.3 | 0.0 | 45.5 | 0.2 | 17.2 | 0.0 | 0.0 | 0.0 | 0.0 | 99.9 | 7.37 | 1.71 |
| New 1, post-inverse | 85.6 | 0.3 | 4.5 | 5.4 | 3.4 | 0.1 | 0.2 | 0.0 | 0.1 | 0.4 | 0.0 | 100.0 | 8.88 | 2.68 |
| New 2, post-inverse | 38.1 | 0.2 | 4.9 | 0.5 | 54.3 | 0.2 | 1.8 | 0.0 | 0.1 | 0.0 | 0.0 | 100.1 | 8.61 | 2.42 |
| New 3 + $SnSO_4$ (post-inv) | 88.7 | 1.0 | 0.0 | 0.2 | 5.9 | 0.0 | 4.1 | 0.1 | 0.0 | 0.0 | 0.0 | 100.0 | 9.11 | 3.24 |
| 24h cure, post-inverse | 59.2 | 0.3 | 9.6 | 0.5 | 12.8 | 0.6 | 14.5 | 0.2 | 0.0 | 2.1 | 0.3 | 100.1 | 7.23 | 1.70 |

# Appendix C – Rietveld refinement data for chapter 4

**Table C-1:** X-ray diffraction Rietveld refinement phase composition of electrode samples during key points pre- and post-inverse charging for Battery 5. Samples for the second inverse charge were analyzed 5 cycles after inverse charging.

| Battery 5 XRD Rietveld refinement data: negative YUASA Pb-Ca electrodes | | | | | | | | | | | | | | |
|---|---|---|---|---|---|---|---|---|---|---|---|---|---|---|
| | **Pb** | **αPbO** | **β-PbO** | **$Pb_3(CO_3)_2(OH)_2$** | **$PbSO_4$** | **1BS** | **3BS** | **4BS** | **$Pb_3O_4$** | **α$PbO_2$** | **β-$PbO_2$** | **Total** | **Rwp** | **GOF** |
| New | 62.8 | 0.0 | 30.6 | 0.0 | 0.0 | 0.0 | 6.6 | 0.0 | 0.0 | 0.0 | 0.0 | 100.0 | 12.72 | 4.04 |
| 327 cycles (upper) | 36.5 | 0.4 | 10.5 | 0.0 | 10.8 | 0.0 | 40.8 | 1.0 | 0.0 | 0.0 | 0.0 | 100.0 | 9.39 | 3.99 |
| 327 cycles (lower) | 8.5 | 0.0 | 0.0 | 0.0 | 91.5 | 0.0 | 0.0 | 0.0 | 0.0 | 0.0 | 0.0 | 100.0 | 11.55 | 4.18 |
| Inverse 1 (upper) | 11.7 | 5.7 | 6.9 | 0.3 | 60.9 | 0.0 | 14.7 | 0.0 | 0.0 | 0.0 | 0.0 | 100.2 | 9.08 | 3.07 |
| Inverse 1 (lower) | 8.9 | 0.3 | 0.5 | 3.3 | 84.8 | 0.0 | 2.2 | 0.0 | 0.0 | 0.0 | 0.0 | 100.0 | 7.82 | 2.64 |
| Inverse 2 (upper) | 16.2 | 0.0 | 1.7 | 0.0 | 74.2 | 0.0 | 7.7 | 0.0 | 0.2 | 0.0 | 0.0 | 100.0 | 7.19 | 2.43 |
| Inverse 2 (lower) | 6.4 | 0.0 | 0.0 | 0.0 | 93.6 | 0.0 | 0.0 | 0.0 | 0.0 | 0.0 | 0.0 | 100.0 | 11.61 | 4.95 |

| Battery 5 XRD Rietveld refinement data: positive YUASA Pb-Sb electrodes | | | | | | | | | | | | | | |
|---|---|---|---|---|---|---|---|---|---|---|---|---|---|---|
| | **Pb** | **αPbO** | **β-PbO** | **$Pb_3(CO_3)_2(OH)_2$** | **$PbSO_4$** | **1BS** | **3BS** | **4BS** | **$Pb_3O_4$** | **α$PbO_2$** | **β-$PbO_2$** | **Total** | **Rwp** | **GOF** |
| New | 0.1 | 1.1 | 0.0 | 0.0 | 1.0 | 0.6 | 7.1 | 0.0 | 8.5 | 32.6 | 49.1 | 100.1 | 8.61 | 4.07 |
| 327 cycles | 0.0 | 0.0 | 0.0 | 0.0 | 0.0 | 0.0 | 0.0 | 0.0 | 0.0 | 90.5 | 9.5 | 100.0 | 17.85 | 11.33 |
| Inverse 1 | 0.0 | 0.1 | 8.5 | 0.0 | 0.0 | 0.0 | 34.6 | 0.0 | 0.2 | 33.7 | 22.9 | 100.0 | 8.87 | 2.42 |
| Inverse 2 | 0.0 | 0.0 | 0.0 | 0.0 | 0.0 | 0.0 | 0.0 | 0.0 | 0.0 | 4.5 | 95.5 | 100.0 | 15.19 | 7.13 |

**Table C-2:** XRD Rietveld refinement phase composition of failed PowerSonic Pb-Ca electrode samples during key points pre-and post-inverse charging.

| XRD Rietveld refinement data: failed PowerSonic VRLA | | | | | | | | | | | | | | |
|---|---|---|---|---|---|---|---|---|---|---|---|---|---|---|
| | **Pb** | **αPbO** | **β-PbO** | **$Pb_3(CO_3)_2(OH)_2$** | **$PbSO_4$** | **1BS** | **3BS** | **4BS** | **$Pb_3O_4$** | **α$PbO_2$** | **β-$PbO_2$** | **Total** | **Rwp** | **GOF** |
| Electrode 1: Failed | 23.6 | 1.3 | 10.8 | 0.0 | 50.7 | 0.0 | 13.1 | 0.1 | 0.4 | 0.0 | 0.0 | 100.0 | 7.65 | 2.18 |
| Electrode 1: post-Inverse | 4.5 | 0.0 | 1.1 | 0.0 | 83.6 | 0.2 | 4.5 | 0.0 | 6.1 | 0.0 | 0.0 | 100.0 | 9.34 | 2.39 |
| Electrode 2: Failed | 14.3 | 0.1 | 3.5 | 0.0 | 74.1 | 0.0 | 7.7 | 0.2 | 0.1 | 0.0 | 0.0 | 100.0 | 8.08 | 1.93 |
| Electrode 2: post-Inverse | 8.0 | 0.5 | 1.3 | 0.0 | 83.2 | 0.1 | 6.2 | 0.7 | 0.0 | 0.0 | 0.0 | 100.0 | 11.58 | 3.68 |